Directional Raman spectroscopy: A surface-sensitive tool for measuring the chemical, optical, and physical properties of adsorbates on metal surfaces

by

Charles Kofi Adarkwa Nyamekye

A dissertation submitted to the graduate faculty

in partial fulfillment of the requirements for the degree of

DOCTOR OF PHILOSOPHY

Major: Chemistry

Program of Study Committee:
Emily A. Smith, Major Professor
Joseph W. Burnett
Levi M. Stanley
Patricia A. Thiel
Javier Vela-Becerra

Iowa State University

Ames, Iowa

2020

DEDICATION

This dissertation is dedicated to my parents, Andrew O. and Emelia, and my siblings, Andrew M., Andrew K., and Andrea, who have been my source of inspiration, support and strength. To my extended Family, thank you for all your love.

TABLE OF CONTENTS

Page

NOMENCLATURE v

ACKNOWLEDGMENTS vi

ABSTRACT vii

CHAPTER 1. GENERAL INTRODUCTION 1
    Dissertation Overview 1
    Raman Spectroscopy 1
    Surface Plasmon Resonance 4
    References 6

CHAPTER 2. THE EVOLUTION OF TOTAL INTERNAL REFLECTION RAMAN SPECTROSCOPY FOR THE CHEMICAL CHARACTERIZATION OF THIN FILMS AND INTERFACES 9
    Abstract 9
    Introduction 10
    Modeling the TIR Raman Signal 13
    Experimental TIR Raman Spectroscopy 16
    Polymer and Waveguide Samples 19
    Surface-Plasmon-Polariton-Enhanced (SPP) Raman Spectroscopy 25
    Directional Raman Scattering 27
    Conclusions 33
    Acknowledgements 35
    References 35

CHAPTER 3. COMBINED MEASUREMENT OF DIRECTIONAL RAMAN SCATTERING AND SURFACE-PLASMON-POLARITON CONE FROM ADSORBATES ON SMOOTH PLANAR GOLD SURFACES 44
    Abstract 44
    Introduction 45
    Materials and Methods 49
        Materials 49
        Sample Fabrication 50
        Directional-surface-plasmon-coupled Raman Spectrometer 51
        Surface-plasmon-polariton Cone Measurements 52
        Directional-surface-plasmon-coupled Raman Measurements 53
        Data Analysis and Calculations 54
    Results and Discussion 55
        Directional RS Instrumentation with Self-assembled Monolayer Sensitivity 55
        Quantification and Modelling of the Cone Diameter, Cone Intensity, and Raman Scattering 59
    Conclusions 65

- Acknowledgements 65
- References 66
- Supporting Information 68

CHAPTER 4. EXPERIMENTAL ANALYSIS OF WAVEGUIDE-COUPLED SURFACE-PLASMON-POLARITON CONE PROPERTIES 72
- Abstract 72
- Introduction 73
- Materials and Methods 77
  - Sample Preparation 77
  - Ellipsometry Thickness Measurements 78
  - Waveguide-coupled SPP Cone Measurements 79
  - Waveguide-coupled Directional Raman Measurements 80
  - Simulation of the Electric Field Intensity Distribution Around the Waveguide-coupled Directional-surface-plasmon-polariton Cones 80
- Results and Discussion 82
  - Quantification and Modeling of the Waveguide-coupled SPP Cones with Reverse-Kretschmann Raman Illumination 82
  - Waveguide-coupled SPP Cone Angular Intensity Pattern and Directional Raman Scattering Measurements with Kretschmann Illumination 87
- Conclusions 91
- Acknowledgements 93
- References 93
- Supporting Information 96

CHAPTER 5. DIRECTIONAL RAMAN SCATTERING SPECTRA OF METAL-SULFUR BONDS AT SMOOTH GOLD AND SILVER SUBSTRATES 111
- Abstract 111
- Introduction 112
- Materials and Methods 115
  - Materials 115
  - Sample Fabrication 116
  - Directional Raman Spectrometer 117
  - SPP Cone Images 118
  - Data Analysis 119
- Results and Discussion 120
  - SPP Cone Images of Benzenethiol Monolayer Adsorbed on Metallic Films 120
  - Directional Raman Scattering of Benzenethiol Monolayer Adsorbed on Metallic Films 123
- Conclusions 128
- Acknowledgements 128
- References 129
- Supporting Information 132

CHAPTER 6. GENERAL CONCLUSION 137

NOMENCLATURE

ATR	Attenuated Total Reflectance
FDTD	Finite-difference Time-domain
IR	Infrared
NIR	Near-Infrared
PC	Poly(bisphenol A carbonate)
PS	Polystyrene
PVPh	Poly(4-vinylphenol)
PWR	Plasmon Waveguide Resonance
RMS	Root Mean Square of Surface Roughness
RS	Raman Spectroscopy
SA	Scanning Angle
SAM	Self-assembled Monolayer
SERS	Surface-enhanced Raman Spectroscopy
SiO_2	Silica
SPCE	Surface-plasmon-coupled-emission
SPP	Surface Plasmon Polariton
SPR	Surface Plasmon Resonance
TIR	Total Internal Reflection

ACKNOWLEDGMENTS

I would like to thank my committee chair, Dr. Emily A. Smith, and my committee members, Drs. Joseph W. Burnett, Levi M. Stanley, Patricia A. Thiel, Javier Vela-Becerra, and Robert S. Houk (RSH served on my committee from 2014 to 2018), for their guidance, patience, mentorship, and care throughout my graduate studies and research. I am very blessed for the opportunity to be a member of the Smith Group, and it has been an honor and privilege working with Aleem, Jon, Danny, Qiaochu, Deyny, Chamari, Brett, Sadie, Jingzhe, Nicole, Avinash, Craig, and Vy. I would like to thank the Smith Group for their kindness, laughter, and everlasting memories during this endeavor. I want to also offer my appreciation to Dr. Stephen C. Weibel for his ample contribution and fruitful discussions to work presented in this dissertation. I would like to show gratitude to the Iowa State University Chemistry Department, for making my experience very fulfilling and enjoyable. Also, I would like to recognize Thelma Harding of the Graduate College and the Graduate Minority Assistance Program, for their tremendous support. I would like to acknowledge my undergraduate advisor, Dr. Sarah Pilkenton, for her leadership. I would like to thank the Guerrero Family (Pat, Cindy, Nick, and Marc), for their love and support. I would also like to acknowledge my friends for their kindness, and may we live long and prosper. Lastly, I would like to thank the Ames Laboratory and the National Science Foundation (NSF grant number CHE-1709099), for supporting my research through funding. This research was supported by the U.S. Department of Energy (DOE), Office of Science, Basic Energy Sciences, Chemical Sciences, Geosciences, and Biosciences Division at the Ames Laboratory under contract number DE-AC02-07CH11358. Ames Laboratory is operated for the DOE by Iowa State University. The document number assigned to this dissertation is IS-T 3266.

ABSTRACT

There is a need for sensitive methods to analyze thin films of polymers, biological cells, dielectric waveguides, and self-assembled monolayers. In this dissertation, we discuss a newly-developed instrument with combined benefits of surface plasmon resonance, plasmon waveguide resonance, and Raman spectroscopy for collecting the chemical information of adsorbates with monolayer sensitivity. Additionally, the instrument is applicable for measuring angle-dependent molecular interactions. Directional-surface-plasmon-coupled Raman spectroscopy (i.e., directional Raman scattering) is a viable non-destructive method equivalent to total internal reflection Raman spectroscopy using a smooth metal film. The excitation of surface plasmons produces directional Raman scattering in the plane of the metal film (in-coupling) and the emission of the scattered light through a Weierstrass prism (out-coupling). A hollow cone of directional scattering at a sharply defined angle results in the surface-plasmon-polariton cone radiating from the Weierstrass prism. The directionality of the signal, as well as the enhanced electric field, produces relatively large Raman signals at a smooth metal interface, without the use of surface-enhanced Raman substrates. The electric field intensity is amplified by 20-fold due to the directional emission of the scattered light and the collection of the entire surface-plasmon-polariton cone.

The directional Raman spectrometer has the capability of measuring the full surface-plasmon-polariton cone image, cone intensity, and directional Raman scattering radiating from the cone as a function of the incident angle. On the same instrument, the Kretschmann and reverse-Kretschmann configurations can provide multimodal spectral data (e.g., thickness and refractive indices) collection. The directional Raman spectrometer utilizes translational stages (as opposed to rotational stages, commonly used in surface plasmon resonance sensing). The

instrument design provides faster acquisition times and precise control of the light incident on the prism interface with 0.06° angle resolution.

We can quantify the surface-plasmon-polariton cone properties and intensity from the digitized surface-plasmon-polariton cone image by extracting the cone diameters from the cone angles. The calculated cone parameters are obtained using three-dimensional finite-difference time-domain simulations of the far-field angular radiation pattern in combination with Fresnel reflectivity calculations. The approach has equivalent sensitivity to alternative methods used to collect surface plasmon resonance and plasmon waveguide resonance data. Further, we can simultaneously measure the adsorption and chemical identification of thin films, waveguides, and self-assembled monolayers. The sensitivity of all the waveguide-coupled surface-plasmon-polariton cone modes is between 0.009 and 0.02° nm^{-1}. The incident angles that produce the surface-plasmon-polariton cones and the surface-plasmon-polariton cone angles are linearly dependent; therefore, it is straightforward to determine the optimum incident angle for collecting directional Raman scattering. According, the acquisition time is reduced for collecting plasmon waveguide resonance data. The thickness and chemical composition for thin films, as well as the structure and orientation of guided modes in waveguides, can be obtained in our multi-detection directional Raman scattering instrument.

Directional Raman spectroscopy can be applied to study photovoltaic thin films, polymer brushes, energy harvesting devices, optoelectronics, and sensor readout devices where the chemical composition, orientation, and morphology are essential to their function. This spectroscopic technique will propel new and emerging technologies in which functionalization of a surface is required.

CHAPTER 1. GENERAL INTRODUCTION

Dissertation Overview

This dissertation is organized into six chapters. Discussed within Chapter 1 is a brief and general introduction to the fundamental theories of Raman spectroscopy and surface plasmon resonance. In the critical review presented in Chapter 2, we describe the total internal reflection Raman spectroscopies developed over the past five decades with an emphasis on the recent advancements in the field. In Chapter 3, we present directional Raman spectroscopy: a non-destructive method analogous to total internal reflection Raman spectroscopy. Directional Raman spectroscopy technique analyzes the chemical composition and adsorbate properties (e.g., refractive indices and thicknesses) of self-assembled monolayers and thin polymer films adsorbed on smooth planar metallic surfaces. Within Chapter 4, we demonstrate directional Raman scattering for collecting plasmon waveguide resonance data. We report images of the waveguide-coupled surface-plasmon-polariton cone properties from dielectric waveguide materials such as silica, poly(methyl methacrylate), polystyrene, and poly(4-vinylphenol) thick films. In Chapter 5, we focus on the experimental measurement of the metal-sulfur bonds chemisorbed onto smooth planar gold and silver surfaces, as well as roughen gold surfaces with directional Raman spectroscopy. Lastly, Chapter 6 is a summary of the general conclusions and potential future directions for the work presented in this dissertation.

Raman Spectroscopy

Raman spectroscopy is an analytical technique used to study the rotational and vibrational transitions in molecules such as solids, liquids, and gases.[1-6] It was discovered in 1928 by Krishnan and Raman, when they experimentally demonstrated the phenomenon of inelastic scattering of light by molecules.[7] In 1930, Raman won the Nobel prize in physics for the discovery of the *Raman effect*, a technique named after him.

When monochromatic light interacts with molecules, the absorption of a photon of energy ($h\nu_0$) can give rise to elastic (i.e., Rayleigh) and inelastic (i.e., anti-Stokes and Stokes Raman) scattering of photons (Figure 1). Rayleigh scattering ($Energy = h\nu_0$) has no change or shift in energy for the scattered photons. The molecules are excited to a virtual state from the ground state (ν_0) for Stokes Raman scattering ($Energy = h(\nu_0 - \nu_1)$) or the lowest excited vibrational level (ν_1) for anti-Stokes Raman scattering ($Energy = h(\nu_0 + \nu_1)$). The result of inelastically scattered light by the molecules at a higher energy transition is known as anti-Stokes, and the lower energy transition is Stokes Raman scattering (Figure 1). Stokes Raman scattering is more intense than anti-Stokes Raman scattering because the molecules must be in the first vibrational level (ν_1), which has a lower population of molecules than the ground state (ν_0).[2] In contrast, Rayleigh scattering appears much more intense compared to the relatively weak Raman scattered light, where only one in 10^6 to 10^8 photons undergo the Raman effect.[6] Within this dissertation, only the Stokes Raman scattering was collected and analyzed.

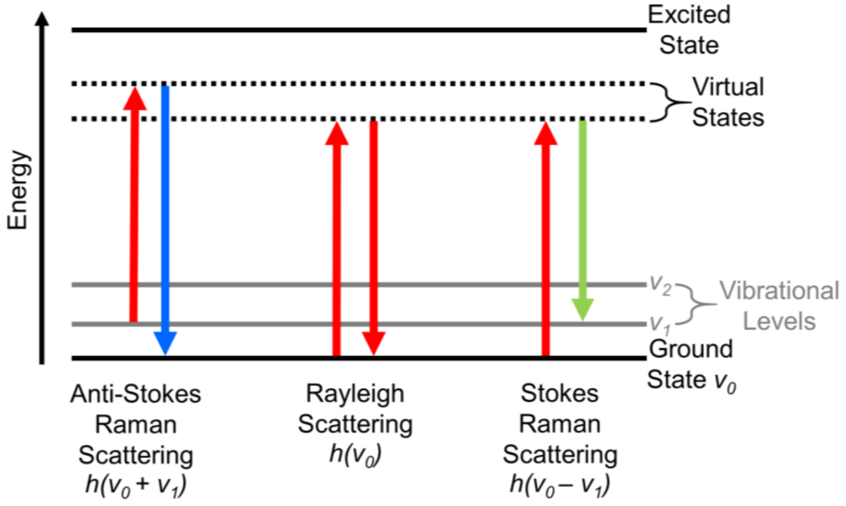

Figure 1. Jablonski energy-level diagram illustrating the Rayleigh scattering $h(\nu_0)$ and anti-Stokes $h(\nu_0 + \nu_1)$ and Stokes $h(\nu_0 - \nu_1)$ Raman scattering transitions, where h is Planck's

constant. The virtual state from a quantum mechanical viewpoint is an electron cloud distortion formed by the electric field of the monochromatic light.[3]

The excitation of vibrational modes in a molecule corresponds to the change in the frequency of the scattered light ($Energy = h(\nu_{ex} \pm \nu_1)$). For Raman scattering to occur, there must be a change in the polarizability (α) of the molecule during the vibration. In contrast, the polarizability remains constant for Rayleigh scattering. Equation 1 shows that the induced polarization (P) within the molecule produced by the polarizability (α) and the incident electric field (E) associated with the light beam is linearly proportional.

$$P = \alpha \times E \tag{1}$$

As indicated in this equation, a change in the polarizability of the molecule ($\alpha \neq 0$) can cause a small fraction of the scattered photons to give rise to a Raman shift. Also, a change in the distribution of the electron cloud around the vibrating atom will yield Raman bands. Ingle and Crouch presents the full mathematic and physical derivation of equation 1.[8]

Raman scattering can provide molecular vibrations and symmetry (i.e., asymmetric and symmetric stretches) from multiple bonds. For linear and non-linear molecules, there are $3N–5$ and $3N–6$ vibrational modes, respectively, where N is the number of atoms. A full description of the mechanism, selection rules, and details for Raman spectroscopy are eloquently presented by McCreery[3], Long[2], Smith and Dent,[4, 6, 9] and Lewis and Edwards.[1]

Raman spectroscopy alone is not a surface-sensitive technique even though the Rayleigh and Raman intensities are linearly proportional to the incident electric field given by equation 1. A more intense source such as a laser could enhance the Raman signals. But, the combination of Raman spectroscopy and surface plasmon resonance detects the chemical information of adsorbates on a surface. Additionally, the adsorption properties (e.g., the index of refraction, thickness, rate constants, and kinetics) of the molecular interactions on a surface can be measured. A discussion on the basic principles of surface plasmon resonance is in the next section.

Surface Plasmon Resonance

Surface plasmon resonance (SPR) is an optical absorption spectroscopic method for detecting and characterizing the chemical changes occurring at a thin noble metal surface.[10-20] The phenomenon is associated with total internal reflection (TIR) of light at a boundary between a TIR element or prism and a noble metal film, such as gold, silver, copper, or platinum. The dielectric permittivity of the prism (ε_P) must be greater than the dielectric function of the metal ($\varepsilon_M = \varepsilon_r + i\varepsilon_{im}$) and the adjacent layer (ε_L), where $i = \sqrt{-1}$, and the subscripts indicate the real (r) and imaginary (im) components.[21-23] The dielectric medium and constant are wavelength (frequency) dependent. In the Kretschmann configuration (Figure 1a), a p-polarized 785-nm laser passes through a sapphire prism and reflects off the backside of a thin gold film and into a detector. When the incident angle (θ_{INC}) is above the critical angle (θ_C), an evanescent wave is generated at the prism/air or sample interface and exponentially decays into the air or sample layer. The evanescent wave can extend ~200 nm into the air or sample interface and is dependent on the wavelength of light, the indices of reflection of the dielectric medium on either side of the metal film, and the properties of the metal film.[24]

At the SPR angle (θ_{SPR}), surface plasmon polaritons are generated at the metal surface due to the coupling of the excitation light (k_x) with collective oscillations of the electrons from the metal substrate (k_{SP}). When $\theta_{INC} > \theta_C$ the light travels through the prism and reflects off the metal film and the adjacent layer. The condition for SPR absorption is satisfied when $k_x = k_{SP}$,

$$k_x = \left(\frac{\omega}{c}\right)\sqrt{\varepsilon_P}\,\sin\theta_{INC} = \left(\frac{\omega}{c}\right)\sqrt{\frac{\varepsilon_M\varepsilon_L}{\varepsilon_M+\varepsilon_L}} = k_{SP} \tag{2}$$

where ω and c are the frequency of light and speed in a vacuum, respectively. A full detailed derivation and theoretical description of SPR can be found in Kretschmann's SPR theory[25-28] and discussed by Knoll[21] and Raether.[22, 23] The excitation of surface plasmons results in an attenuation of the reflected light. It is shown as a dip in the reflectivity curve for a 50 nm bare gold film (yellow curve in Figure 1b). When molecules bind on the noble metal film, a shift in the SPR angle (black tack in Figure 1b) is due to small changes in the local refractive index and thickness of the dielectric medium adjacent to the noble metal film. The Fresnel equations used to simulate the reflectivity curves are discussed in Chapter 2.

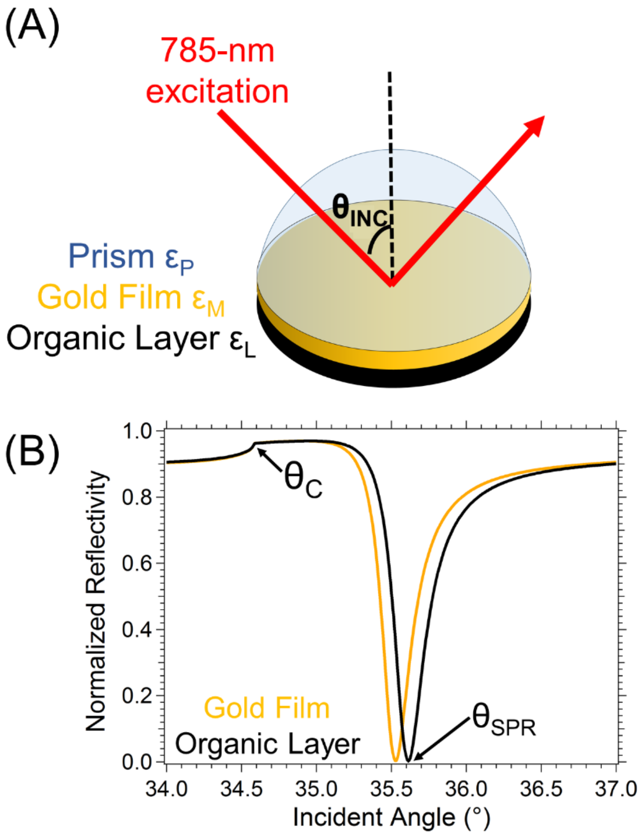

Figure 2. (A) Kretschmann configuration (prism/metal/air or sample) used for surface plasmon resonance (SPR) measurements. (B) Calculated SPR reflectivity curves for a sapphire prism (ε_P = 3.1043) / 50-nm gold film (ε_M = –22.855 + i1.4245) / air (ε_L = 1.000) (yellow curve) and a sapphire prism / 50-nm gold film / organic layer (ε_L = 2.4586) (black curve). The incident angle

of p-polarized 785-nm excitation light (θ_{INC}) that excites surface plasmons on the gold film is 35.53°. Upon adsorption of the organic layer, the SPR angle (θ_{SPR}) shifts to 35.60° due to the changes in the index of refraction and the thickness of the organic layer adjacent to the gold film. The critical angle (θ_C) is 34.59°.

References

1. Lewis, I. R.; Edwards, H. G. M., *Handbook of Raman spectroscopy : from the research laboratory to the process line / edited by Ian R. Lewis, Howell G.M. Edwards*. New York : Marcel Dekker: New York, 2001.

2. Long, D. A., *Raman spectroscopy*. McGraw-Hill: New York, 1977.

3. McCreery, R. L., *Raman spectroscopy for chemical analysis*. John Wiley & Sons: 2005; Vol. 225.

4. Smith, E.; Dent, G., Introduction, Basic Theory and Principles. In *Modern Raman Spectroscopy – A Practical Approach*, John Wiley & Sons, Ltd: The Atrium, Southern Gate, Chichester, West Sussex, England, 2005; pp 1-21.

5. Smith, E.; Dent, G., The Raman Experiment – Raman Instrumentation, Sample Presentation, Data Handling and Practical Aspects of Interpretation. In *Modern Raman Spectroscopy – A Practical Approach*, John Wiley & Sons, Ltd: The Atrium, Southern Gate, Chichester, West Sussex, England, 2005; pp 23-70.

6. Smith, E.; Dent, G., The Theory of Raman Spectroscopy. In *Modern Raman Spectroscopy – A Practical Approach*, John Wiley & Sons, Ltd: The Atrium, Southern Gate, Chichester, West Sussex, England, 2005; pp 71-92.

7. Raman, C. V.; Krishnan, K. S., A New Type of Secondary Radiation. *Nature* **1928,** *121* (3048), 501-502.

8. Ingle, J. D.; Crouch, S. R., *Spectrochemical analysis*. Prentice-Hall: Englewood Cliffs, N.J., 1988.

9. Smith, E.; Dent, G., Applications. In *Modern Raman Spectroscopy – A Practical Approach*, John Wiley & Sons, Ltd: The Atrium, Southern Gate, Chichester, West Sussex, England, 2005; pp 135-179.

10. Abbas, A.; Linman, M. J.; Cheng, Q., Sensitivity comparison of surface plasmon resonance and plasmon-waveguide resonance biosensors. *Sensors and Actuators B: Chemical* **2011,** *156* (1), 169-175.

11. Liedberg, B.; Nylander, C.; Lunström, I., Surface plasmon resonance for gas detection and biosensing. *Sensors and Actuators* **1983,** *4*, 299-304.

12. Lyon, L. A.; Musick, M. D.; Natan, M. J., Colloidal Au-Enhanced Surface Plasmon Resonance Immunosensing. *Analytical Chemistry* **1998,** *70* (24), 5177-5183.

13. Masson, J.-F., Surface Plasmon Resonance Clinical Biosensors for Medical Diagnostics. *ACS Sensors* **2017,** *2* (1), 16-30.

14. Peterlinz, K. A.; Georgiadis, R., In Situ Kinetics of Self-Assembly by Surface Plasmon Resonance Spectroscopy. *Langmuir* **1996,** *12* (20), 4731-4740.

15. Smith, E. A.; Corn, R. M., Surface Plasmon Resonance Imaging as a Tool to Monitor Biomolecular Interactions in an Array Based Format. *Applied Spectroscopy* **2003,** *57* (11), 320A-332A.

16. Smith, E. A.; Erickson, M. G.; Ulijasz, A. T.; Weisblum, B.; Corn, R. M., Surface Plasmon Resonance Imaging of Transcription Factor Proteins: Interactions of Bacterial Response Regulators with DNA Arrays on Gold Films. *Langmuir* **2003,** *19* (5), 1486-1492.

17. Smith, E. A.; Thomas, W. D.; Kiessling, L. L.; Corn, R. M., Surface Plasmon Resonance Imaging Studies of Protein-Carbohydrate Interactions. *Journal of the American Chemical Society* **2003,** *125* (20), 6140-6148.

18. Wang, Y.; Dostalek, J.; Knoll, W., Magnetic nanoparticle-enhanced SPR biosensor. *Procedia Engineering* **2010,** *5*, 1017-1020.

19. Wu, L.; Chu, H. S.; Koh, W. S.; Li, E. P., Highly sensitive graphene biosensors based on surface plasmon resonance. *Opt. Express* **2010,** *18* (14), 14395-14400.

20. Singh, P., SPR Biosensors: Historical Perspectives and Current Challenges. *Sensors and Actuators B: Chemical* **2016,** *229*, 110-130.

21. Knoll, W., Interfaces and thin films as seen by bound electromagnetic waves. *Annual Review of Physical Chemistry* **1998,** *49* (1), 569-638.

22. Raether, H., The dispersion relation of surface plasmons on rough surfaces; A comment on roughness data. *Surface Science* **1983,** *125* (3), 624-634.

23. Raether, H., *Surface plasmons on smooth and rough surfaces and on gratings*. Springer: 1988.

24. Kurihara, K.; Suzuki, K., Theoretical Understanding of an Absorption-Based Surface Plasmon Resonance Sensor Based on Kretchmann's Theory. *Analytical Chemistry* **2002,** *74* (3), 696-701.

25. Kretschmann, E., The angular dependence and the polarisation of light emitted by surface plasmons on metals due to roughness. *Optics Communications* **1972,** *5* (5), 331-336.

26. Kretschmann, E., Decay of non radiative surface plasmons into light on rough silver films. Comparison of experimental and theoretical results. *Optics Communications* **1972,** *6* (2), 185-187.

27. Kretschmann, E., Die bestimmung der oberflächenrauhigkeit dünner schichten durch messung der winkelabhängigkeit der streustrahlung von oberflächenplasmaschwingungen. *Optics Communications* **1974,** *10* (4), 353-356.

28. Kretschmann, E.; Raether, H., Notizen: Radiative Decay of Non Radiative Surface Plasmons Excited by Light. In *Zeitschrift für Naturforschung A*, 1968; Vol. 23, p 2135.

CHAPTER 2. THE EVOLUTION OF TOTAL INTERNAL REFLECTION RAMAN SPECTROSCOPY FOR THE CHEMICAL CHARACTERIZATION OF THIN FILMS AND INTERFACES

Charles K. A. Nyamekye[a,b], Jonathan M. Bobbitt[a,b], Qiaochu Zhu[a] and Emily A. Smith[*a,b]

[a] Department of Chemistry, Iowa State University, Ames, Iowa 50011, United States

[b] The Ames Laboratory, U.S. Department of Energy, Ames, Iowa 50011, United States

[*] Corresponding Author (esmith1@iastate.edu, 1-515-294-1424)

Modified from a manuscript published in Analytical and Bioanalytical Chemistry

Abstract

Total internal reflection (TIR) optical spectroscopies have been widely used for decades as non-destructive and surface-sensitive measurements of thin films and interfaces. Under TIR conditions, an evanescent wave propagates into the sample layer within a region approximately 50 nm to 2 μm from the interface, which limits the spatial extent of the optical signal. The most common TIR optical spectroscopies are fluorescence (i.e., TIRF) and infrared spectroscopy (i.e., attenuated total reflection infrared). Despite the first report of TIR Raman spectroscopy appearing in 1973, this method has not received the same attention to date. While TIR Raman methods can provide chemical specific information, it has been outshined in many respects by surface-enhanced Raman spectroscopy (SERS). TIR Raman spectroscopy, however, is garnering more interest for analyzing the chemical and physical properties of thin polymer films, self-assembled monolayers (SAMs), multilayered systems, and adsorption at an interface. Herein we discuss the early experimental and computational work that laid the foundation for recent developments in the use of TIR Raman techniques. Recent applications of TIR Raman spectroscopy as well as modern TIR instruments capable of measuring monolayer-sensitive vibrational modes on smooth metallic surfaces are also discussed. The use of TIR Raman

spectroscopy has been on a rise and will continue to push the limits for chemical specific interfacial and thin film measurements.

Introduction

The chemical characterization of surfaces and interfaces is indispensable for state-of-the-art research in separations, heterogeneous catalysis, energy harvesting and storage devices, and electrochemistry. In order to understand the properties of interfaces, many destructive and non-destructive microscopic and spectroscopic methods have been extensively deployed. Electron microscopy techniques and scanning probe microscopies (e.g., atomic force microscopy) can provide primarily structural information about an interface with atomic spatial resolution. While these techniques offer an unrivalled spatial resolution, they provide limited chemical information. They also have a limited ability to measure dynamic information and structural information below the top-most surface layer without destructive sample preparation methods.

Total internal reflection (TIR) vibrational spectroscopies (e.g., attenuated total reflection infrared spectroscopy and TIR Raman spectroscopy) can non-destructively measure chemical composition and molecular orientation at an interface with minimal sample preparation. TIR vibrational spectroscopies, like other TIR optical spectroscopies, use evanescent waves to provide interfacial selectivity and sensitivity. The fundamental principles behind TIR Raman spectroscopy have been reviewed by Bain et al. [1-3]. Briefly, the TIR phenomena occurs at an interface between two dielectric materials of differing indices of refraction: η_1 (for the total internal reflection element or prism) and η_2 (for the sample), where η_1 is greater than η_2. The incident light travels from the dielectric material with a higher refractive index to the lower refractive index material at an angle greater than or equal to the critical angle θ_c, as described by Snell's law:

$$\theta_c = sin^{-1}\left(\frac{\eta_2}{\eta_1}\right) \tag{1}$$

At the critical angle, there is no transmitted wave that propagates through the sample η_2, but there is an evanescent wave generated at both sides of the interface. The evanescent wave travels parallel to the interface and exponentially decays from the interface. The penetration depth of the evanescent wave, d_p, is where the intensity drops to a value of 1/e, and on the sample side is given by:

$$d_p = \frac{\lambda_0}{2\pi}\frac{1}{\sqrt{\eta_1^2 sin^2\theta_i - \eta_2^2}} \tag{2}$$

where λ_0 is the wavelength of light with an incident angle θ_i. The properties of the evanescent wave confine the measured vibrational signals to the interface. Comparing TIR Raman and infrared signals, in addition to different selection rules, Raman spectroscopies have the benefit of using shorter wavelengths of light. This results in a smaller penetration depth of the evanescent wave and an increased surface sensitivity. Also, the penetration depth of the evanescent wave varies across the infrared spectrum because the excitation wavelength is varied to collect the absorption spectrum. Raman scattering produces minimal spectral interference from peaks associated with water, and maybe better suited for aqueous samples. On the other hand, IR signals generally result in better detection limits. Table 1 summarizes key similarities and differences between ATR-IR and TIR Raman spectroscopies, and serves as a guide to when either technique may be preferred.

Table 1. Selected comparisons of attenuated total reflection infrared (ATR-IR) and total internal reflection (TIR) Raman spectroscopies.

ATR-IR	**TIR Raman**
Requires a change in the dipole moment	Requires a change in polarizability
Adsorption of IR radiation	Inelastic scattering (measures relative frequencies)
Excitation light in mid-IR region, reflective optics generally required	Range of excitation wavelengths may be used (UV, visible, or IR)
d_p varies with the excitation wavelength, which may complicate ATR-IR depth profiling measurements	A single excitation wavelength is used, which may simplify depth profiling measurements
d_p is generally greater than 1 µm	d_p is generally in the range of 100 nm to 1 µm
Water background from sample may be problematic	Fluorescence background from sample or prism may be problematic
Collected spectral range often dependent on the ATR crystal (ex: diamond 45,000-10 cm^{-1}; α-Al_2O_3 50,000-1,780 cm^{-1}; ZnSe 20,000-650 cm^{-1}; Ge 5,500-830 cm^{-1})	Possible to measure low Raman shifts with many prism types
Signal enhancement is generally not needed	Raman scattering signal may be low, signal enhancement may be required
Commercial instruments are readily available	Home-built instruments currently in use
Measurement of all types of samples including organic and inorganic solids, liquids, powders, pastes, gases, as well as biological specimens	
Self-assembled monolayer detection has been reported	
Real-time adsorption measurements can be performed	

Even though the first reports of TIR Raman spectroscopy occurred approximately a half century ago, relatively few papers have been published covering TIR Raman spectroscopy compared to other TIR optical spectroscopies. This is partly due to the discovery and subsequent focus on surface-enhanced Raman spectroscopy (SERS) [4-8]. While SERS measured at a roughened noble metal surface provides large signal enhancements, it has drawbacks for some applications. These include: a signal enhancement that can only be achieved at a couple of nanometers distance away from the plasmon-supporting surface, thus limiting the distance over which the signal can be achieved and the thickness of the sample that can be studied; and the need for a roughened substrate, which prohibits the study of smooth films, such as those found in many electronic devices (e.g., polymer-based organic light-emitting diodes and organic solar cells) [9,10]. (Similarly, tip-enhanced Raman spectroscopy can also be used to study interfaces, but for some applications, it has the disadvantages of SERS as well as other scanning probe microscopies).

In this review, the fundamental work that paved the way for recent advances in TIR Raman spectroscopy is briefly outlined [11-20]. In recent years, TIR Raman spectroscopy has received renewed interest due in part to improvements in Raman instrumentation that have expanded the types of samples that can be studied [21-27]. Recent advances and applications of TIR Raman spectroscopy will also be covered including studies of thin polymer films [28-35], SAMs [2,36], phospholipid bilayers at liquid interfaces [25], and hydrogen bonding at silica/water or ice interfaces [24]. TIR Raman spectroscopies have been combined with smooth [37-43] and rough [44,45,40,46,47] noble metal substrates for signal enhancement; the latter is equivalent to SERS under TIR conditions. Only the former will be covered in detail in this review.

Modeling the TIR Raman Signal

Prior to the first experimental demonstration of TIR Raman spectroscopy, the appropriate theory for modeling the signal was reported. The reflected light from the interface can be modeled by Fresnel reflectivity coefficients, R_p and R_s, where the subscript refers to the polarization of the incident light. P-polarized light has an electric field oriented parallel to the plane of incidence and s-polarized light has an electric field perpendicular to that plane. Figure 1a shows the Fresnel reflectivity curves as a function of the incident angle at a sapphire prism/organic layer interface. As expected, the 57.551° critical angle for this interface is marked by a sharp increase in the reflected light intensity. Hansen [14] derived the equations for the electric field intensity under conditions of TIR illumination in two-, three-, or multi-layered systems. The oscillation of the produced electric field in the x and z directions results from p-polarized incident light and the oscillations in the y plane results from s-polarized light (Figure 1b). Thus, controlling the polarization of the light can be used to measure, for example, the orientation of molecules at an interface. The electric fields in the y and z directions are maximum at the critical angle for the sapphire prism/organic layer interface under TIR (Figure 1b).

D’Hooge et al. [48,49] generated the theory of Raman scattering that is produced by evanescent excitation. The Raman scattering generated at the interface containing a homogenous sample is proportional to the electric field intensity within the sample and the depth over which the Raman signal is collected. At a given incident angle, the depth over which the Raman scattering is generated, D_{RS}, decreases twice as fast as the evanescent wave since the Raman scattering is proportional to the electric field intensity:

$$D_{RS} = \frac{d_p}{2} \tag{3}$$

where d_p is the penetration depth expressed in equation 2. The depth over which the Raman scattering is generated can be adjusted at different incident angles above the critical angle to perform axial depth profiling measurements (Figure 1c). When the incident angle changes from 58° to 59°, D_{RS} changes by ~186 nm for a sapphire prism/organic layer interface. This represents an improvement compared to confocal Raman spectroscopy, which provides an axial spatial resolution of hundreds of nanometers to microns. Confocal Raman spectroscopy is also limited in its ability to measure thin films, especially in the presence of a bulk layer that also produces a Raman signal. The axial spatial resolution at the interface can also be tuned by controlling the variables of wavelength and refractive index of the interfacial materials. Depending on these variables, the maximum D_{RS} typically ranges from tens of nanometers to a few microns.

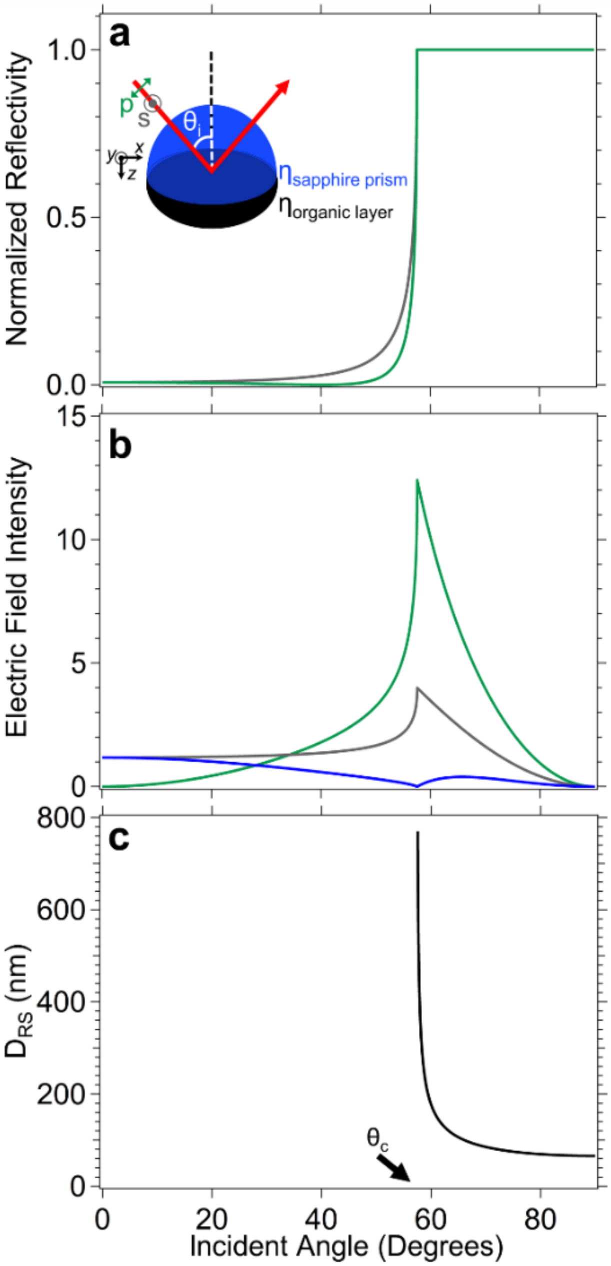

Figure 1. Calculated **a** reflected light, **b** electric field intensity, and **c** depth over which Raman scattering is generated D_{RS} as functions of incident angle for a sapphire (η = 1.7619) / organic layer (η = 1.4868) interface at λ_0 = 785 nm. P-polarized incident light (**a**, green) produces electric fields oscillating in the x- (**b,** blue) and z-planes (**b**, green) and s-polarized incident light (**a**, gray) produces an electric field orientated in the y direction (**b**, gray). The properties of the Raman signal depend on whether it is collected on the prism side or sample side of the interface.

Experimental TIR Raman Spectroscopy

TIR Raman spectroscopy was first experimentally demonstrated by Ikeshoji et al. to analyze a liquid of carbon disulfide using a flint-glass prism [50]. Figure 2 shows their TIR Raman spectra collected over a range of incident angles. The Raman scattering is at a maximum near the critical angle (θ_c = 70.8°) and decreases with increasing incident angle (Figure 2a). This is due to the aforementioned decrease in the electric field intensity and D_{RS} at larger incident angles. Ikeshoji and coworkers showed that TIR Raman spectroscopy can provide an adequate signal from a solution at an interface and the ability to model the Raman scattering as the incident angle is changed.

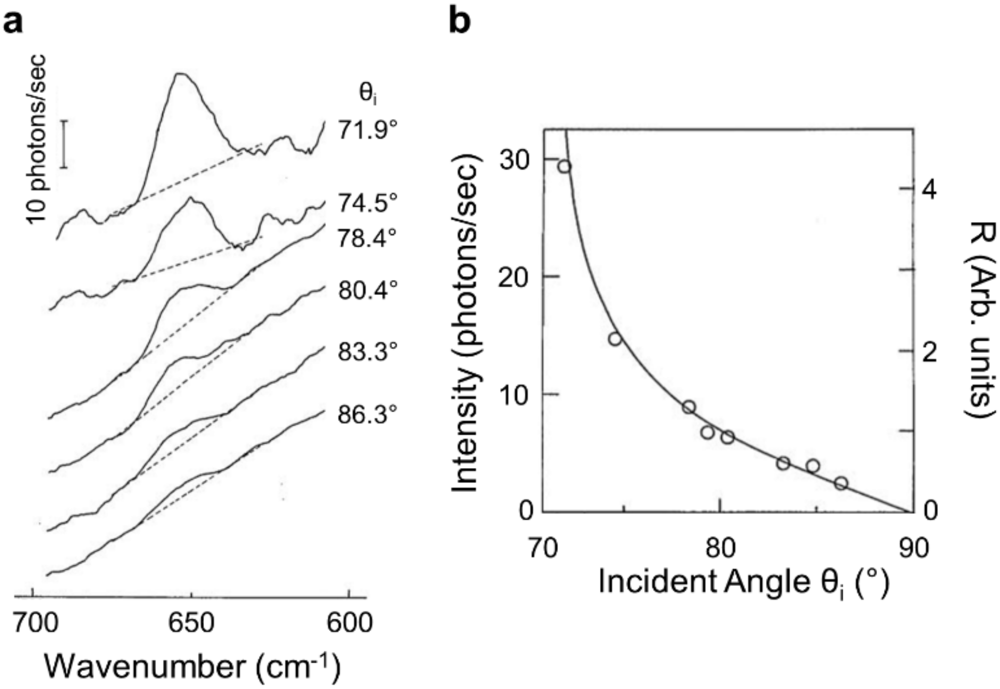

Figure 2. a TIR Raman spectra of carbon disulfide solution (η_{sample} = 1.6180) at a hemispherical flint glass (η_{glass} = 1.7130) prism illuminated with 632.8 nm light. **b** Experimentally measured TIR Raman scattering intensities of the 654 cm^{-1} peak (symbol) and calculated fit (solid line, details of the fit can be found within the reference) as functions of incident angle. The critical angle of the hemispherical flint glass/carbon disulfide solution was 70.8°. Reprinted from [Ikeshoji T, Ono Y, Mizuno T (1973) Total Reflection Raman Spectra; Raman Scattering due to the Evanescent Wave in Total Reflection. Appl. Opt. 12 (10):2236-2237. doi:10.1364/AO.12.002236] (ref. [50]), with permission from AIP Publishing.

In 1993, Nickolov et al. used TIR Raman spectroscopy to study the O-H stretching vibrational bands of water (3200 and 3420 cm^{-1}) at two interfaces [51]. One was a hydrophobic surface composed of a 25-layer Langmuir-Blodgett film of ω-tricosenoic acid adjacent to a sapphire prism, and the second interface was a hydrophilic surface that consisted of only the sapphire prism. They concluded that the O-H Raman band changes at the hydrophobic interface compared to the hydrophilic interface due to an increase in the hydrogen bonding of water molecules at the interface with ω-tricosenoic acid.

In order to achieve high axial resolution depth profiling with TIR Raman spectroscopy, the penetration depth of the evanescent wave must be carefully controlled. This requires accurate control of the incident angle of light upon the interface. In 2010, a scanning angle (SA) Raman spectrometer with 785 nm excitation was reported for measuring interfacial phenomena with a 0.05° angle resolution using adjustable translation stages and a variable angle galvanometer mirror [52]. This angle resolution correlates to probing analytes near a planar interface with tens of nanometer spatial resolution perpendicular to the interface (i.e., axial resolution) [53-55]. As a proof of concept, this instrument was used to collect the Raman scattering from a zinc selenide prism /benzonitrile interface over a range of 35-180 nm with 1 nm axial resolution. Compared to a conventional confocal Raman microscope, the resolution of the SA Raman technique shows a 1000-fold improvement. A 532 nm SA Raman instrument was also reported (Figure 3) that had mechanical design improvements and the benefits associated with the use of a shorter excitation wavelength (e.g., resonant enhancement, decrease in the acquisition time, and smaller D_{RS}) [56]. Resonance enhancement of the TIR Raman signal has been shown using a 532 nm laser to measure visible-light absorbing organic polymer photovoltaic films [57].

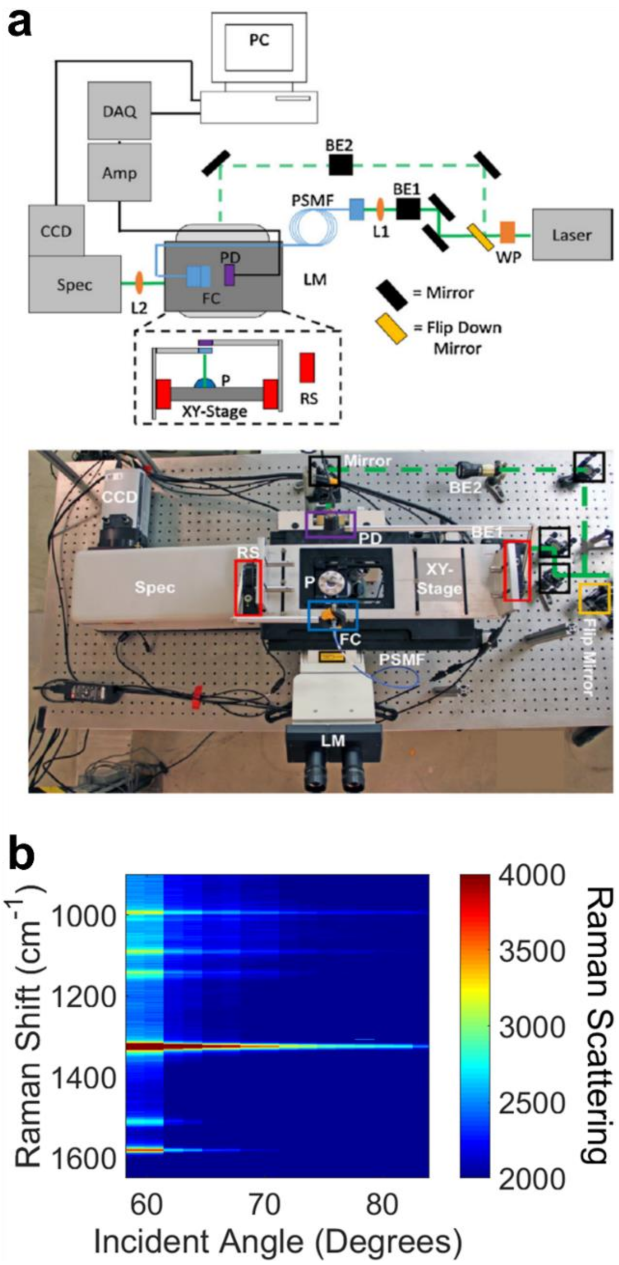

Figure 3. a Schematic diagram and picture of a 532 nm SA Raman instrument built around an optical microscope. Amp: amplifier, BE: beam expander, CCD: charge-coupled device, DAQ: data acquisition device, FC: fiber collimator, LM: Leica microscope, L1: aspheric focusing lens, L2: collection lens, PC: computer, PSMF: polarization-maintaining single-mode fiber optic, P: prism, PD: photo-diode, RS: rotational stage, Spec: spectrometer, WP: half wave-plate. Reprinted from Anal. Chim. Acta, 848, Lesoine MD, Bobbitt JM, Zhu S, Fang N, Smith EA, High angular-resolution automated visible-wavelength scanning angle Raman microscopy, 61-66 (ref. [56]), Copyright (2014), with permission from Elsevier. **b** SA Raman spectra of nitrobenzene at a sapphire interface. The color amplitude scale represents the Raman scattering intensity. As expected, the largest TIR Raman signal for all Raman peaks is measured near the critical angle of 61.2° and exponentially decays towards higher incident angles.

Polymer and Waveguide Samples

Polymer films are one of the most commonly studied samples using TIR Raman spectroscopy. Many of these polymer films are waveguides. A waveguide consists of a dielectric layer with a thickness greater than or equal to $\frac{\lambda_0}{2\eta_2}$, where λ_0 is the excitation wavelength and η_2 is the refractive index of the polymer. The electric field intensity calculated within a 1 µm polymer waveguide film ($\eta_2 = 1.5099$) is plotted as a function of incident angle in Figure 4a. There is a maximum in the electric field intensity at two angles: 50° (labeled mode 1) and 57° (labeled mode 0). At both angles, the electric field intensity can be calculated as a distance across the interface (Figure 4b, where the polymer is from 1000 to 2000 nm in this calculation). The 1 µm polymer film acts as a radiative or "leaky" waveguide, which is caused by the interference from counter propagating reflections. The number of antinodes within the waveguide layer in the electric field intensity is given by the mode integer (Figure 4b). Since the scattering intensity is proportional to the electric field intensity, this indicates that the Raman signal is not generated uniformly throughout the waveguide. In addition, the profile of the Raman scattering generated throughout the film is different at 50° and 57°. The spatial dependence of the generated Raman signal within the waveguide film is influenced by the refractive index and thickness of the polymer as well as the excitation wavelength, incident angle, and polarization of the excitation light. Harnessing the spatial dependence of the generated Raman signal within waveguide samples as a function of incident angle, SA Raman spectroscopy can be used to determine physical properties of the waveguide such as the refractive index, thickness and composition.

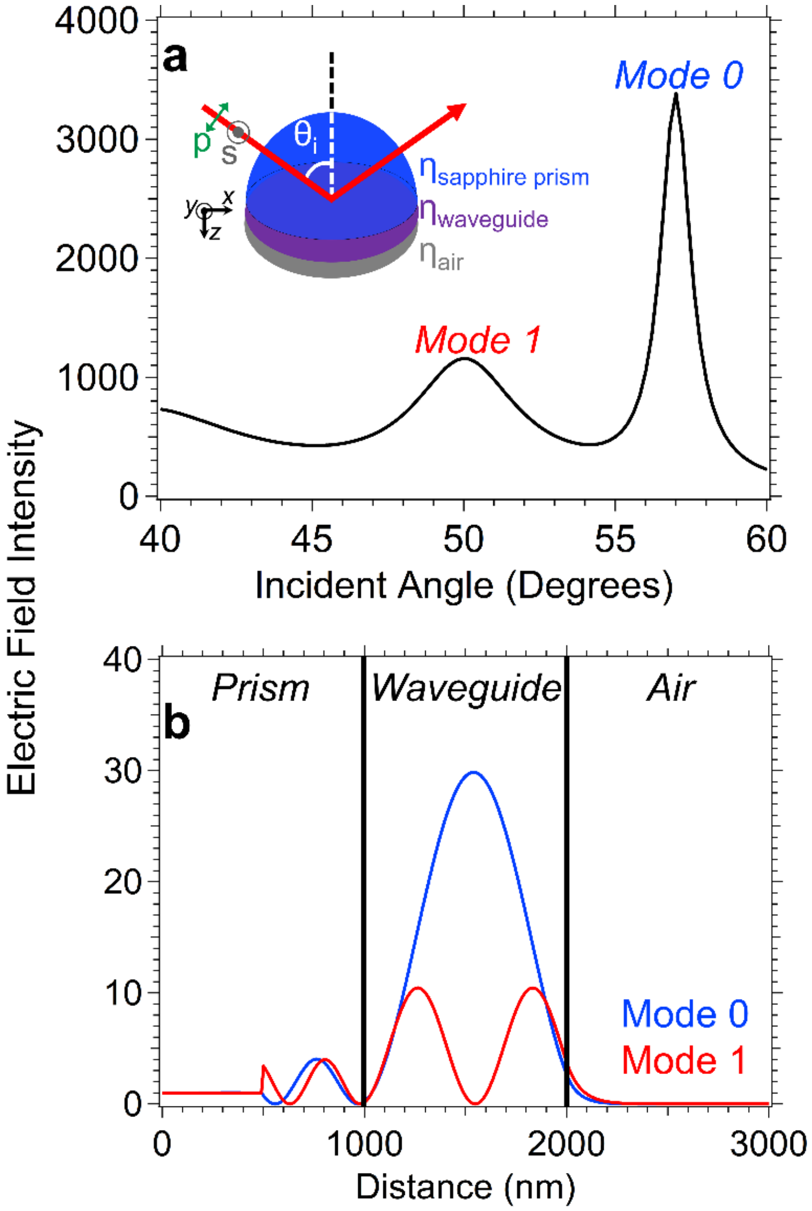

Figure 4. Calculated electric field intensity for a 1 μm polymer waveguide film ($\eta_2 = 1.5099$) as functions of **a** the incident angle of s-polarized 785 nm light and **b** the distance from the interfacial layers. The red curve in **b** corresponds to mode one at 50° and the blue curve corresponds to mode zero at 57°. The vertical black lines represent the interface locations.

Rabolt and coworkers [58-62] studied the waveguide nature of thick polymer films and multilayered polymer films. Their initial findings showed that the excitation light can be coupled into a polymer waveguide film and produced Raman spectra with 1 to 2 orders of magnitude better signal-to-noise ratio than a bulk sample [58]. Following this study, Rabolt et al, studied bilayer films consisting of poly(methyl methacrylate) on poly(vinyl alcohol) and polystyrene on poly(vinyl alcohol) [59,63]. They calculated the electric field as a function of the distance throughout the dielectric waveguide bilayer. By controlling the incident angle of light, they excited waveguide mode 0 or 1 and collected the Raman spectra of bilayer films [59]. Subsequent work reported small molecule diffusion within the waveguide [64], and a variety of polymer types at different thicknesses and using different excitation wavelengths [60-62].

In 1980, Carius et al. applied TIR Raman spectroscopy to evaluate the degree of polymerization in a 6 μm thick polystyrene film prepared by thermal polymerization of a styrene monomer directly onto a hemispherical glass prism [65]. The TIR Raman spectra were acquired with 488 nm excitation and the incident angle was used to control the depths over which the Raman signal was collected, which was confirmed by modeling the intensities of the 3060 cm^{-1} band (CH stretch). They studied the incident angle from 67.5° to 77.5° with d_p values ranging from 125 to 400 nm. The ratios of the Raman intensities of the 1633 cm^{-1} (monomer, C=C band) and 1603 cm^{-1} (polystyrene, ring stretching mode) peaks were used to determine the ~l% monomer composition that remained after polymerization.

Also in 1980, Iwamoto et al. showed that TIR Raman spectroscopy can be used to measure a polymer bilayer film [66-68]. Figure 5a shows the TIR Raman spectroscopy apparatus they used to collect the data for bilayer films composed of 0.05 μm polystyrene (closest to the internal reflection element) and 30 μm polyethylene (Figure 5b). Figure 5b reveals only peaks corresponding to polyethylene were measured when the excitation light passes straight through the sample, while the same film illuminated under TIR produced a spectrum corresponding to polystyrene. Under TIR no peaks for polyethylene were measured since its location was beyond the distance over which the Raman signal was collected [67]. Additionally, Iwamoto and coworkers [68,67] measured the Raman signal for a bilayer film as the thickness of the polymer closest to the internal reflection element increased. The TIR Raman spectra of polystyrene (closest to the internal reflection element) and polycarbonate bilayer films were collected. They showed that there is a decrease in the TIR Raman intensity ratio of the 890 cm^{-1} polycarbonate to the 1001 cm^{-1} polystyrene peaks with increasing polystyrene thickness as the polycarbonate layer moves farther away from the internal reflection element.

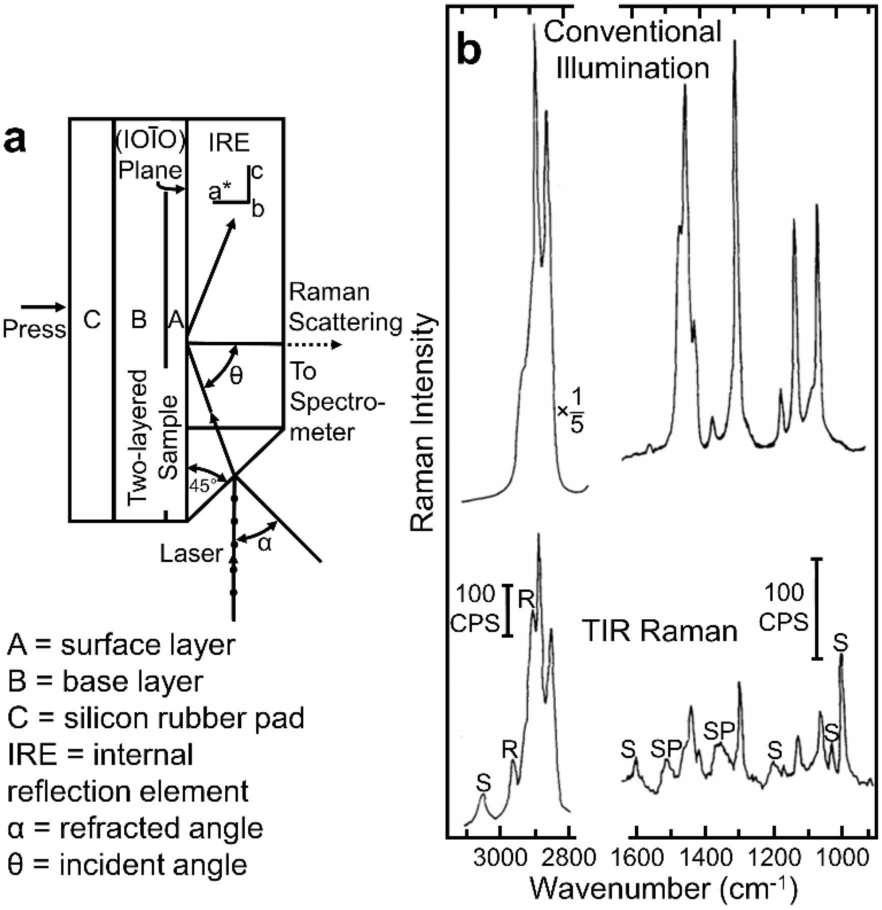

Figure 5. **a** Sample configuration used to collect **b** the Raman spectra of 0.05 µm polystyrene (surface layer) coated on top of 30 µm polyethylene (base layer) film collected using (top of the figure) the conventional illumination through the sample and (bottom of the figure) the TIR illumination. The polystyrene, sapphire, and silicon rubber peaks (sample holder) are denoted with a S, SP, and R, respectively. The TIR Raman spectrum is collected at the incident angle of 64.8°. Reprinted from [Iwamoto R, Miya M, Ohta K, Mima S (1981) Total internal reflection Raman spectroscopy. J. Chem. Phys. 74 (9):4780-4790. doi:10.1063/1.441757] (ref. [67]), with the permission of AIP Publishing.

More recently, SA Raman spectroscopy with a high incident angle resolution was used to analyze solid-solid interfaces composed of blended and conjugated polymer films in organic photovoltaic devices. Meyer et al. used the SA Raman technique to measure poly(3-hexylthiophene):phenyl−C61−butyricacid methyl ester blend morphology on varying photovoltaic device substrates, such as sapphire, Au, and indium tin oxide (ITO) [69]. Compared to conventional Raman spectroscopy, the TIR Raman signals were 4× larger and enhanced at the incident angle of 35.00°. This incident angle is close to the critical angle of 34.581° for a sapphire/air interface. The authors concluded that the molecular order of poly(3-hexylthiophene) depended on the underlying substrate based on the peak width of the 1447 cm^{-1} thiophene C=C stretch, which was different for the three substrates that were studied.

Bobbitt et al. measured the chemical content and the location of buried interfaces of polymer bilayer and trilayer waveguides composed of poly(methyl methacrylate)/polystyrene and poly(methyl methacrylate)/polystyrene/poly(methyl methacrylate), respectively (Figure 6) [70]. The thicknesses of the poly(methyl methacrylate) layer closest to the prism and the poly(methyl methacrylate) layer farthest from the prism were varied between 160 to 420 nm in the trilayer system while the polystyrene layer was kept at a constant thickness of 180 nm. Figure 6a-f shows the SA Raman data for trilayer films and the fit of the SA Raman signal to the electric field calculated using three-dimensional finite-difference time-domain methods. A recursive algorithm for calculating the electric field within each individual component in the multilayered film (with a 10 nm step size) was developed and used to model the SA Raman data for the bilayer and trilayer polymer films. The authors found that the SA method provided a 7 to 80 nm axial spatial resolution for probing the buried interfaces between the polymer layers in the trilayer system [70]. Furthermore, Bobbitt and coworkers simultaneously determined the refractive indices, thicknesses, and the chemical compositions of mixed polymer films consisting of polystyrene-block-poly(methyl methacrylate):poly(methyl methacrylate) at several volume ratios [71].

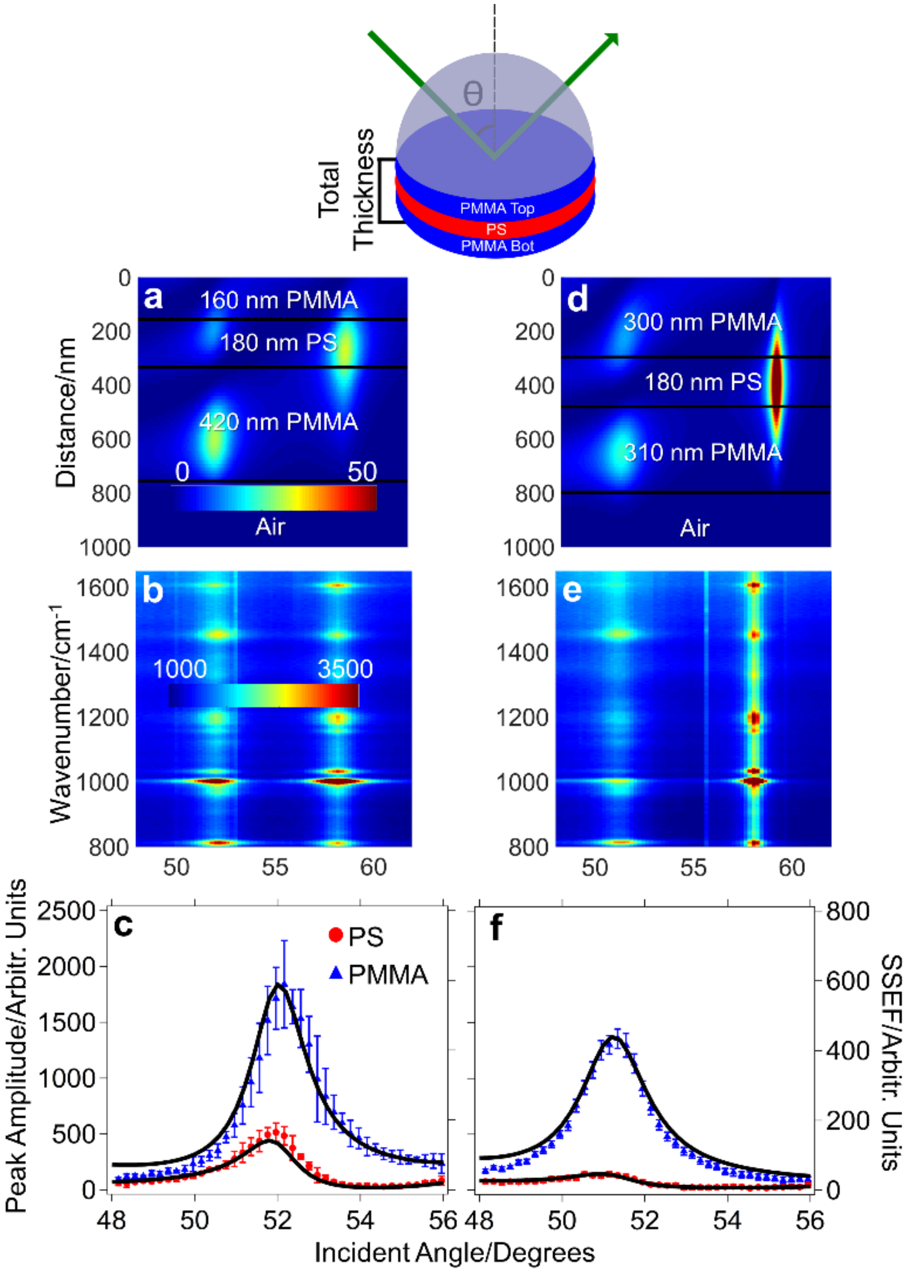

Figure 6. Trilayer films are composed of **a-c** 160 nm poly(methyl methacrylate)/180 nm polystyrene/420 nm poly(methyl methacrylate) and **d-f** 300 nm poly(methyl methacrylate)/180 nm polystyrene/310 nm poly(methyl methacrylate). **a,d** Calculated electric field intensity plots as functions of incident angle and distance from the prism interface for the trilayer films. The color scale represents the electric field intensity. **b,e** SA Raman spectra of trilayer films with the

aforementioned thicknesses plotted on a color scale representing the SA Raman scattering intensity. **c,f** Plots of the 1605 cm^{-1} polystyrene and 812 cm^{-1} poly(methyl methacrylate) peak amplitudes as a function of incident angle. The black line represents the best sum squared electric field (SSEF) fit to the experimental data. Reproduced from Bobbitt JM, Smith EA (2017) Extracting interface locations in multilayer polymer waveguide films using scanning angle Raman spectroscopy. J. Raman Spectrosc. 49 (2):262-270. doi:10.1002/jrs.5275 (ref. [70]), Copyright (2017), with permission from John Wiley and Sons.

Surface-Plasmon-Polariton-Enhanced (SPP) Raman Spectroscopy

Plasmon-supporting substrates can be incorporated into TIR Raman measurements to study phenomena occurring at the metal interface as well as to enhance the signal. Under TIR conditions, a noble metal film (e.g., Au, Ag, Pt) adjacent to a prism can support non-radiative electromagnetic surface waves (surface plasmon polaritons, SPPs) when the electron oscillation frequency of the metal film matches the wavevector of the incident light. Only SPP Raman spectroscopies utilizing smooth planar noble metal films will be discussed herein. Burstein and collaborators in 1969 were the first to propose the use of Ag films in a TIR configuration to enhance the Raman scattering intensity of adsorbates [72]. Ushioda and collaborators used both experiment and theory to conclude that there is a significant enhancement of the Raman scattering intensity of adsorbates on a metal surface. They found a 200× increase in the Raman scattering intensity of a BK-7 prism/Ag film/pyridine sample/air interface in the Kretschmann configuration with a 514.5 nm laser beam, after finding that a 57 nm thick Ag film generated the largest electric field [73]. Furthermore, they found that the angle where propagating surface plasmons were excited in the metal film (the SPR angle) slightly differed from the angle where the highest Raman signal was generated due to the difference in the incident and scattered light energies.

Modern SPP Raman spectroscopy instruments can collect spectra as a function of incident angle with monolayer sensitivity. The SPP Raman signal of a 1.25 M pyridine solution at a Au film interface as a function of incident angle is shown in Figure 7a [37]. The signal is well-modeled by the calculated values for the electric field and D_{RS} (Figure 7b-d). The Raman scattering is enhanced 4-fold at the angle where SPPs are most efficiently excited in the metal film [37]. SPP Raman spectroscopy was also demonstrated by Etchegoin et al. [74] using Nile blue adsorbed on 50 nm Au and Ag films at an air interface and excited with 647 nm light. In addition, SPP Raman scattering from a smooth silver film with 532 nm excitation was used to measure a small molecule-protein interaction at the metal surface [75]. The 1631 cm^{-1} Raman band (aromatic C=C stretch) of Atto610-labeled biotin was observed upon binding to the protein avidin. Subsequently, the authors added silver colloids to generate the surface roughness required for SERS.

A limitation to measuring the Raman signal at SPP-supporting films is that only p-polarized excitation can be used to enhance the Raman signal, unless the sample is a waveguide or is adsorbed to a waveguide surface. P- and s-polarized excitation light can be used to collect Raman signals generated from waveguide modes, which can provide information about molecular orientation [76]. By scanning the incident angle of light while simultaneously collecting the Raman signal from a plasmon waveguide sample, the angle where the maximum Raman signal was generated was used to build a calibration curve for polymer thickness [77]. A follow-up of this work conducted by Bobbitt and coworkers [78], showed that a similar analysis could be performed by simultaneously scanning the incident wavelength and angle of light.

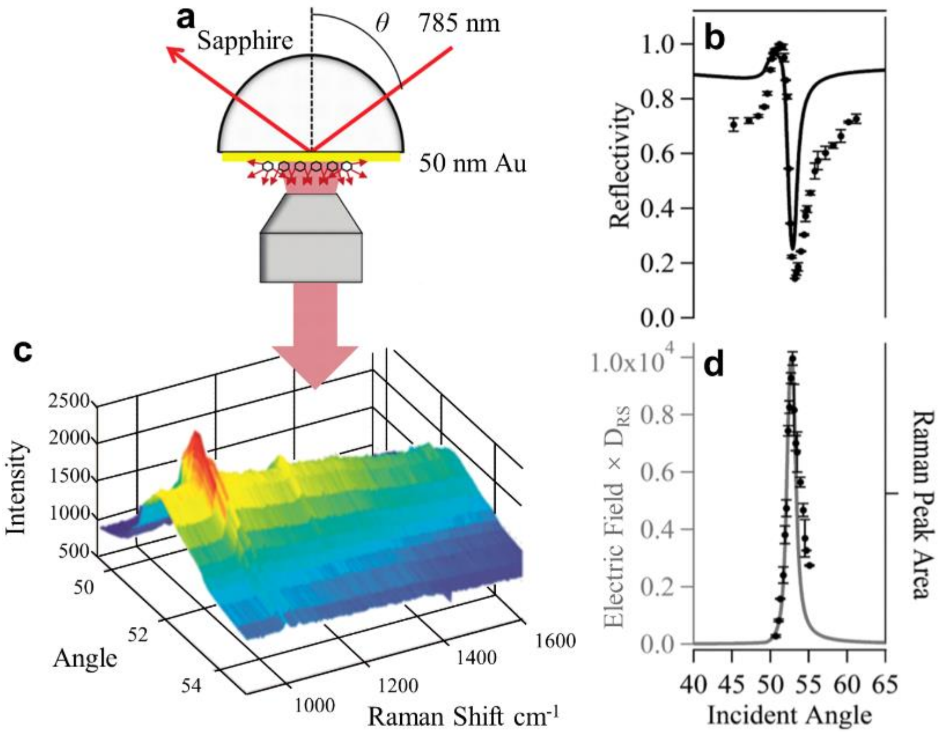

Figure 7. a Sample geometry used to measure aqueous pyridine solution at a sapphire prism/50 nm Au/pyridine solution interface with the Raman signal collected on the sample side. **b** Experimentally measured (dotted symbol) reflected light intensity and Fresnel reflectivity calculations (solid line). **c** SPP Raman spectra of pyridine collected with 785 nm excitation. **d** Calculated mean square electric field (MSEF) × D_{RS} (gray) fit to the SPP Raman peak areas (black, symbols). Reprinted (adapted) with permission from McKee KJ, Meyer MW, Smith EA (2012) Near IR Scanning Angle Total Internal Reflection Raman Spectroscopy at Smooth Gold Films. Anal. Chem. 84 (10):4300-4306. doi:10.1021/ac203355a, (ref. [37]). Copyright (2012) American Chemical Society.

Directional Raman Scattering

Large collection efficiencies are achieved when the Raman signal is collected on the prism side of a prism/metal/sample interface under TIR conditions (Figure 8a). This is due to the directionality of the scattered light in the form of a hollow cone, called the surface plasmon polariton (SPP) cone (Figure 8b). Simon and Guha [79] were the first to report an experimentally measured SPP cone. They determined that the directional Raman signal collected on the prism side (Figure 8c) was larger than the Raman signal measured on the air side. Braundmeier and Tomaschke [80] proposed two mechanisms for the generation of the SPP cone observed on a Ag film under TIR conditions: 1) momentum conserving optical coupling and 2) scattering from surface irregularities or roughness coupling [80]. The excitation of surface plasmons in the plane of the metal film (in-coupling) and the scattered light through the prism (out-coupling) results in the directional emission of the SPP cone at a sharp and defined angle. Equation 4 illustrates the incident angle θ_{inc} that results in the SPP cone, where η_1 is the refractive index of the prism and ϵ is the dielectric function of the metal film.

$$\theta_{inc} = arcsin\left[\eta_1^{-1}\left(\frac{\epsilon}{1+\epsilon}\right)^{\frac{1}{2}}\right] \tag{4}$$

Otto and coworkers experimentally demonstrated directional Raman scattering from carbon contaminates and Rhodamine 6G adsorbed on Ag films by collecting the signal from the full SPP cone radiating from a Weierstrass prism (hyperhemispherical prism) [81]. Byahut and Furtak designed an instrument to collect the directional Raman signal of *p*-nitrosodimethylaniline adsorbed on smooth and rough Ag films [82,40,83]. They showed that the highest intensity of the 1613 cm^{-1} ring stretching mode of *p*-nitrosodimethylaniline occurred at the incident angle of 44.29°, the angle where the SPP cone is generated. Futamata and coworkers [84,41,85-87] demonstrated monolayer sensitive Raman measurements of copper phthalocyanine monolayer on Au, Ag and Cu metallic substrates by means of collecting the directional Raman signal generated from the prism side of the Otto configuration (prism/air gap/metal/sample).

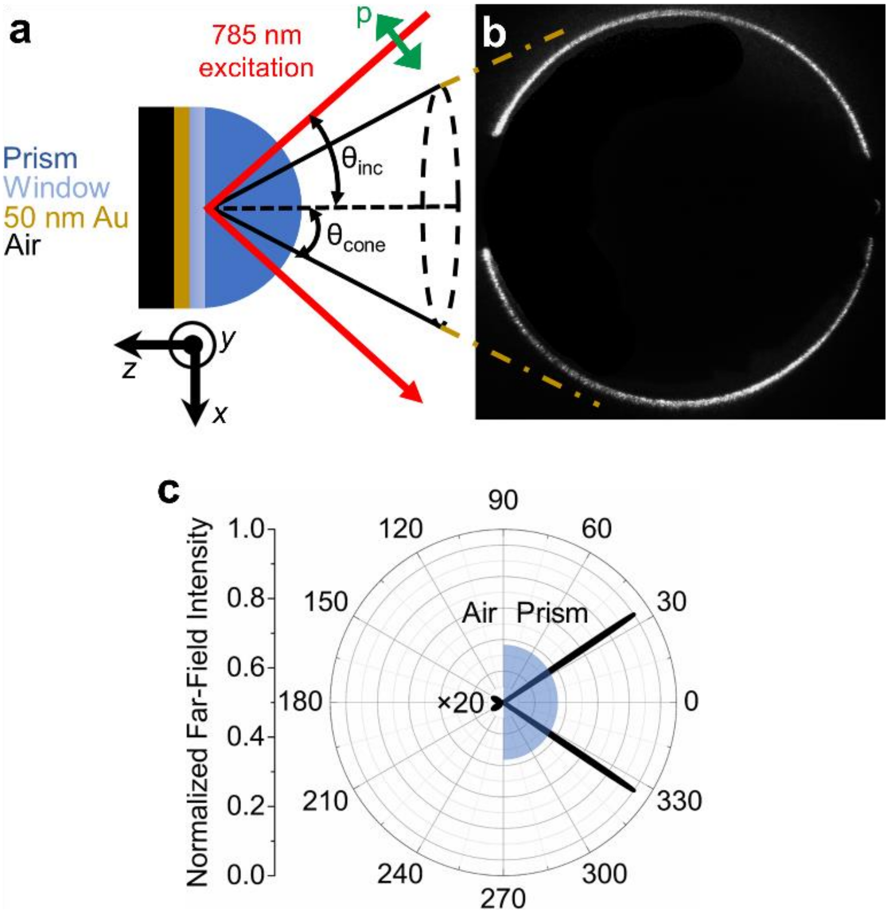

Figure 8. a The Kretschmann configuration (hyperhemispherical prism/50 nm Au/air) used to collect **b** the surface-plasmon-polariton cone (SPP cone) acquired with a 785 nm laser at the incident angle (θ_{inc}) of 35.53°. **c** Calculated and normalized far-field angular radiation pattern depicting the directionality of the 785 nm Rayleigh scattered light through the prism. The far-field intensity on the air side was multiplied by 20.

While measurements of the SPP cone were reported by Braundmeier and Tomaschke [80] and Simon and Guha [79] in the 1970s, they did not quantify the SPP cone properties. Nyamekye and coworkers developed a directional Raman spectroscopy instrument (Figure 9a) capable of collecting the full Raman scattering signal generated from the SPP cone as a function of incident angle while simultaneously collecting an image of the SPP cone [38,39]. The instrument had monolayer Raman sensitivity and the SPP cone encoded the same information measured by surface plasmon resonance. Self-assembled monolayers, thin polymer films and waveguide polymer films were measured on the same instrument [38,39]. Since the instrument design utilized translational stages (as opposed to the rotational stages commonly used in SPR sensing), faster acquisition times with a 0.06° angle resolution were possible. By utilizing a smooth planar metallic film, simple and accurate models of the experimental results were possible (Figure 9e).

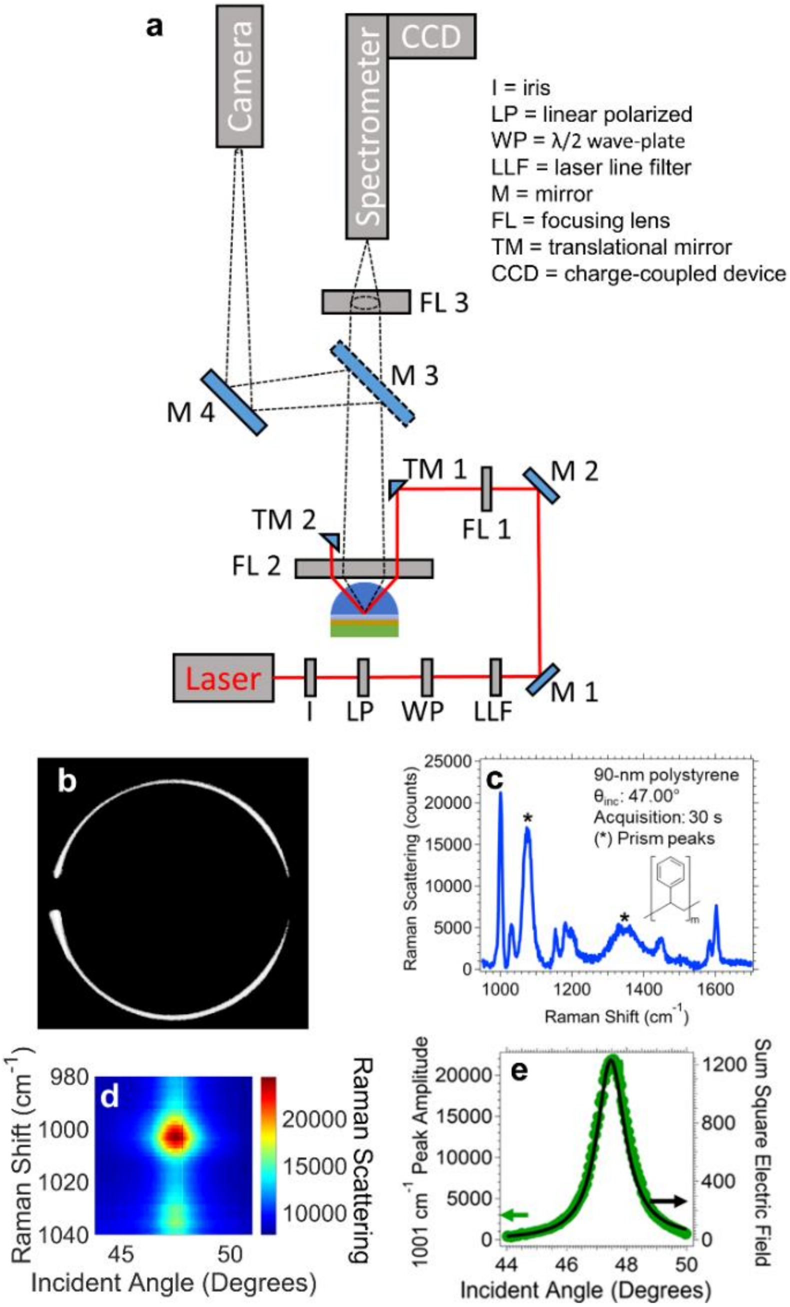

Figure 9. a Instrument schematic of the directional Raman spectroscopy instrument. **b** An image of the SPP cone and **c** the directional Raman spectrum encoded within the cone for a 90 nm

polystyrene film adsorbed on a 50 nm Au film. The SPP cone and the spectrum were acquired at the SPR angle of 47.00°. **d** Directional Raman scattering intensity as a function of Raman shift and incident angle. The color scale represents the Raman scattering intensity. **e** Peak amplitude versus incident angle of the 1001 cm^{-1} mode of polystyrene (symbol) and the calculated sum square electric field fit (solid black line) to the experimental data obtained from **d**. [Nyamekye CKA, Weibel SC, Bobbitt JM, Smith EA (2018) Combined measurement of directional Raman scattering and surface-plasmon-polariton cone from adsorbates on smooth planar gold surfaces. Analyst 143 (2):400-408. doi:10.1039/C7AN01299C] (ref. [38]) – Reproduced by permission of The Royal Society of Chemistry.

Directional Raman spectroscopy has been demonstrated by Li et al. [44] to measure a *p*-aminothiophenol monolayer adsorbed on a Ag substrate with p-polarized 532 nm excitation. They reported that the directional signal emanating through the prism at 44.5° was ~10× stronger than the Raman scattering signal on the air side. Qi and coworkers reported experimental [88,89] and calculated [90-92] directional Raman scattering from monolayers and waveguides. Neither Li nor Qi reported an experimentally measured SPP cone. The calculations provided by Qi and coworkers, however, showed that the wavelength of the excitation source, analyte, and indices of refraction of the interfacial layers (mainly the type of metal film: Au, Ag, Pt) influenced the SPP cone properties. Most recently, Yukhymchuk and coauthors developed a directional Raman spectroscopy instrument to measure Rhodamine G6 adsorbed on Ag surfaces [93]. An elliptical mirror enabled the collection of the directional signal emanating from the full SPP cone, although the cone was not imaged. The operation of the elliptical mirror enabled a wider angular range for data collection, as opposed to using a collection lens in the instrument developed by Byahut and Furtak [40]. As with previous work, they showed the information measured is akin to that measured by surface plasmon resonance.

The directional Raman signal can also be produced by waveguide samples. Similar to the waveguide studies discussed above, the plasmon waveguide samples enable both p- and s-polarized light to generate modes in the waveguide and produce enhanced electric fields oriented in the x-, y-, and z-directions. Nyamekye et al. [39] recently reported the experimental collection and modeling of the waveguide-coupled SPP cone with reverse-Kretschmann (Figure 10a) and Kretschmann (Figure 10d) illumination geometries. In the reverse-Kretschmann configuration with the light illuminating the interface from the sample side and perpendicular to the interface, all the waveguide modes are excited simultaneously [91,90]. This enables the direct comparison of all the waveguide modes in a single image (Figure 10b,c). The sensitivity (i.e., the change in the waveguide-coupled SPP cone angle per nanometer change in the polymer thickness) of all the SPP cone modes across ~400 to 700 nm polymer waveguide films is between 0.009 and 0.02° nm^{-1}. This range is similar to the plasmon waveguide resonance sensitivity value of 0.01° nm^{-1} reported by Abbas et al. [94] using an angle-scanning SPR instrument. A traditional angle scanning SPR instrument (or plasmon waveguide resonance instrument) does not provide chemical information, whereas the thickness, chemical composition, structure and orientation of thin films adsorbed onto waveguides can be obtained using the directional Raman spectroscopy instrument (Figure 10e).

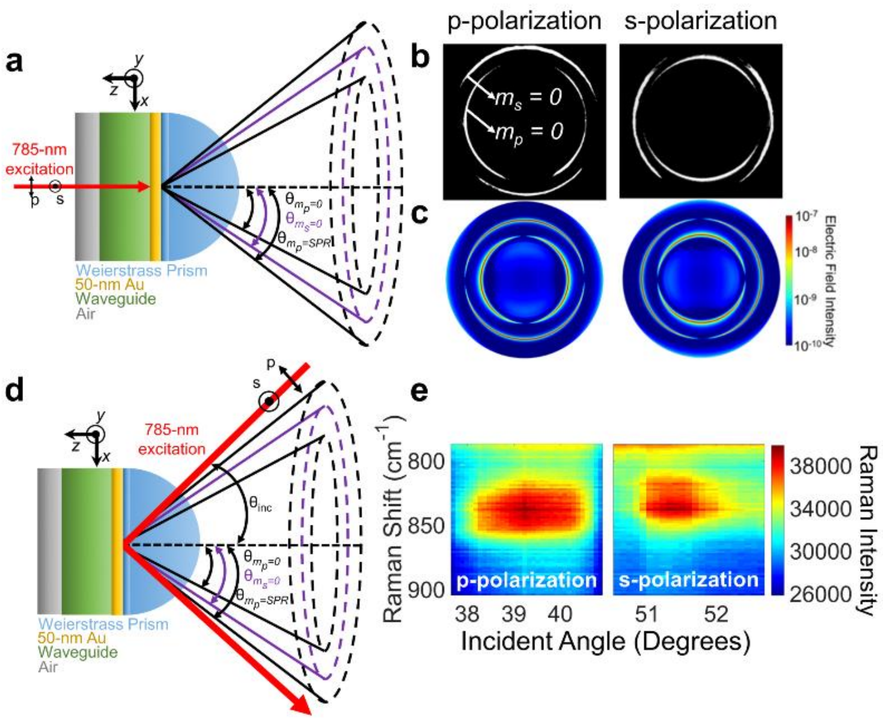

Figure 10. a Schematic of the reverse-Kretschmann configuration used to collect **b** the experimentally measured (black/white images) and **c** calculated (color images, shown in logarithmic base 10 scale) waveguide-coupled SPP cone images of 404 nm poly(4-vinylphenol) films adsorbed onto a 50 nm Au film. The experimental [calculated] cone angles for the two waveguide modes are 35.34° [35.39°] (mode 0, p-polarization, $m_p = 0$) and 44.33° [44.30°] (mode 0, s-polarization, $m_s = 0$), respectively. **d** The Kretschmann configuration used to acquire **e** the directional Raman spectra of the 404 nm poly(4-vinylphenol) film collected as a function of the Raman shift and incident angle with p- and s-polarized 785 nm excitation. The 842 cm^{-1} Raman band is assigned to the out-of-plane CH deformation mode. Reprinted from Anal. Chim. Acta, 1048, Nyamekye CKA, Zhu Q, Mahmood R, Weibel SC, Hillier AC, Smith EA, Experimental Analysis of Waveguide-coupled Surface-plasmon-polariton Cone Properties, 123-131 (ref. [39]), Copyright (2019), with permission from Elsevier.

Conclusions

From the 1970s until recently, a variety of non-destructive TIR Raman methods have been developed and improved upon for surface-sensitive measurements. TIR Raman techniques have great potential for a variety of surface and interfacial measurements, and in many cases can provide complementary information to other surface analysis techniques. The primary impediment to the adoption of the technique is the availability of commercial instruments. While most of the instruments used to collect the data discussed in this review were prism-based TIR Raman instruments, TIR Raman scattering can be excited and collected through a high numerical aperture objective lens. This is similar to most total internal reflection fluorescence (TIRF) experiments using a commercial instrument, wherein the laser is directed to the sample at an angle greater than the critical angle through the objective. Compared to using an external prism, the objective-based TIR approach generally simplifies laser alignment, and may be better suited and easily adapted to many commercial TIR Raman instruments. The prism-based approach, on the other hand, is better suited when the index of refraction of the internal reflection element needs to be changed and to achieve a larger range of incident angles. Once the utility of the technique is accepted, more specialized commercial instrumentation may be developed.

Another area of continued research is pushing the limits of the signal to measure thinner films and lower concentrations of surface species. Of course roughened metal surfaces can be used in the TIR Raman format, and these measurements are useful in many cases, but signal enhancement strategies that maintain the smooth interface will be particularly useful. Such advancements could enable in-situ TIR Raman spectroscopy studies of, for example, photovoltaic thin films, polymer brushes, sensors, and model thin film catalysts. Furthermore, TIR Raman spectroscopy can be applicable in industrial settings, such as the automotive industry. An excellent example of this was reported by Bain and co-workers, comprising the direct TIR Raman detection of thin lubricant films in a tribological contact to evaluate shear thinning in the wear of engine components [26]. Among all previously studied samples, gas-based monitoring is the least studied with TIR Raman spectroscopy. We envision an increase in the detection of gases with TIR Raman spectroscopy, particularly with new signal enhancement strategies established. Finally, while TIR Raman spectroscopy is ideally suited for three-dimensional depth profiling and imaging at the interface, much work remains to be done to fully take advantage of its capabilities. For example, future directions may be aimed at obtaining exquisite depth profiling measurements of the Raman signal to reconstruct polymer film structures as well as imaging to obtain lateral spatial resolution. The future of TIR Raman spectroscopy will break the barriers to achieve better depth profiling resolution with fast temporal resolution to measure dynamic events as they occur at a surface.

Acknowledgements

The authors acknowledge support from the National Science Foundation (NSF) under Grant Number CHE-1709099.

References

1. Greene PR, Bain CD (2004) Total internal reflection Raman spectroscopy. Spectroscopy Europe 16 (4):8-15

2. Woods DA, Bain CD (2012) Total internal reflection Raman spectroscopy. Analyst 137 (1):35-48. doi:10.1039/C1AN15722A

3. Woods DA, Bain CD (2014) Total internal reflection spectroscopy for studying soft matter. Soft Matter 10 (8):1071-1096. doi:10.1039/C3SM52817K

4. Fleischmann M, Hendra PJ, McQuillan AJ (1974) Raman spectra of pyridine adsorbed at a silver electrode. Chem. Phys. Lett. 26 (2):163-166. doi:http://dx.doi.org/10.1016/0009-2614(74)85388-1

5. Allen CS, Schatz GC, Van Duyne RP (1980) Tunable laser excitation profile of surface enhanced Raman scattering from pyridine adsorbed on a copper electrode surface. Chem. Phys. Lett. 75 (2):201-205. doi:https://doi.org/10.1016/0009-2614(80)80496-9

6. Allen CS, Van Duyne RP (1981) Molecular generality of surface-enhanced Raman spectroscopy (SERS). A detailed investigation of the hexacyanoruthenate ion adsorbed on silver and copper electrodes. J. Am. Chem. Soc. 103 (25):7497-7501. doi:10.1021/ja00415a017

7. Jeanmaire DL, Van Duyne RP (1977) Surface Raman spectroelectrochemistry: Part I. Heterocyclic, aromatic, and aliphatic amines adsorbed on the anodized silver electrode. J. Electroanal. Chem. Interf. Electrochem. 84 (1):1-20. doi:https://doi.org/10.1016/S0022-0728(77)80224-6

8. Langer J, Jimenez de Aberasturi D, Aizpurua J, Alvarez-Puebla RA, Auguié B, Baumberg JJ, et al. (2020) Present and future of surface-enhanced Raman scattering. ACS Nano 14 (1):28-117. doi:10.1021/acsnano.9b04224

9. Fan M, Andrade GFS, Brolo AG (2011) A review on the fabrication of substrates for surface enhanced Raman spectroscopy and their applications in Anal. Chem.. Anal. Chim. Acta 693 (1):7-25. doi:https://doi.org/10.1016/j.aca.2011.03.002

10. White MS, Kaltenbrunner M, Głowacki ED, Gutnichenko K, Kettlgruber G, Graz I, Aazou S, Ulbricht C, Egbe DAM, Miron MC, Major Z, Scharber MC, Sekitani T, Someya T, Bauer S, Sariciftci NS (2013) Ultrathin, highly flexible and stretchable PLEDs. Nat. Photonics 7:811. doi:10.1038/nphoton.2013.188

11. Fahrenfort J (1961) Attenuated total reflection: A new principle for the production of useful infra-red reflection spectra of organic compounds. Spectrochim. Acta 17 (7):698-709. doi:https://doi.org/10.1016/0371-1951(61)80136-7

12. Fahrenfort J (1968) Developments and applications in attenuated total reflectance. Mol. Spectrosc. Proc. Conf. 4th:111

13. Harrick NJ (1960) Surface chemistry from spectral analysis of totally internally reflected radiation*. J. Phys. Chem. 64 (9):1110-1114. doi:10.1021/j100838a005

14. Hansen WN (1968) Electric fields produced by the propagation of plane coherent electromagnetic radiation in a stratified medium. J. Opt. Soc. Am. 58 (3):380-390. doi:10.1364/JOSA.58.000380

15. Karl R (1966) Application of the attenuated total reflection (ATR) method to the infrared spectroscopic analysis of multi-layer paint films. Farbe und Lack 72 (1):13

16. Shigeyuki T (1968) Infrared analysis. Kobunshi 17 (200):1017

17. Fujiyama T, Crawford B (1968) Vibrational intensities. XXI. Some band shapes and intensities in liquid hexafluorobenzene. J. Phys. Chem. 72 (6):2174-2181. doi:10.1021/j100852a050

18. Wilks PA (1969) Internal reflectance spectroscopy II: Quantitative analysis aspects. Appl. Spectrosc. 23 (1):63-66. doi:10.1366/000370269774381201

19. Hirschfeld T (1967) Procedures for attenuated total reflection study of extremely small samples. Appl. Opt. 6 (4):715-718. doi:10.1364/AO.6.000715

20. Wilks PA, Hirschfeld T (1967) Internal reflection spectroscopy. Appl. Spectrosc. Rev. 1 (1):99-130. doi:10.1080/05704926708547582

21. Beattie DA, Larsson ML, Holmgren AR (2006) In situ total internal reflection Raman spectroscopy of surfactant adsorption at a mineral surface. Vib. Spectrosc. 41 (2):198-204. doi:http://dx.doi.org/10.1016/j.vibspec.2006.02.003

22. Woods DA, Petkov J, Bain CD (2011) Surfactant adsorption by total internal reflection Raman spectroscopy. Part III: Adsorption onto cellulose. Colloid Surf. A Physicochem. Eng. Asp. 391 (1):10-18. doi:https://doi.org/10.1016/j.colsurfa.2011.07.027

23. Grenoble Z, Baldelli S (2013) Adsorption of benzyldimethylhexadecylammonium chloride at the hydrophobic silica–water interface studied by total internal reflection Raman spectroscopy: Effects of Silica Surface Properties and Metal Salt Addition. J. Phys. Chem. B 117 (34):9882-9894. doi:10.1021/jp4015096

24. Liljeblad JFD, Furó I, Tyrode EC (2017) The premolten layer of ice next to a hydrophilic solid surface: correlating adhesion with molecular properties. Phys. Chem. Chem. Phys. 19 (1):305-317. doi:10.1039/C6CP05303C

25. Lee C, Wacklin H, Bain CD (2009) Changes in molecular composition and packing during lipid membrane reconstitution from phospholipid–surfactant micelles. Soft Matter 5 (3):568-575. doi:10.1039/B812768A

26. Praveena M, Guha K, Ravishankar A, Biswas SK, Bain CD, Jayaram V (2014) Total internal reflection Raman spectroscopy of poly(alpha-olefin) oils in a lubricated contact. RSC Adv. 4 (42):22205-22213. doi:10.1039/C4RA02261K

27. Ngo D, Baldelli S (2016) Adsorption of dimethyldodecylamine oxide and its mixtures with Triton X-100 at the hydrophilic silica/water interface studied using total internal reflection Raman spectroscopy. J. Phys. Chem. B 120 (48):12346-12357. doi:10.1021/acs.jpcb.6b08853

28. Takenaka T, Nogami K, Gotoh H, Gotoh R (1971) Studies on built-up films by means of the polarized infrared ATR spectrum I.: Built-up films of stearic acid. J. Colloid Interface Sci. 35 (3):395-402. doi:https://doi.org/10.1016/0021-9797(71)90138-X

29. Nakanaga T, Takenaka T (1977) Resonance Raman spectra of monolayers of a surface-active dye adsorbed at the oil-water interface. J. Phys. Chem. 81 (7):645-649. doi:10.1021/j100522a011

30. Takenaka T (1979) Application of Raman spectroscopy to the study of surface chemistry. Adv. Colloid Interface Sci. 11 (4):291-313. doi:https://doi.org/10.1016/0001-8686(79)80011-1

31. Giesekke EW (1983) A review of spectroscopic techniques applied to the study of interactions between minerals and reagents in flotation systems. Int. J. Miner. Process. 11 (1):19-56. doi:https://doi.org/10.1016/0301-7516(83)90043-1

32. Hölzer W, Schröter O, Richter A (1990) Raman study on surface layers and thin films by using total reflection experiments. J. Mol. Struct. 217:253-264. doi:https://doi.org/10.1016/0022-2860(90)80366-R

33. Yoshikawa M, Gotoh T, Mori Y, Iwamoto M, Ishida H (1994) Determination of anisotropic refractive indices of a single-crystal organic thin film by attenuated total reflection Raman spectroscopy. Appl. Phys. Lett. 64 (16):2096-2098. doi:10.1063/1.111694

34. Fontaine NH, Furtak TE (1997) Precise control of evanescent fields from a Gaussian beam for depth-resolved spectroscopy. J. Opt. Soc. Am. B 14 (12):3342-3348. doi:10.1364/JOSAB.14.003342

35. Fontaine NH, Furtak TE (1998) Variable-angle internal-reflection Raman spectroscopy for depth-resolved vibrational characterization of polymer thin films. Phys. Rev. B 57 (7):3807-3810. doi:10.1103/PhysRevB.57.3807

36. Ota C (2015) Investigation of the structure of water at hydrophobic and hydrophilic interfaces by angle-resolved TIR Raman spectroscopy. Phys. Chem. Chem. Phys. 17 (39):26435-26442. doi:10.1039/C5CP03581C

37. McKee KJ, Meyer MW, Smith EA (2012) Near IR scanning angle total internal reflection Raman spectroscopy at smooth gold films. Anal. Chem. 84 (10):4300-4306. doi:10.1021/ac203355a

38. Nyamekye CKA, Weibel SC, Bobbitt JM, Smith EA (2018) Combined measurement of directional Raman scattering and surface-plasmon-polariton cone from adsorbates on smooth planar gold surfaces. Analyst 143 (2):400-408. doi:10.1039/C7AN01299C

39. Nyamekye CKA, Zhu Q, Mahmood R, Weibel SC, Hillier AC, Smith EA (2019) Experimental analysis of waveguide-coupled surface-plasmon-polariton cone properties. Anal. Chim. Acta 1048:123-131. doi:https://doi.org/10.1016/j.aca.2018.09.057

40. Byahut SP, Furtak TE (1991) Surface plasmon assisted Raman scattering from electrochemically controlled adsorbates on flat, single crystal silver. Electrochim. Acta 36 (11):1879-1882. doi:https://doi.org/10.1016/0013-4686(91)85061-B

41. Futamata M (1995) Surface plasmon polariton enhanced Raman scattering from adsorbates on a "smooth" metal surface: The effect of thickness and dielectric properties of constituents. Langmuir 11 (10):3894-3901. doi:10.1021/la00010a046

42. Meyer SA, Auguié B, Le Ru EC, Etchegoin PG (2012) Combined SPR and SERS microscopy in the Kretschmann configuration. J. Phys. Chem. A 116 (3):1000-1007. doi:10.1021/jp2107507

43. Jiang S-L, Chen L, Yu X-X, Zheng H-J, Lin K, Zhang Q, Wang X-P, Luo Y (2017) Surface plasmon assisted directional Rayleigh scattering. Chin. J. Chem. Phys. 30 (2):135-138. doi:10.1063/1674-0068/30/cjcp1611204

44. Li H, Xu S, Liu Y, Gu Y, Xu W (2012) Directional emission of surface-enhanced Raman scattering based on a planar-film plasmonic antenna. Thin Solid Films 520 (18):6001-6006. doi:http://dx.doi.org/10.1016/j.tsf.2012.04.084

45. Pettinger B, Tadjeddine A, Kolb DM (1979) Enhancement in Raman intensity by use of surface plasmons. Chem. Phys. Lett. 66 (3):544-548. doi:https://doi.org/10.1016/0009-2614(79)80335-8

46. Wang H, Li H, Xu S, Zhao B, Xu W (2017) Integrated plasmon-enhanced Raman scattering (iPERS) spectroscopy. Sci. Rep. 7 (1):14630. doi:10.1038/s41598-017-15111-3

47. Huo S-X, Liu Q, Cao S-H, Cai W-P, Meng L-Y, Xie K-X, Zhai Y-Y, Zong C, Yang Z-L, Ren B, Li Y-Q (2015) Surface plasmon-coupled directional enhanced Raman scattering by means of the reverse Kretschmann configuration. J. Phys. Chem. Lett. 6 (11):2015-2019. doi:10.1021/acs.jpclett.5b00666

48. D’Hooge L, Vigoureux JM, Menu C (1981) General theory of the Raman scattering close to a plane surface. Evanescent Raman spectra. J. Chem. Phys. 74 (7):3639-3659. doi:10.1063/1.441591

49. D'Hooge L, Vigoureux JM (1979) Evanescent field excitation of homogeneous raman scattering close to a dielectric. Chem. Phys. Lett. 65 (3):500-506. doi:https://doi.org/10.1016/0009-2614(79)80280-8

50. Ikeshoji T, Ono Y, Mizuno T (1973) Total reflection Raman spectra; Raman scattering due to the evanescent wave in total reflection. Appl. Opt. 12 (10):2236-2237. doi:10.1364/AO.12.002236

51. Nickolov ZS, Earnshaw JC, McGarvey JJ (1993) Water structure at interfaces studied by total internal reflection Raman spectroscopy. Colloid Surf. A Physicochem. Eng. Asp. 76:41-49. doi:https://doi.org/10.1016/0927-7757(93)80059-N

52. McKee KJ, Smith EA (2010) Development of a scanning angle total internal reflection Raman spectrometer. Rev. Sci. Instrum. 81 (4):043106. doi:10.1063/1.3378682

53. Fujiwara K, Watarai H (2003) Total internal reflection resonance Raman microspectroscopy for the liquid/liquid interface. Ion-association adsorption of cationic Mn(III) porphine. Langmuir 19 (7):2658-2664. doi:10.1021/la026119y

54. Jubb AM, Verreault D, Posner R, Criscenti LJ, Katz LE, Allen HC (2013) Sulfate adsorption at the buried hematite/solution interface investigated using total internal reflection (TIR)-Raman spectroscopy. J. Colloid Interface Sci. 400:140-146. doi:10.1016/j.jcis.2013.02.031

55. Damin CA, Nguyen VHT, Niyibizi AS, Smith EA (2015) Application of scanning angle Raman spectroscopy for determining the location of buried polymer interfaces with tens of nanometer precision. Analyst 140 (6):1955-1964. doi:10.1039/C4AN02240H

56. Lesoine MD, Bobbitt JM, Zhu S, Fang N, Smith EA (2014) High angular-resolution automated visible-wavelength scanning angle Raman microscopy. Anal. Chim. Acta 848:61-66. doi:http://dx.doi.org/10.1016/j.aca.2014.07.040

57. Lesoine MD, Bobbitt JM, Carr JA, Elshobaki M, Chaudhary S, Smith EA (2014) Quantitative comparison of organic photovoltaic bulk heterojunction photostability under laser illumination. J. Phys. Chem. C 118 (51):30229-30237. doi:10.1021/jp509589g

58. Rabolt JF, Santo R, Swalen JD (1979) Raman spectroscopy of thin polymer films using integrated optical techniques. Appl. Spectrosc. 33 (6):549-551. doi:10.1366/0003702794925101

59. Rabolt JF, Schlotter NE, Swalen JD (1981) Spectroscopic studies of thin film polymer laminates using Raman spectroscopy and integrated optics. J. Phys. Chem. 85 (26):4141-4144. doi:10.1021/j150626a038

60. Schlotter NE, Rabolt JF (1984) Raman spectroscopy in polymeric thin film optical waveguides. 1. Polarized measurements and orientational effects in two-dimensional films. J. Phys. Chem. 88 (10):2062-2067. doi:10.1021/j150654a025

61. Zimba CG, Rabolt JF (1991) Parametric optimization of waveguide Raman spectroscopy in the near-IR. Thin Solid Films 206 (1):388-393. doi:https://doi.org/10.1016/0040-6090(91)90456-8

62. Zimba CG, Turrell S, Swalen JD, Hallmark VM, Rabolt JF (1990) Applications of Fourier transform Raman spectroscopy to studies of thin polymer films. J. Phys. Chem. 94 (2):939-943. doi:10.1021/j100365a080

63. Swalen JD, Schlotter NE, Santo R, Rabolt JF (1981) Raman spectroscopy of laminated polymer films by integrated optical techniques. J. Adhes. 13 (2):189-194. doi:10.1080/00218468108073185

64. Schlotter NE (1990) Diffusion of small molecules in glassy polymer thin films studied by waveguide Raman techniques. J. Phys. Chem. 94 (4):1692-1699. doi:10.1021/j100367a086

65. Carius W, Schröter O (1980) Total reflection Raman spectroscopy (TRRS) of polystyrene. Phys. Status Solidi A 59 (1):K115-K118. doi:10.1002/pssa.2210590178

66. Iwamoto R, Miya M, Ohta K, Mima S (1980) Total internal reflection Raman spectroscopy as a new tool for surface analysis. J. Am. Chem. Soc. 102 (3):1212-1213. doi:10.1021/ja00523a074

67. Iwamoto R, Miya M, Ohta K, Mima S (1981) Total internal reflection Raman spectroscopy. J. Chem. Phys. 74 (9):4780-4790. doi:10.1063/1.441757

68. Iwamoto R, Ohta K, Miya M, Mima S (1981) Total internal reflection Raman spectroscopy at the critical angle for Raman measurements of thin films. Appl. Spectrosc. 35 (6):584-587. https://doi.org/10.1366/0003702814732102

69. Meyer MW, Larson KL, Mahadevapuram RC, Lesoine MD, Carr JA, Chaudhary S, Smith EA (2013) Scanning angle Raman spectroscopy of poly(3-hexylthiophene)-based films on indium tin oxide, gold, and sapphire surfaces. ACS Appl. Mater. Interfaces 5 (17):8686-8693. doi:10.1021/am4023225

70. Bobbitt JM, Smith EA (2018) Extracting interface locations in multilayer polymer waveguide films using scanning angle Raman spectroscopy. J. Raman Spectrosc. 49 (2):262-270. doi:10.1002/jrs.5275

71. Bobbitt JM, Mendivelso-Pérez D, Smith EA (2016) Scanning angle Raman spectroscopy: A nondestructive method for simultaneously determining mixed polymer fractional composition and film thickness. Polymer 107:82-88. doi:http://dx.doi.org/10.1016/j.polymer.2016.10.063

72. Chen YJ, Chen WP, Burstein E (1976) Surface-electromagnetic-wave-enhanced Raman scattering by overlayers on metals. Phys. Rev. Lett. 36 (20):1207-1210. https://doi.org/10.1103/PhysRevLett.36.1207

73. Giergiel J, Reed CE, Hemminger JC, Ushioda S (1988) Surface plasmon polariton enhancement of Raman scattering in a Kretschmann geometry. J. Phys. Chem. 92 (19):5357-5365. doi:10.1021/j100330a009

74. Meyer SA, Le Ru EC, Etchegoin PG (2011) Combining surface plasmon resonance (SPR) spectroscopy with surface-enhanced Raman scattering (SERS). Anal. Chem. 83 (6):2337-2344. doi:10.1021/ac103273r

75. Fu C, Hu C, Liu Y, Xu S, Xu W (2012) Bioidentification of biotin/avidin using surface plasmon resonance and surface-enhanced Raman scattering (SPR-SERS) spectroscopy. Anal. Methods 4 (10):3107-3110. doi:10.1039/C2AY25697E

76. McKee KJ, Meyer MW, Smith EA (2012) Plasmon waveguide resonance Raman spectroscopy. Anal. Chem. 84 (21):9049-9055. doi:10.1021/ac3013972

77. Meyer MW, McKee KJ, Nguyen VHT, Smith EA (2012) Scanning angle plasmon waveguide resonance Raman spectroscopy for the analysis of thin polystyrene films. J. Phys. Chem. C 116 (47):24987-24992. doi:10.1021/jp308882w

78. Bobbitt JM, Weibel SC, Elshobaki M, Chaudhary S, Smith EA (2014) Fourier transform-plasmon waveguide spectroscopy: A nondestructive multifrequency method for simultaneously determining polymer thickness and apparent index of refraction. Anal. Chem. 86 (24):11957-11961. doi:10.1021/ac504103g

79. Simon HJ, Guha JK (1976) Directional surface plasmon scattering from silver films. Opt. Commun. 18 (3):391-394. doi:http://dx.doi.org/10.1016/0030-4018(76)90158-9

80. Braundmeier AJ, Tomaschke HE (1975) Observation of the simultaneous emission of roughness-coupled and optical-coupled surface plasmon radiation from silver. Opt. Commun. 14 (1):99-103. doi:http://dx.doi.org/10.1016/0030-4018(75)90067-X

81. Wittke W, Hatta A, Otto A (1989) Efficient use of the surface plasmon polariton resonance in light scattering from adsorbates. Appl. Phys. A 48 (3):289-294. doi:10.1007/bf00619400

82. Byahut S, Furtak TE (1990) A device for performing surface-plasmon-polariton-assisted Raman scattering from adsorbates on single-crystal silver surfaces. Rev. Sci. Instrum. 61 (1):27-32. doi:10.1063/1.1141321

83. Byahut S, Furtak TE (1991) Direct comparison of the chemical properties of single crystal Ag(111) and electrochemically roughened Ag as substrates for surface Raman scattering. Langmuir 7 (3):508-513. doi:10.1021/la00051a016

84. Futamata M (1995) Surface-plasmon-polariton-enhanced Raman scattering from self-assembled monolayers of p-nitrothiophenol and p-aminothiophenol on silver. J. Phys. Chem. 99 (31):11901-11908. doi:10.1021/j100031a018

85. Futamata M (1997) Application of attenuated total reflection surface-plasmon-polariton Raman spectroscopy to gold and copper. Appl. Opt. 36 (1):364-375. doi:10.1364/AO.36.000364

86. Futamata M, Borthen P, Thomassen J, Schumacher D, Otto A (1994) Application of an ATR method in Raman spectroscopy. Appl. Spectrosc. 48 (2):252-260. https://doi.org/10.1366/0003702944028524

87. Futamata M, Keim E, Bruckbauer A, Schumacher D, Otto A (1996) Enhanced Raman scattering from copper phthalocyanine on Pt by use of a Weierstrass prism. Appl. Surf. Sci. 100:60-63. doi:http://dx.doi.org/10.1016/0169-4332(96)00257-7

88. Wan X-M, Chen C, Fan Z-B, Lu D-F, Gao R, Qi Z-M (2016) Raman spectroscopy based on plasmon waveguide prepared with mesoporous TiO_2 thin film. Acta Phys. Sin. 65:137801. doi:10.7498/aps.65.137801

89. Wan X-M, Gao R, Lu D-F, Qi Z-M (2018) Self-referenced directional enhanced Raman scattering using plasmon waveguide resonance for surface and bulk sensing. Appl. Phys. Lett. 112 (4):041906. doi:10.1063/1.5009491

90. Chen C, Lu D-F, Gao R, Qi Z-M (2016) Analysis of waveguide-coupled directional emission for efficient collection of fluorescence/Raman light from surface. Opt. Commun. 367:86-94. doi:http://dx.doi.org/10.1016/j.optcom.2016.01.001

91. Chen C, Li J-Y, Wang L, Lu D-F, Qi Z-M (2015) Waveguide-coupled directional Raman radiation for surface analysis. Phys. Chem. Chem. Phys. 17 (33):21278-21287. doi:10.1039/C4CP05092D

92. Chen C, Lu D-F, Gao R, Cheng J, Qi Z-M (2016) Surface Raman spectroscopy with and without reverse Kretschmann configuration: Effect of evanescent-wave-coupled emission. Appl. Phys. Express 9 (6):062001. https://doi.org/10.7567/APEX.9.062001

93. Beketov GV, Shynkarenko OV, Yukhymchuk VO (2019) Optical arrangement for surface plasmon-assisted directional enhanced Raman scattering spectroscopy. Spectrochim. Acta Part A: Molecular and Biomolecular Spectroscopy 219:488-495. doi:https://doi.org/10.1016/j.saa.2019.04.039

94. Abbas A, Linman MJ, Cheng Q (2011) Sensitivity comparison of surface plasmon resonance and plasmon-waveguide resonance biosensors. Sens. Actuators, B 156 (1):169-175. doi:https://doi.org/10.1016/j.snb.2011.04.008

CHAPTER 3. COMBINED MEASUREMENT OF DIRECTIONAL RAMAN SCATTERING AND SURFACE-PLASMON-POLARITON CONE FROM ADSORBATES ON SMOOTH PLANAR GOLD SURFACES

Charles K. A. Nyamekye[a,b], Stephen C. Weibel[c], Jonathan M. Bobbitt[a,b], and Emily A. Smith*[a,b]

[a] The Ames Laboratory, U.S. Department of Energy, Ames, Iowa 50011, United States

[b] Department of Chemistry, Iowa State University, Ames, Iowa 50011, United States

[c] Surface Photonics Inc., Madison, Wisconsin 53719, United States

* Corresponding Author (esmith1@iastate.edu, 1-515-294-1424)

Modified from a manuscript published in Analyst

Abstract

Directional-surface-plasmon-coupled Raman scattering (directional RS) has the combined benefits of surface plasmon resonance and Raman spectroscopy, and provides the ability to measure adsorption and monolayer-sensitive chemical information. Directional RS is performed by optically coupling a 50-nm gold film to a Weierstrass prism in the Kretschmann configuration and scanning the angle of the incident laser under total internal reflection. The collected parameters on the prism side of the interface include a full surface-plasmon-polariton cone and the full Raman signal radiating from the cone as a function of incident angle. An instrument for performing directional RS and a quantitative study of the instrumental parameters are herein reported. To test the sensitivity and quantify the instrument parameters, self-assembled monolayers and 10 to 100-nm polymer films are studied. The signals are found to be well-modeled by two calculated angle-dependent parameters: three-dimensional finite-difference time-domain calculations of the electric field generated in the sample layer and projected to the far-field, and Fresnel calculations of the reflected light intensity. This is the first report of the

quantitative study of the full surface-plasmon-polariton cone intensity, cone diameter, and directional Raman signal as a function of incident angle. We propose that directional RS is a viable alternative to surface plasmon resonance when added chemical information is beneficial.

Introduction

For several decades, surface plasmon resonance (SPR) has been studied extensively for a range of applications, such as detecting and monitoring the kinetics, affinity, and selectivity of interactions between an adsorbate and an immobilized binding partner.[1-7] A drawback to SPR is the encoded signal provides minimal, at best, information about what is adsorbed at the surface; what information is provided is typically through a series of control experiments to measure nonspecific binding.[8] Under total internal reflection, surface plasmons can be generated when the excitation light is at an appropriate incident angle upon a high refractive index prism traveling to an interface with a thin noble metal film and an adjacent dielectric material with a lower refractive index. An exponentially decaying evanescent wave is generated in the dielectric material that extends from ~100 nm to ~2 nm, depending on the excitation wavelength and the indices of refraction of the interfacial media.[9-12] In contrast, on the prism side, excitation of surface plasmons in the plane of the metal film (in-coupling) and scattered light through the prism (out-coupling) results in a hollow cone of directional emission at a sharply defined angle.[13-18] This is referred to as the surface-plasmon-polariton cone (or more simply "cone"). An illustration of the cone generated using a Weierstrass prism in the Kretschmann geometry is shown in Figure 1. Braundmeier et al.[19] proposed two mechanisms for the generation of the cone they measured using a 40-nm silver film: (1) momentum conserving optical coupling and (2) scattering from surface irregularities (e.g., grain boundaries and dislocations) or roughness coupling. The angle of incidence (θ_{inc}) that results in the emission cone is given by equation 1, where η is the refractive index of the prism and ϵ is the dielectric function of the metal film.[19]

$$\theta_{inc} = arcsin\left[\eta^{-1}\left(\frac{\epsilon}{1+\epsilon}\right)^{\frac{1}{2}}\right] \tag{1}$$

Fluorophores in close proximity to a gold or silver surface can be excited within the cone and this is referred to as surface plasmon coupled emission.[20-24] Gryczynski et al.[25, 26] reported the surface plasmon coupled emission from 30 to 750-nm polyvinyl alcohol films with incorporated fluorescent sulforhodamine 101 on a 50-nm silver substrate. They photographed the surface plasmon coupled emission cone projected onto tracing paper, and concluded that there was an increase in the angle where the maximum luminescence was measured with increasing polyvinyl alcohol thickness. Also, four surface plasmon coupled emission cones were observed for a 745-nm film, but quantification of the cone parameters was not reported. Quenching and photobleaching of the fluorophores is a concern with luminescence,[27] and more importantly, chemical identification of the adsorbates is limited using luminescence.

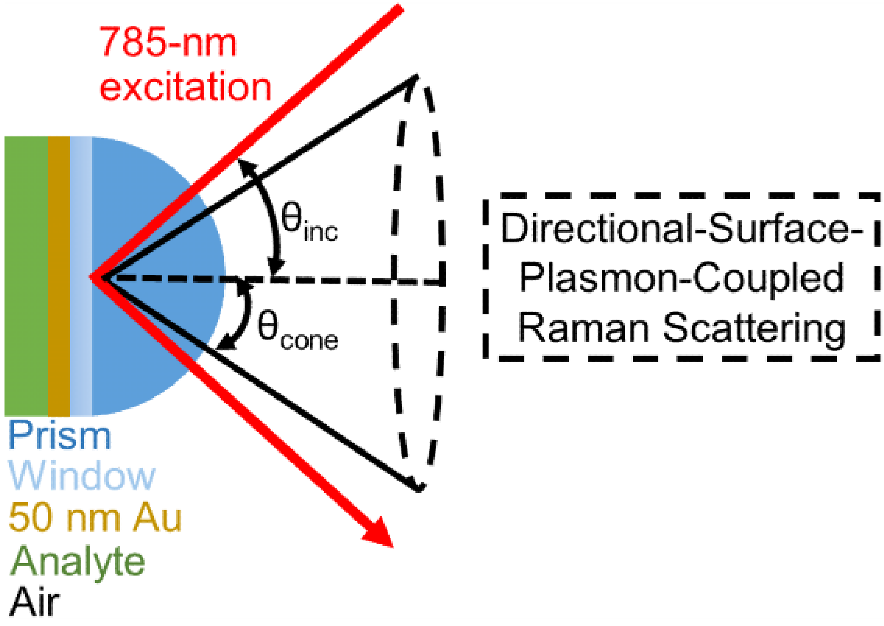

Figure 1. Schematic illustrating the Weierstrass prism (formed by optically coupling a sapphire hemispherical prism to a sapphire window) in the Kretschmann configuration with a 50-nm thick gold substrate. The signals are collected on the *prism side* (i.e., with collection optics on the right side of this schematic). The data include an image of the full cone to extract the intensity and

diameter as well as Raman scattering as a function of incident angle. The signal on the *sample side* refers to placing the collection optics on the left side of this schematic. The schematic is not drawn to scale.

Directional-surface-plasmon-coupled Raman scattering (directional RS) generated within the cone has also been demonstrated, with some of the earliest reports from Furtak,[28] Otto,[18] and Futamata.[29] In 1990, Byahut and Furtak[28] used a device that allowed the collection of the Raman signal from the entire cone. In their set-up, a hemispherical prism and a paraboloid mirror in the Kretschmann configuration was used to obtain a Raman spectrum of a paranitrosodimethylaniline monolayer on a silver film. A Weierstrass prism is capable of collecting the entire cone in the Kretschmann and Otto configurations.[18, 30, 31] Futamata et al.[29, 30, 32] projected the entire cone onto paper from an attenuated total reflection device in the Otto configuration (Weierstrass prism/air gap/adsorbate/silver). By controlling the thickness of the air gap and/or placing water in the air gap, the Raman band intensities were increased for monolayers of copper-phthalocyanine, p-nitrothiophenol and p-aminothiophenol with 514.5-nm excitation. However, in all these fundamental studies, the cone was projected onto paper in a manner that did not facilitate the quantification of the cone parameters, or was not recorded at all, thus the ability to extract optical information about the adsorbed analytes was not demonstrated.

Li et al.[33] collected the Raman spectrum of p-aminothiophenol on a silver substrate coupled to a semi-cylindrical prism on an angle-resolved Raman spectrometer with 532-nm excitation. Etchegoin et al.[34, 35] were able to simultaneously measure the SPR reflectivity and Raman signal of a monolayer of Nile Blue on 50-nm silver and gold films as a function of the incident angle. While Li et al. and Etchegoin et al. collected the Raman signal as a function of incident angle, they did not study the surface-plasmon-polariton cone nor collect the Raman signal from the entire cone (thus the signal collection was not optimized).

When an appropriately roughened metal film replaces the smooth noble metal film, surface enhanced Raman spectroscopy (SERS) can be combined with directional RS. Huo et al.[36] demonstrated directional RS with SERS in the reverse Kretschmann configuration (illumination from the sample side). They measured 4-aminothiophenol adsorbed on a silver nanoparticle-on-film SERS substrate, although they did not show an image of the cone nor collect the SERS signal from the entire cone. SERS substrates enhance the Raman signal, but SERS generally precludes the measurement of smooth films, and the signal is not simply modelled by calculated parameters.

While neither the surface-plasmon-polariton cone nor Raman scattering generated from the cone are new concepts, only a handful of reports[28-32] have shown the optimized collection of the entire Raman signal from the cone with the ability to scan over a limited range of the incident angles, but the ability to quantify the properties of the cone as a function of adsorption and incident angle have not been previously reported. Herein we show for the first time: (1) an instrument capable of collecting the full cone and the full Raman scattering signal emanating from the cone as functions of incident angle, which could be a useful alternative to SPR. In order to fulfill this potential, we show: (2) that the Raman signal has monolayer sensitivity on a smooth film, (3) the first quantification of the cone intensity and diameter as a function of incident angle for varying adsorbate layers, and we demonstrate (4) that it is possible to model all the instrument parameters through simple calculations to extract sample information from these properties.

The directional RS signal using a smooth planar gold film is enhanced relative to measuring the same number of molecules in solution by Raman spectroscopy. This is the result of the enhanced electric field that is produced at the interface under total internal reflection.[9] In addition, the presented instrumentation enables the full Raman signal from the cone to be collected, further increasing the signal compared to studies where only a portion of the directional Raman signal was collected. The larger signal enables the measurement of monolayers without the use of a SERS substrate, so smooth films can be measured and it is straight forward to model the signals with finite-difference time-domain and Fresnel calculations.

Furthermore, the multidimensionality of the data (cone diameter and intensity and Raman scattering as a function of incident angle) provides the ability to measure more sample properties compared to either SPR or Raman scattering techniques alone. This is highlighted by our related previous work using a technique called scanning angle Raman spectroscopy,[37-45] whereby the incident light is scanned over a wide range of angles while simultaneously collecting the reflected light from the prism side and Raman scattering on the sample side of the interface. Scanning angle Raman spectroscopy (in the absence of a gold film) was used to identify buried interfaces in a multi-layered system with ~10s of nanometer spatial resolution. This new directional RS instrument and methodology reported herein can be applied to study numerous smooth thin films including sensors, organic solar cells, and more generally as an alternative to surface plasmon resonance spectroscopy when added chemical information is beneficial.

Materials and Methods

Materials

Thiophenol (assay 99%, CAS# 108-98-5), poly(bisphenol A carbonate) (M_w = 64,000, CAS# 25037-45-0), polystyrene pellets (M_W = 192,000, CAS# 9003-53-6), 200 proof ethanol (assay 99.5%, CAS# 64-17-5), and sulfuric acid (assay 99.999%, CAS# 7664-93-9) were purchased from Sigma-Aldrich (St. Louis, MO) and used as received. Methylene chloride (assay 99.9%, CAS# 75-09-2), anhydrous toluene (assay 99.8%, CAS# 108-88-3), and hydrogen peroxide (assay 31.7%, CAS# 7722-84-1) were purchased from Fisher Chemical (Pittsburgh, PA). Deionized water from an 18.2 MΩ cm^{-1} EasyPure II filtration system (Thermo Scientific, Waltham, MA) was used as a rinsing solution.

Sample Fabrication

The sample configuration consisted of a sapphire Weierstrass prism (Figure 1, ISP Optics Irvington, NY) optically coupled to a 25.4 mm diameter sapphire substrate (Meller Optics, Providence, RI) containing a 2-nm titanium (99.999% pure Ti) adhesive layer and a 50-nm gold (99.999% pure Au) layer (metal deposition by Platypus Technologies LLC., Madison, WI). The optical coupling of the prism to the sapphire substrate used a $\eta_D = 1.7400$ index matching fluid (Cargille Laboratories Inc., Cedar Grove, NJ) to ensure optical contact without the presence of air gaps. Before preparing the thin films, the gold substrate was cleaned with piranha solution (3:1 mixture of sulfuric acid and hydrogen peroxide) for 5 minutes inside a fume hood (NOTE: piranha solution may result in chemical and thermal burns if not handled with extreme caution). The gold substrate was rinsed with deionized water, then immersed in a 50:50 (v/v) ethanol and deionized water bath for sonication using an ultrasonic cleaner for 10 minutes. Then the cleaned gold substrate was dried with a stream of N_2 gas. To form a self-assembled monolayer of thiophenol, the clean gold substrate was immersed in an ethanoic 10 mM thiophenol solution for 24 hours. The monolayer sample was rinsed with ethanol and dried with a stream of N_2 gas. For the polymer samples, solutions of poly(bisphenol A carbonate) in methylene chloride and solutions of polystyrene in toluene were prepared with concentrations ranging from 0.001 to 1.0 g mL^{-1}. To make the polymer films, 200 μL of solution was spin-coated on the gold substrate at 3000 rpm for one minute using a KW-4A spin coater (Chemat Technology, Inc. Northbridge, CA). The polymer film was allowed to dry in ambient conditions overnight. The thickness of poly(bisphenol A carbonate) and polystyrene was measured with an AlphaStep® D-600 stylus profiler (KLA-Tencor Corp. Milpitas, California). A calibration curve of thickness versus solution concentration was generated and used to fabricate polymer films approximately 10 and 50 nm thick poly(bisphenol A carbonate) and 30, 60, 70, 80, 90, and 100 nm thick polystyrene. The exact thickness of each film was subsequently measured with profilometry (Figure S1) after the surface-plasmon-polariton cone and Raman data were collected. For simplicity, the samples will be referred to by their approximate thickness throughout the text.

Directional-surface-plasmon-coupled Raman Spectrometer

A schematic of the instrument is shown in Figure 2. A sample holder was designed to secure the prism and the gold substrate onto the instrument. A 785-nm near-infrared diode laser (Toptica Photonics XTRA II, Victor, NY) with a power of 200 mW measured after FL1 was directed at the prism. A linear polarizer and half-wave plate were used to ensure p-polarized light was incident upon the interface, and a laser line filter was used to clean up the laser profile. The laser beam was directed with mirrors M1 and M2 while translation mirror TM1 was used to control the incident angle. The speed of the translational mirrors can be varied. For this work, the slowest setting on the stage movement was utilized. It is noteworthy that the use of a translational mirror to control the incident angle has the potential to reduce acquisition times compared to the use of a rotational stage. The laser light was directed onto the sample by FL2, an aspherical lens (50 mm focal length and 75 mm diameter). The beam was 250 μm in diameter at the air/prism interface. TM2 was used to block the reflected light from reaching the detector.

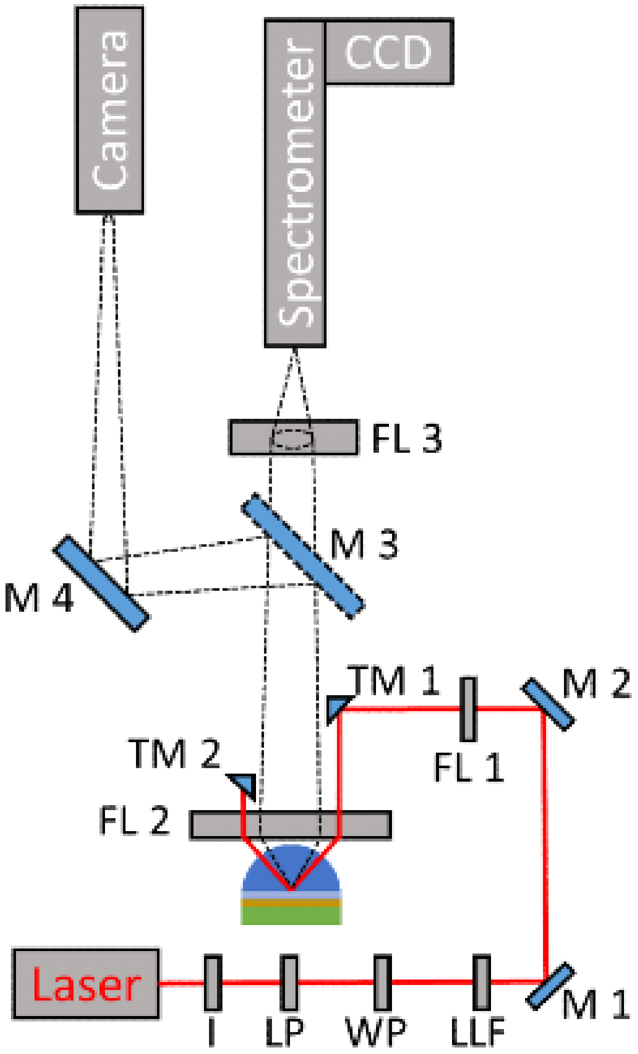

Figure 2. Instrument schematic from the top of the 785-nm excitation directional-surface-plasmon-coupled Raman spectrometer. I: iris, LP: linear polarizer, WP: waveplate (λ/2), LLF: laser line filter, M: mirror, FL: focusing lens, TM: translation mirror, CCD: charge-coupled device. M3 can be flipped down to collect the Raman signal.

Surface-plasmon-polariton Cone Measurements

An image of the cone (i.e., directional Rayleigh signal) was collected with M3 in the light path directing it to M4 and a 75 mm (f/1.3) Kameratori TV Lens (Tampere, Finland) attached to an 11.340 mm × 7.130 mm, 2.32 mega pixel CMOS sensor (IDS Imaging Development Systems GmbH, Obersulm, Germany). Cone images were acquired using software that was integrated with a stepper motor for varying the incident angle of the laser excitation. For the cone intensity measurements, the incident angle range was 0.00° to 60.00° with an angle resolution of 0.06°. The capability of the instrument to image the cone while scanning the incident angle of light for a Weierstrass prism/50-nm thick gold substrate/air interface in the Kretschmann configuration is shown in SI Figure S2 and accompanying movie. All images of the cone were collected with a fixed distance between FL2 and the camera.

Directional-surface-plasmon-coupled Raman Measurements

When M3 was out of the light path, the Raman signal emanating from the full cone was collected on the prism side. The cone of Rayleigh scattering was visualized using an infrared card, confirming the collection of the entire cone. FL3 was a N-BK7 plano-convex lens, (75 mm diameter, 100 mm focal length, Thor Laboratories, Newton, NJ), which was used to focus the light onto a Kaiser HoloSpec Raman spectrometer (Kaiser Optical Systems, Inc. Ann Arbor, MI) with a 100 µm slit and a HSG-785-LF volume phase holographic grating. The detector was a Princeton Instruments (Trenton, NJ) PIXIS 400 1340 × 400 near-infrared-enhanced charged-coupled device (CCD) with 20 µm × 20 µm pixels controlled with the Princeton Instruments WinSpec/32 [v.2.6.14 (2013)] software. The detector was thermoelectrically cooled to -70 °C. Due to efficiency limitations of the instrument components, there is invariably some loss of the Raman scattering prior to detecting the final signal. A solution of acetonitrile-toluene was used for wavelength calibration. Raman data were collected from 34.0° to 54.0° using a 0.2° angle resolution, except within ± 1° of the angle producing the maximum intensity where an angle resolution of 0.06° was used. For the thiophenol monolayer, an acquisition time of 10 s and 3 accumulations was sufficient to obtain a high signal-to-noise ratio spectrum. The Raman spectra of 10 and 50-nm poly(bisphenol A carbonate) were obtained with 180 s and 120 s acquisition times, respectively. For the polystyrene films, the Raman spectra of the 70, 80, 90, and 100-nm were obtained with a 30 s acquisition time and 120 s for the 30 and 60-nm polystyrene films. All spectra of the polymer films used 2 accumulations to facilitate cosmic ray removal. All spectra were collected at room temperature. Three replicates experiments were obtained by taking consecutive scans through the entire incident angle range.

Data Analysis and Calculations

All calculations assumed that all layers have a constant index of refraction for p-polarized 785-nm excitation and were homogeneous. The input parameters were the indices of refraction and thickness of each layer shown in Figure 1. The input refractive indices of sapphire, poly(bisphenol A carbonate), polystyrene, thiophenol, air, and gold at 785 nm were 1.762, 1.571, 1.578, 1.568, 1.000, and 0.10219 (η_{Au}) and 5.0998 (k_{Au}), respectively. The thicknesses of the prism and air layers were semi-infinite compared to the polymer (10 to 100 nm) and the gold (50 nm) layers.

Calculations to model the surface-plasmon-polariton cone were performed using three-dimensional finite-difference time-domain simulations (EM Explorer, San Francisco, CA). The calculated emission cone diameter was obtained from the tangent of the far-field angular radiation pattern depicting the directionality of the scattered light on the prism side and the distance between the prism and the detector as experimentally measured for the instrument shown in Figure 2. The CMOS camera used to measure the cone was calibrated with a metal ruler placed across the planar side of the collection lens (FL2). An image of the metal ruler was acquired and the ruler scale was used to generate a distance per pixel calibration for the CMOS image. The stated cone diameter is for its position at FL2, where the cone has its largest diameter. Since the observed cone diameter is path length dependent, the camera position was fixed for all measurements. The experimental cone diameter was obtained using the CMOS calibration and by fitting the cone with the Radial Profile Plot Java Script in Image-J 1.44p (National Institutes of Health, USA).

The Raman peak amplitude of the 890 cm^{-1} mode of poly(bisphenol A carbonate), 1001 cm^{-1} mode of polystyrene and the 999 cm^{-1} mode of thiophenol was modelled by the sum square electric field (SSEF) generated within the analyte layer. Three-dimensional finite-difference time-domain simulations were used to calculate the SSEF with a Yee cell size of 5 nm, 2000 cycles, a 35.00° to 55.00° angle range and a 0.05° angle resolution. The SSEF calculations that best modelled our experimental Raman peak amplitude measurements used a 785-nm wavelength (i.e., the excitation wavelength). Fresnel reflectivity calculations were performed using IGOR Pro (WaveMetrics, Inc., Lake Oswego, OR) Macros available from Corn et al.[46] to model the cone intensity as a function of incident angle. The angle range was set from 0.000° to 90.000° with a 0.009° angle resolution.

Results and Discussion

Directional RS Instrumentation with Self-assembled Monolayer Sensitivity

Herein, we demonstrate instrumentation that enables the simultaneous collection of the entire surface-plasmon-polariton cone and the Raman scattering as functions of incident angle. It has been pointed out that the collection of the entire cone as a function of incident angle requires a complicated optical setup.[35] Figure 2 shows a simple optical setup that allows the collection of the cone intensity, cone diameter and directional Raman scattering using a single motorized translational mirror to scan the incident angle. We first test how well the cone properties are modelled for a bare gold film prior to showing self-assembled monolayer sensitivity, as the gold film parameters are used to model the latter (Figure 3). For a 50-nm gold film, there is good agreement between the calculated incident angle that produces the maximum attenuation of the reflected light (the surface plasmon resonance angle, 35.530°) and the 35.53° experimental incident angle producing the maximum cone intensity (Figure 3A). The attenuation in the reflected light intensity corresponds to excitation of surface plasmons in the gold film, and the cone is measured at angles where surface plasmons are excited, as expected. Similarly, the experimental cone diameter (Figure 3B) is 2.639 ± 0.003 cm and the calculated cone diameter from the far-field angular radiation pattern (Figure 3C) is 2.662 cm (Figure 3D). The capability of the instrument to image the cone as the incident angle of light is scanned from 0.00° to 60.00° is shown in SI Figure S2 and supporting movie.

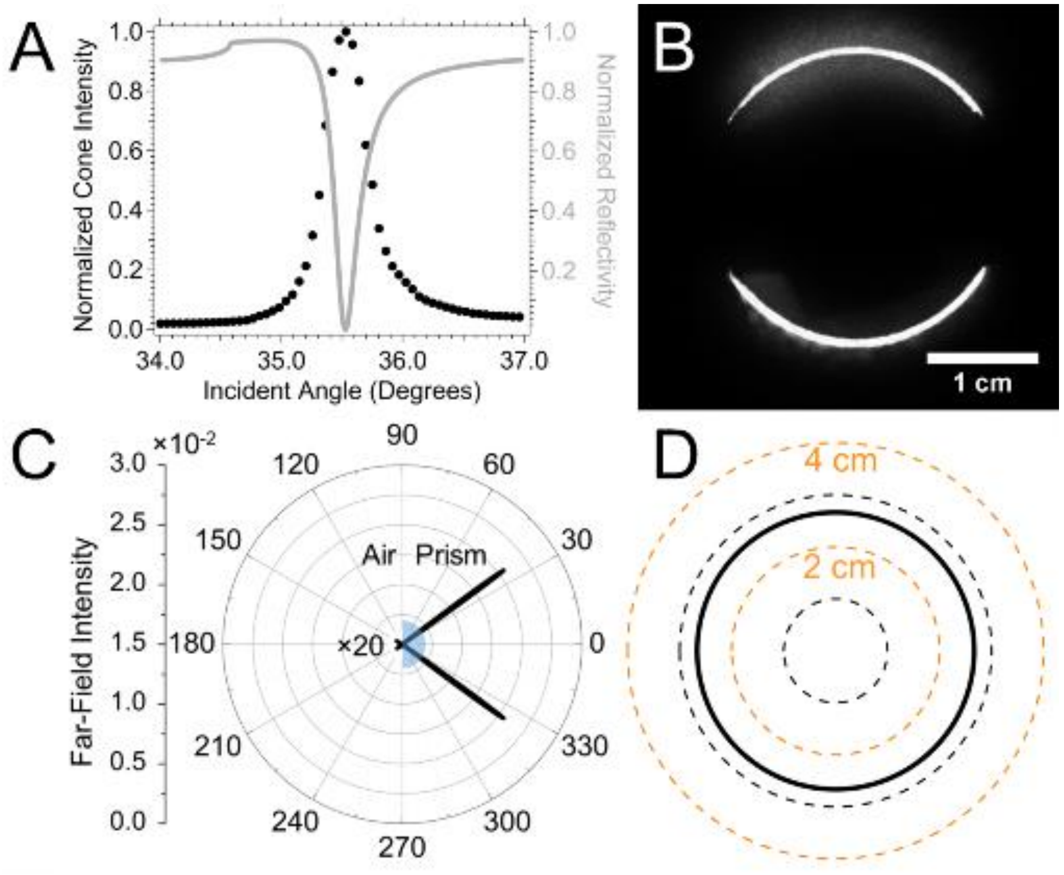

Figure 3. (A) Experimental cone intensity (dotted symbol) and calculated reflectivity (solid gray line) for prism/50-nm gold/air. (B) Cone acquired at an incident angle of 35.53°. Translational mirrors block the incident light (right) and reflected light (left) from reaching the detector, which is why the cone is not continuous. (C) Calculated far-field angular radiation pattern. The far-field intensity on the air side is multiplied by 20. (D) Calculated cone diameter obtained from the far-field angular radiation pattern projected to the far-field.

The directional RS of a self-assembled monolayer of thiophenol on a smooth planar gold film collected at an incident angle of 35.60°, where the maximum cone intensity is observed, is shown in Figure 4A. The bands at 999, 1022, 1177, 1470 and 1573 cm^{-1} in Figure 4A can be assigned to the in-plane ring-breathing mode, in-plane C-H bending mode, in-plane C-H deformation mode, in-plane C-C ring deformation mode, and C-C ring stretching mode, respectively.[47-49] The signal-to-noise ratio of the 999 cm^{-1} Raman mode of thiophenol is 79 when the full Raman signal emanating from the cone is collected for 10 s. McKee et al.[39] reported the signal-to-noise ratio of a thiophenol monolayer on a smooth planar gold film to be 6.8 when the Raman signal is collected for 60 s on the sample side in the Kretschmann configuration (using the same laser, spectrometer and detector as shown in Figure 2). This simple comparison does not take into account some differences in the optics that were used; however, it shows the benefit of collecting the full Raman signal from the surface-plasmon-polariton cone using the instrument shown in Figure 2. This benefit is credited to the magnitude and directionality of the scattered light at a defined angle on the prism side.

Comparing the bare gold film and the thiophenol monolayer, there is a 0.07° shift in the angle that produces the maximum cone intensity. This shift is consistent with what has been reported in the literature for self-assembled monolayers measured by surface plasmon resonance where the reflectivity minimum is measured.[50-52] Similarly, there is an increase in the cone diameter comparing the bare gold film (2.639 ± 0.003 cm) and the monolayer (2.863 ± 0.005 cm) as shown in Figure 4B. The increase in the angle that produces the maximum cone intensity and the increase in the cone diameter are attributed to the changes in the local refractive index of the dielectric medium adjacent to the gold film. Both parameters exhibit monolayer sensitivity, and sub-monolayer sensitivity is expected.

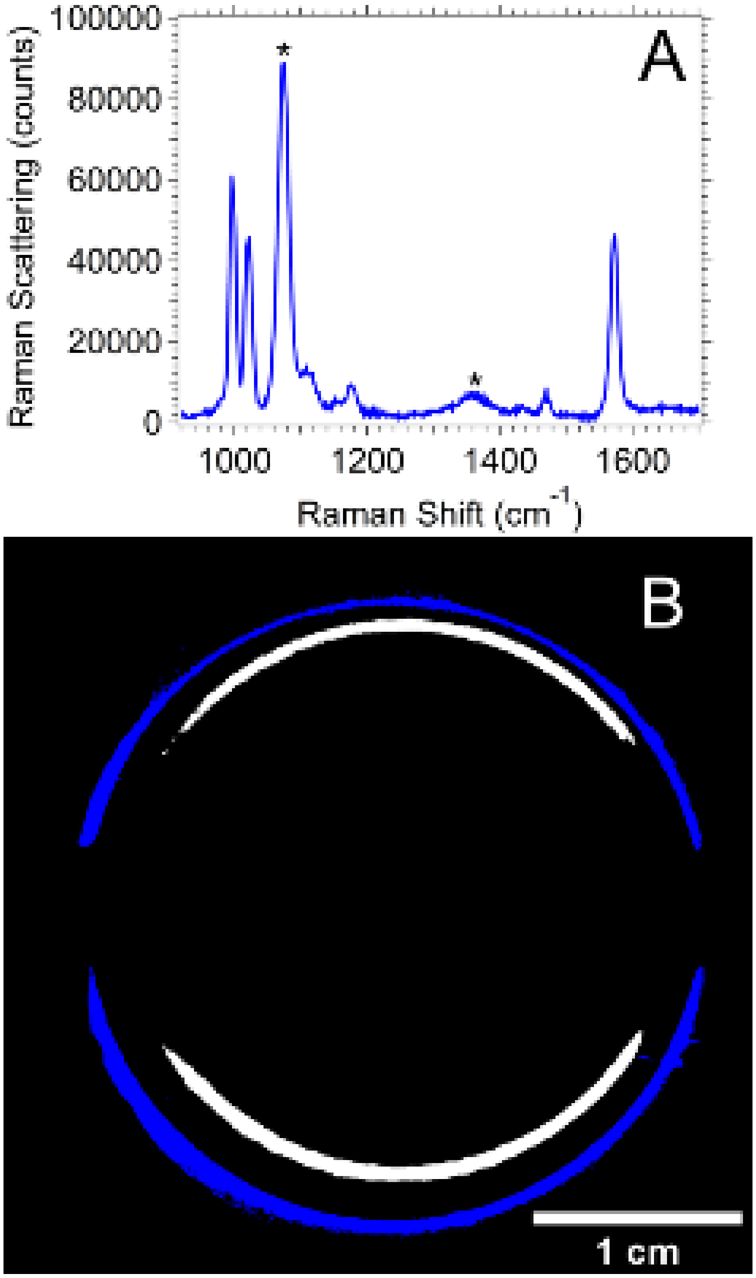

Figure 4. (A) Directional Raman spectrum of a self-assembled monolayer of thiophenol at a Weierstrass prism/50-nm gold/thiophenol/air interface in the Kretschmann geometry. The acquisition time is 10 s with 3 accumulations using an incident power of 200 mW. The asterisks (*) represent a peak that originates from the sapphire prism. (B) An overlay of the surface-plasmon-polariton cones for (blue) thiophenol self-assembled monolayer and (white) bare gold film acquired at the incident angle producing the maximum cone intensity of 35.60° and 35.53°, respectively.

Quantification and Modelling of the Cone Diameter, Cone Intensity, and Raman Scattering

Polymer films of ~10 to 100-nm thickness were used to quantify the cone intensity and diameter. An image of the overlaid experimental cones for 10 and 50-nm poly(bisphenol A carbonate) films (Figure 5A) and 30, 60, 70, 80, 90, 100-nm polystyrene films (Figure 5B) are shown at the incident angle producing the maximum cone intensity, which varies with each sample as discussed below. The calculated cone diameters for poly(bisphenol A carbonate) films (Figure 5C) and polystyrene films (Figure 5D) correlate very well with the experimental cone diameters in Figure 5A and 5B, with an average percent difference of 1%. The emission cone diameter increases with increasing sample thickness due to the increase in the angle of the directionally scattered light through the Weierstrass prism as shown by the calculated far-field angular radiation pattern (Figure S3). Both the calculated and experimentally measured cone diameter quadratically increase with polymer thickness (Figure 5E). While the absolute cone diameter is dependent on the system optics, it can be concluded that the cone diameter is sensitive to the thickness of the adsorbate layer (as quantified below).

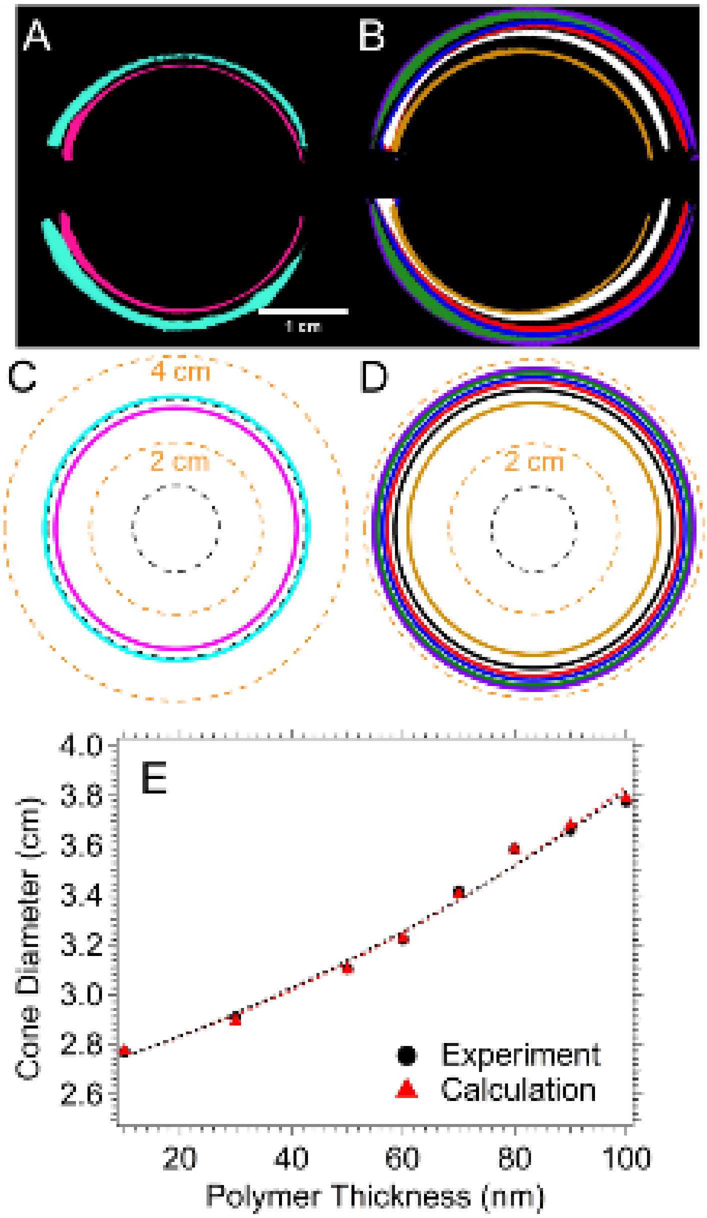

Figure 5. (A, B) Experimentally measured and (C, D) calculated surface-plasmon-polariton cone for 10 nm (pink), 30 nm (gold), 50 nm (cyan), 60 nm (white/black), 70 nm (red), 80 nm (blue), 90 nm (green) and 100 nm (purple) polymer films. Polymer films are composed of (A, C) poly(bisphenol A carbonate) and (B, D) polystyrene. The experimental and calculated cones have been overlaid for easier comparison. The calculated cone used the polymer thicknesses obtained from profilometry measurements (SI Figure 1S). The incident angles at which the experimental cones were collected are 36.00°, 37.45°, 40.15°, 40.94°, 43.59°, 45.76°, 48.00°, and 50.22° for the increasing polymer thicknesses, respectively. The indices of refraction for poly(bisphenol A carbonate) and polystyrene are the same under these experimental conditions. (E) Graphs of experimental (black circle) and calculated (red triangle) cone diameter as a function of polymer thickness. The black dashed line represents a polynomial fit for the experimental data and the red dash line represents a polynomial fit for the calculated data ($y = (2.679 \pm 0.005) + (0.0067 \pm 0.0005)x + (0.000047 \pm 0.000006)x^2$; $R^2 = 0.988$).

Figure 6A and 6B show the measured cone intensity and calculated reflected light intensity from the interface as a function of incident angle for the polymer samples. As with the calibration plot for the cone diameter (Figure 5E), the incident angle that produces the maximum cone intensity quadratically increases with polymer thickness (Figure 6C). SPR-based techniques are inevitably not linear over a broad range of thicknesses or indices of refraction as reported by Corn et al.,[53] although the calibration can be considered linear over a narrow range of thicknesses or indices of refraction. Additionally, the cone intensity as a function of incident angle is well modelled by the calculated surface plasmon resonance angle and is sensitive to sample thickness.

The Raman spectra of 10-nm poly(bisphenol A carbonate) and 100-nm polystyrene films collected at an incident angle that produces the largest signal are shown in Figure S4. There are only minor differences in the relative intensities of the peaks when comparing the spectra for the bulk powder and the thin films; these minor differences can be explained by the varying spectral background. The directional RS data collected over the full range of incident angles for the poly(bisphenol A carbonate) (Figure 7A, C) and polystyrene (Figure 7B, D, E, F, G, and H) films with varying thicknesses are plotted as their Raman shift versus the incident angle with the color scale representing the Raman scattering intensities.

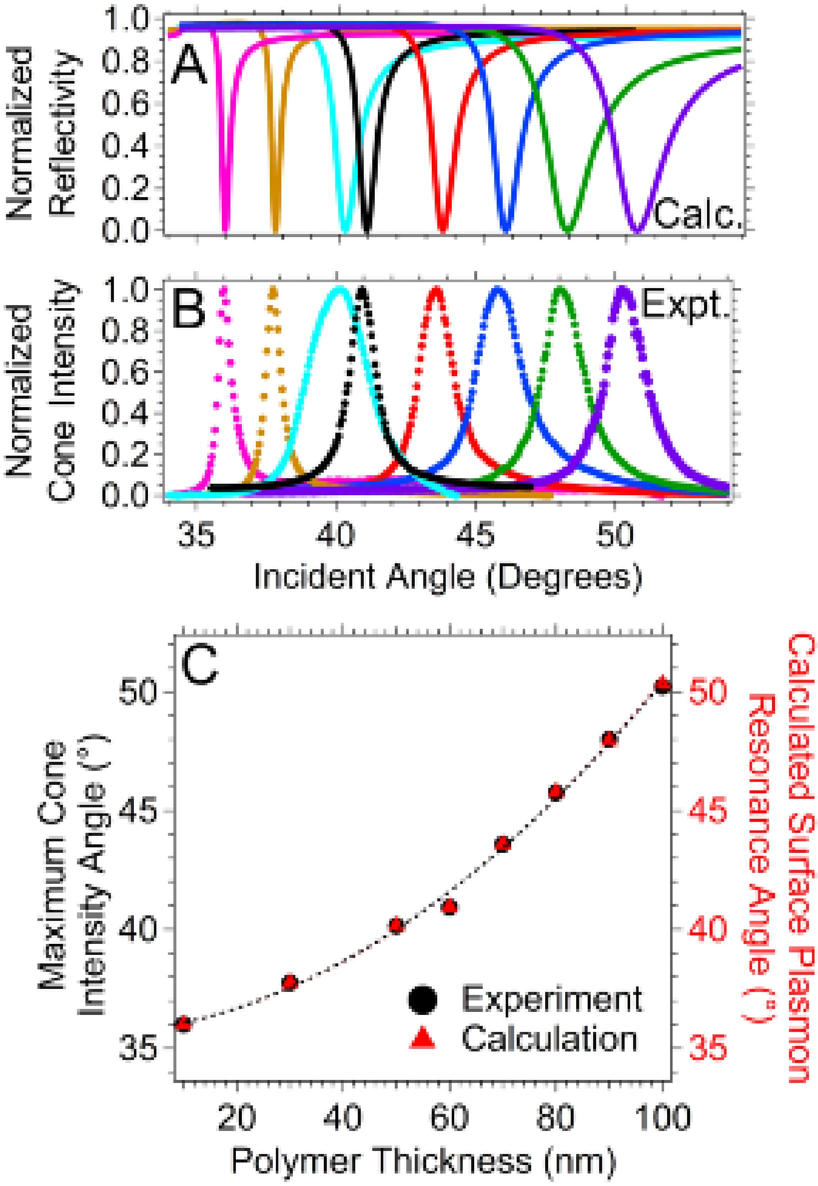

Figure 6. (A) Calculated angle dependent reflectivity curves and (B) the measured angular dependence of the surface-plasmon-polariton cone intensity for 10 nm (pink), 50 nm (cyan) poly(bisphenol A carbonate) and 30 nm (gold), 60 nm (black), 70 nm (red), 80 nm (blue), 90 nm (green) and 100 nm (purple) polystyrene films. (C) Plot of the measured incident angle that produces the maximum cone intensity (black circle) and the calculated surface plasmon resonance angle using the polymer thickness obtained from profilometry measurements (red triangle). The black dashed line represents a polynomial fit for the experimental data and the red dash line represents a polynomial fit for the calculated data ($y = (35.70\pm0.02) + (0.025\pm0.001)x + (0.00123\pm0.00002)x^2$; $R^2 = 0.998$).

The 890 cm^{-1} and 995 cm^{-1} peaks assigned to poly(bisphenol A carbonate) have the highest intensity in the angular range from 35.92° to 36.19° for the 10-nm film (Figure 7A). The 1001 cm^{-1} and 1023 cm^{-1} Raman peaks of polystyrene have the highest intensity in the angular range from 36.03° to 38.78° for the 30-nm film (Figure 7B). There is also an increase in the background at the angles that produce the maximum Raman scattering. A cross-section of the peak amplitude (solid colored lines) and the calculated sum square electric field as a function of incident angle (dashed gray line) show a good agreement for all the polymer films (Figure 7I). A quadratic increase in the angle producing the maximum Raman scattering intensity is observed with increasing polymer thickness. Averaging over all the samples, the maximum Raman scattering intensity is measured within 0.5° of the angle producing the maximum cone intensity.

The smallest difference in the adsorbate thickness (i.e., with a ~1.575 index of refraction) that can be measured when considering the limits of the instrument resolution is the same for all three parameters collected on the directional RS instrument and is 0.6 nm. When measuring the cone intensity and Raman scattering, future iterations of the instrumentation can be improved with an angular resolution of 0.001 degrees. The smallest change in the cone diameter that can be measured is 0.4 cm, this parameter could also be improved by other image processing methods and using a camera with a larger sensitive area. Future instrument designs will compare well with standard SPR instrumentation, and of course have the added capability to perform sensitive *in situ* Raman measurements.

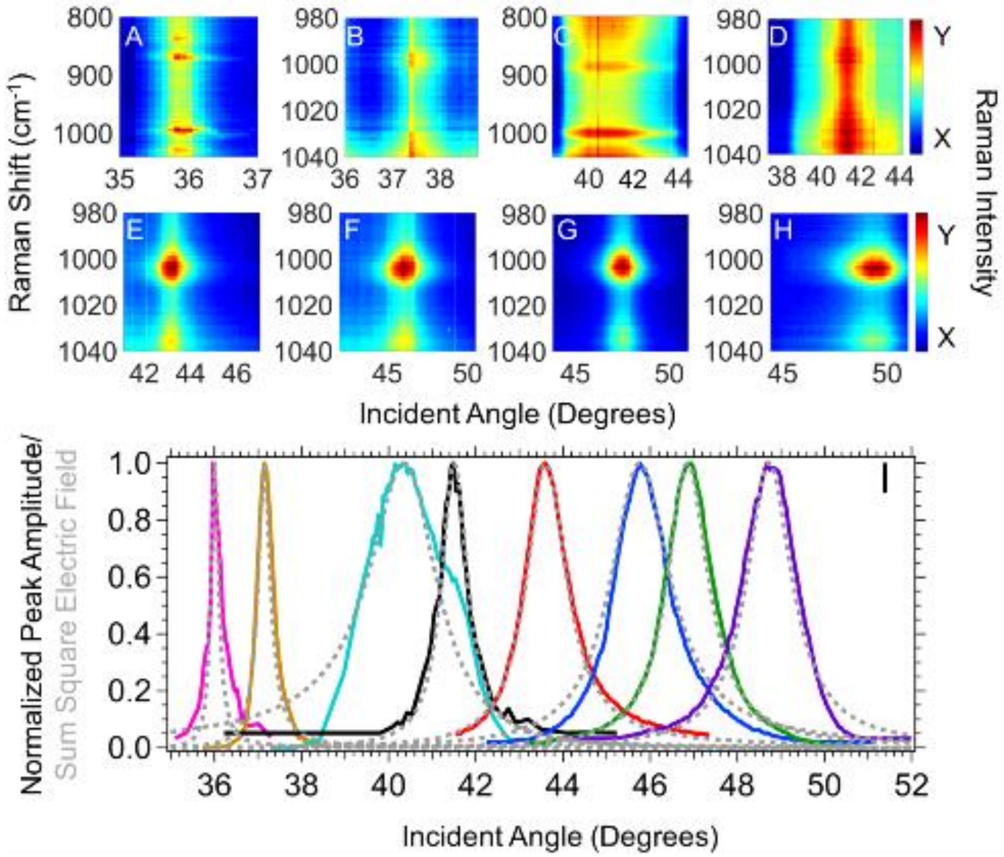

Figure 7. (A-H) Raman scattering intensity as a function of Raman shift and incident angle on a color amplitude scale. (A, C) Polymer films are composed of 10 and 50-nm thick poly(bisphenol A carbonate) and (B, D, E, F, G, and H) 30, 60, 70, 80, 90, 100-nm polystyrene. The Raman scattering intensity scale in units of counts is designated by X and Y in the color scale, with (A) X,Y = 6,000 to 18,000, (B) X,Y = 80,000 to 120,000, (C) X,Y = 15,000 to 32,000, (D) X,Y = 40,000 to 80,000, (E) X,Y = 15,000 to 30,000, (F and G) X,Y = 10,000 to 20,000, and (H) X,Y = 5,000 to 20,000. (I) Peak amplitude versus incident angle of the 890 cm^{-1} mode of poly(bisphenol A carbonate) and 1001 cm^{-1} mode of polystyrene, (pink) 10 nm, (gold) 30 nm, (cyan) 50 nm, (black) 60 nm, (red) 70 nm, (blue) 80 nm, (green) 90 nm, (purple) 100 nm film (solid line) and the sum square electric field (dashed gray line) calculated using the sample thickness obtained from profilometry measurements. The standard deviation from three replicate experimental measurements is not perceptible on this scale. The acquisition times for the 10 and 50-nm poly(bisphenol A carbonate) films were 180 s and 120 s, respectively. For the 70, 80, 90, and 100-nm polystyrene films, the Raman spectra were collected for 30 s and for the 30 and 60-nm polystyrene films a 120 s acquisition time was used. All polymer film spectra had 2 accumulations to facilitate cosmic ray removal.

Conclusions

The directional RS method enables the simultaneous collection of the surface-plasmon-polariton cone intensity, cone diameter and Raman scattering as a function of incident angle with a single instrument. The quantitative study of all three parameters using a thiophenol monolayer and thin polymer films as model samples has been presented. Overall, all three measured parameters are well modelled with simple calculations and exhibit a quadratic dependence within a broad range of adsorbate thickness. It is important to note, while the films used to demonstrate the quantitative relationship of each parameter and adsorbate thickness were homogeneous, the multi-parameter directional RS method will be very beneficial for analyzing multicomponent films. For example, the index of refraction, thickness and chemical content of the multicomponent films can be simultaneously measured. The multi-parameter analysis will be useful for smooth films where the film morphology and composition affect its function, such as many films used in energy capture and conversion devices. In addition, the directional Raman signal with the combined measurement of the surface-plasmon-polariton cone will be a useful alternative to surface plasmon resonance spectroscopy when added chemical measurements are beneficial.

Acknowledgements

This research was supported by the U.S. Department of Energy, Office of Science, Basic Energy Sciences, Chemical Sciences, Geosciences, and Biosciences Division. The research was performed at the Ames Laboratory, which is operated for the U.S. DOE by Iowa State University under contract # DE-AC02-07CH11358. Profilometry measurements were performed at the Iowa State University W.M. Keck Microfabrication Facility. The authors declare competing financial interest(s): Stephen C. Weibel has financial interest in the commercial development of this technology.

References

1. Y. Wang, J. Dostalek and W. Knoll, *Procedia Eng.* 2010, **5**, 1017-1020.
2. A. Abbas, M. J. Linman and Q. Cheng, *Sens. Actuators, B* 2011, **156**, 169-175.
3. B. Liedberg, C. Nylander and I. Lunström, *Sens. Actuators* 1983, **4**, 299-304.
4. L. A. Lyon, M. D. Musick and M. J. Natan, *Anal. Chem.* 1998, **70**, 5177-5183.
5. E. A. Smith, W. D. Thomas, L. L. Kiessling and R. M. Corn, *J. Am. Chem. Soc.* 2003, **125**, 6140-6148.
6. J. S. Yuk, G. N. Gibson, J. M. Rice, E. F. Guignon and M. A. Lynes, *Analyst* 2012, **137**, 2574-2581.
7. J.-F. Masson, *ACS Sens.* 2017, **2**, 16-30.
8. J. Matsui, K. Akamatsu, N. Hara, D. Miyoshi, H. Nawafune, K. Tamaki and N. Sugimoto, *Anal. Chem.* 2005, **77**, 4282-4285.
9. D. A. Woods and C. D. Bain, *Analyst* 2012, **137**, 35-48.
10. R. Iwamoto, K. Ohta, M. Miya and S. Mima, *Appl. Spectrosc.* 1981, **35**, 584-587.
11. T. Ikeshoji, Y. Ono and T. Mizuno, *Appl. Opt.*, 1973, **12**, 2236-2237.
12. D. A. Beattie, M. L. Larsson and A. R. Holmgren, *Vib. Spectrosc.* 2006, **41**, 198-204.
13. C. Chen, L. Dan-Feng, G. Ran, C. Jin and Q. Zhi-Mei, *Appl. Phys. Express* 2016, **9**, 062001.
14. R. K. Fisher and R. W. Gould, *Phys. Rev. Lett.* 1969, **22**, 1093-1095.
15. A. Webster and F. Vollmer, *Opt. Lett.* 2013, **38**, 244-246.
16. M. Futamata, *Appl. Opt.* 1997, **36**, 364-375.
17. J. Giergiel, C. E. Reed, J. C. Hemminger and S. Ushioda, *J. Phys. Chem.* 1988, **92**, 5357-5365.
18. W. Wittke, A. Hatta and A. Otto, *Appl. Phys. A*, 1989, **48**, 289-294.
19. A. J. Braundmeier and H. E. Tomaschke, *Opt. Commun.* 1975, **14**, 99-103.
20. N. Calander, *Anal. Chem.* 2004, **76**, 2168-2173.

21. C. Chen, D.-F. Lu, R. Gao and Z.-M. Qi, *Opt. Commun.* 2016, **367**, 86-94.

22. D. G. Zhang, K. J. Moh and X. C. Yuan, *Opt. Express*, 2010, **18**, 12185-12190.

23. J. S. Yuk, M. Trnavsky, C. McDonagh and B. D. MacCraith, *Biosens. Bioelectron.* 2010, **25**, 1344-1349.

24. I. Gryczynski, J. Malicka, K. Nowaczyk, Z. Gryczynski and J. R. Lakowicz, *Thin Solid Films* 2006, **510**, 15-20.

25. I. Gryczynski, J. Malicka, Z. Gryczynski, K. Nowaczyk and J. R. Lakowicz, *Proc. SPIE* 2004, **5327**, 37-44.

26. I. Gryczynski, J. Malicka, K. Nowaczyk, Z. Gryczynski and J. R. Lakowicz, *J. Phys. Chem. B*, 2004, **108**, 12073-12083.

27. I. Gryczynski, J. Malicka, J. Lukomska, Z. Gryczynski and J. R. Lakowicz, *Photochem. Photobiol.* 2004, **80**, 482-485.

28. S. Byahut and T. E. Furtak, *Rev. Sci. Instrum.* 1990, **61**, 27-32.

29. M. Futamata, P. Borthen, J. Thomassen, D. Schumacher and A. Otto, *Appl. Spectrosc.* 1994, **48**, 252-260.

30. M. Futamata, *Langmuir*, 1995, **11**, 3894-3901.

31. M. Futamata, E. Keim, A. Bruckbauer, D. Schumacher and A. Otto, *Appl. Surf. Sci.* 1996, **100**, 60-63.

32. M. Futamata, *J. Phys. Chem.* 1995, **99**, 11901-11908.

33. H. Li, S. Xu, Y. Liu, Y. Gu and W. Xu, *Thin Solid Films* 2012, **520**, 6001-6006.

34. S. A. Meyer, B. Auguié, E. C. Le Ru and P. G. Etchegoin, *J. Phys. Chem. A* 2012, **116**, 1000-1007.

35. S. A. Meyer, E. C. Le Ru and P. G. Etchegoin, *Anal. Chem.* 2011, **83**, 2337-2344.

36. S.-X. Huo, Q. Liu, S.-H. Cao, W.-P. Cai, L.-Y. Meng, K.-X. Xie, Y.-Y. Zhai, C. Zong, Z.-L. Yang, B. Ren and Y.-Q. Li, *J. Phys. Chem. Lett.* 2015, **6**, 2015-2019.

37. J. M. Bobbitt, D. Mendivelso-Pérez and E. A. Smith, *Polymer* 2016, **107**, 82-88.

38. C. A. Damin, V. H. T. Nguyen, A. S. Niyibizi and E. A. Smith, *Analyst* 2015, **140**, 1955-1964.

39. K. J. McKee, M. W. Meyer and E. A. Smith, *Anal. Chem.* 2012, **84**, 4300-4306.

40. K. J. McKee, M. W. Meyer and E. A. Smith, *Anal. Chem.* 2012, **84**, 9049-9055.

41. K. J. McKee and E. A. Smith, *Rev. Sci. Instrum.* 2010, **81**, 043106.

42. M. W. Meyer, K. L. Larson, R. C. Mahadevapuram, M. D. Lesoine, J. A. Carr, S. Chaudhary and E. A. Smith, *ACS Appl. Mater. Interfaces* 2013, **5**, 8686-8693.

43. M. W. Meyer, K. J. McKee, V. H. T. Nguyen and E. A. Smith, *J. Phys. Chem. C* 2012, **116**, 24987-24992.

44. M. D. Lesoine, J. M. Bobbitt, S. Zhu, N. Fang and E. A. Smith, *Anal. Chim. Acta* 2014, **848**, 61-66.

45. J. M. Bobbitt, S. C. Weibel, M. Elshobaki, S. Chaudhary and E. A. Smith, *Anal. Chem.* 2014, **86**, 11957-11961.

46. Corn RM *Complex Fresnel Calculations For Igor Pro Macros available from http://corninfo.ps.uci.edu/writings/Ref4txt.html* **2014**.

47. M. A. Bryant, S. L. Joa and J. E. Pemberton, *Langmuir*, 1992, **8**, 753-756.

48. R. Holze, *Phys. Chem. Chem. Phys.* 2015, **17**, 21364-21372.

49. W. K. Yi, C.-W. Park, M.-S. Kim and K. Kim, *Bull. Korean Chem. Soc.* 1987, **8**, 291-296.

50. Y. Liu, S. Xu, H. Li, X. Jian and W. Xu, *Chem. Commun.* 2011, **47**, 3784-3786.

51. C. Fu, C. Hu, Y. Liu, S. Xu and W. Xu, *Anal. Methods* 2012, **4**, 3107-3110.

52. B. P. Nelson, A. G. Frutos, J. M. Brockman and R. M. Corn, *Anal. Chem.* 1999, **71**, 3928-3934.

53. A. G. Frutos, S. C. Weibel and R. M. Corn, *Anal. Chem.* 1999, **71**, 3935-3940.

Supporting Information

Thickness of poly(bisphenol A carbonate) and polystyrene films measured by profilometry can be found in supplemental information Figure S1. Cone images at selected incident angles and a movie (.AVI file) to go along with the cone images can be found in supplemental information Figure S2. Calculated far-field angular radiation pattern for the cone diameters shown in Figure 5, can be found in supplemental information Figure S3. The Raman spectra of 10-nm poly(bisphenol A carbonate) and 100-nm polystyrene films from the data set shown in Figure 7, can be found in supplemental information Figure S4.

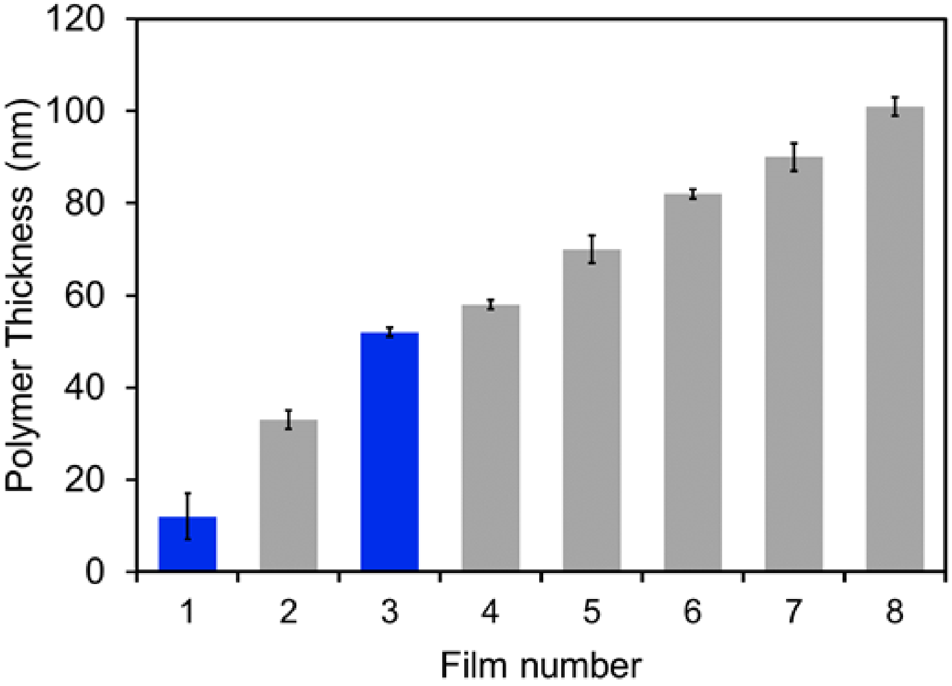

Figure S1. Thickness of poly(bisphenol A carbonate) and polystyrene samples measured by optical profilometry. Data shaded in blue are poly(bisphenol A carbonate) and data shaded in gray are polystyrene. Uncertainties represent one standard deviation.

Figure S2. Selected cone images at the designated incident angle from the provided supplemental movie. The incident angle was scanned from 0.00° to 60.00°. The movie is included in the Supplemental Information as an AVI file. All images of the cone were collected with a fixed distance between FL2 and the camera. The scale bare represents 1 cm.

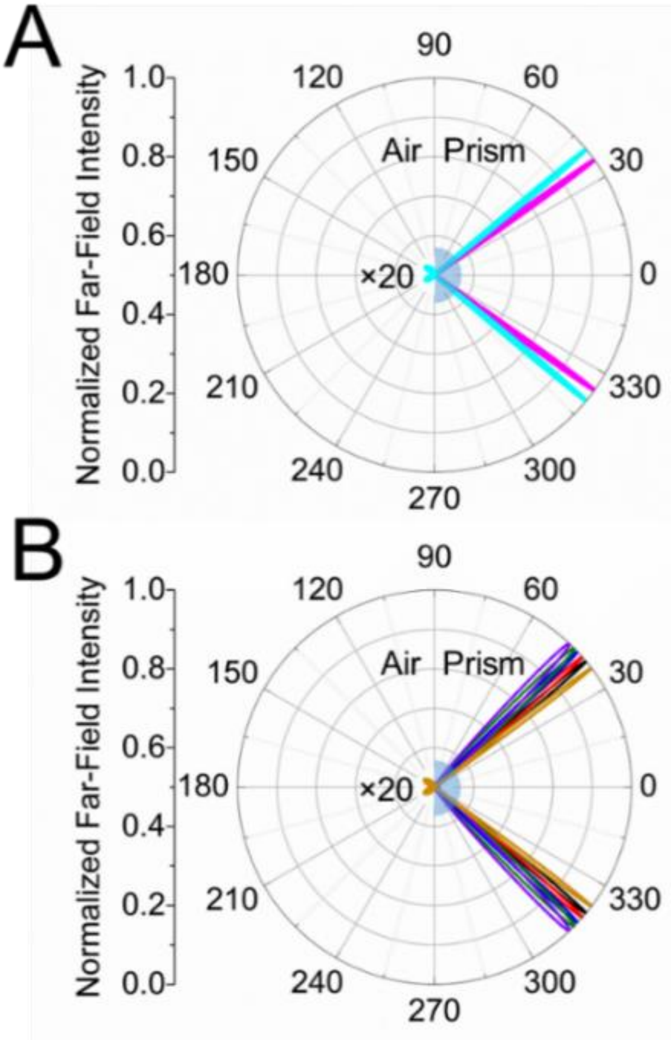

Figure S3. Calculated far-field angular radiation pattern for (A) 10 nm (pink) and 50 nm (cyan) poly(bisphenol A carbonate) and (B) 30 nm (gold), 60 nm (black), 70 nm (red), 80 nm (blue), 90 nm (green), and 100 nm (purple) polystyrene films. The angles of the directional scattered light are (A) 35.77° (10 nm), and 39.64° (50 nm), and (B) 37.17° (30 nm), 40.779° (60 nm), 43.19° (70 nm), 45.61° (80 nm), 46.35° (90 nm), and 47.55° (100 nm), respectively. The angular radiation pattern on the air side has been multiplied by 20.

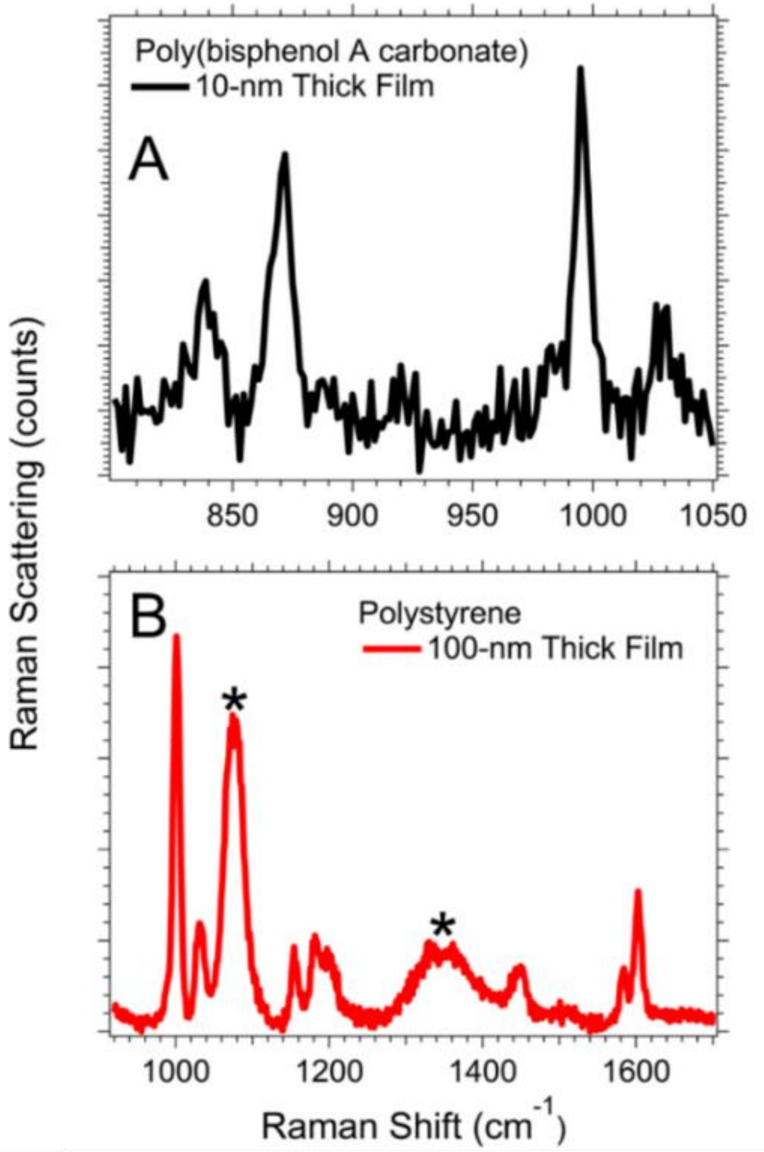

Figure S4. The directional-surface-plasmon-coupled Raman scattering spectra of (A) 10-nm poly(bisphenol A carbonate) and (B) 100-nm polystyrene adsorbed on a smooth planar gold film acquired at incident angles (θ_{inc}) of 36.00° and 48.75°, respectively. The acquisition time was 180 s with 2 accumulation for the 10-nm poly(bisphenol A carbonate) film and 30 s with 2 accumulations for the 100-nm polystyrene film. The asterisk (*) represents peaks that originate from the sapphire prism.

CHAPTER 4. EXPERIMENTAL ANALYSIS OF WAVEGUIDE-COUPLED SURFACE-PLASMON-POLARITON CONE PROPERTIES

Charles K. A. Nyamekye[a,b], Qiaochu Zhu[b], Russell Mahmood[c], Stephen C. Weibel[d], Andrew C. Hillier[a,c], Emily A. Smith[a,b] *

[a] U.S. Department of Energy, The Ames Laboratory, Ames, Iowa 50011, United States

[b] Department of Chemistry, Iowa State University, Ames, Iowa 50011, United States

[c] Department of Chemical and Biological Engineering, Iowa State University, Ames, Iowa 50011, United States

[d] Surface Photonics Inc., Madison, Wisconsin 53719, United States

[*] Corresponding Author (esmith1@iastate.edu, 2415 Osborn Drive, Ames 50011; 1-515-294-1424)

Modified from a manuscript published in Analytica Chimica Acta

Abstract

Experimental data for waveguide-coupled surface-plasmon-polariton (SPP) cones generated from dielectric waveguides is presented. The results demonstrate a simpler route to collect plasmon waveguide resonance (i.e., PWR) data. In the reverse-Kretschmann configuration (illumination from the sample side) and Kretschmann configuration (illumination from the prism side), all the waveguide modes are excited simultaneously with p- or s-polarized incident light, which permits rapid acquisition of PWR data without the need to scan the incident angle or wavelength, in the former configuration. The concentric SPP cone properties depend on the thickness and index of refraction of the waveguide. The angular intensity pattern of the cone is well-matched to simulation results in the reverse-Kretschmann configuration, and is found to be dependent on the polarization of the incident light and the polarization of the waveguide mode. In the Kretschmann geometry, all waveguide-coupled SPP cones are measured at incident

angles that produce attenuated light reflectivity. In addition, the enhanced electric field produced under total internal reflection allows high signal-to-noise ratio multimodal spectroscopies (e.g., Raman scattering, luminescence) to measure the chemical content of the waveguide film, which traditionally is not measured with PWR.

Introduction

Surface-plasmon-polariton-coupled analysis techniques are useful methods for studying thin films, optical waveguides, and for monitoring real-time adsorption of molecules onto a metal surface [1-13]. Plasmon waveguide resonance (PWR), for example, uses both p- and s-polarized incident light to generate guided modes within a waveguide dielectric material [14-17]. In a typical PWR experiment, the reflectivity of light is monitored from a prism/waveguide film as a function of incident angle or wavelength. PWR is particularly useful for measuring the properties of anisotropic films.

Two common illumination geometries used in SPP-coupled spectroscopies are the Kretschmann (Figure 1) and reverse-Kretschmann (Figure 2) configurations. Both configurations consist of an optically-coupled lower-refractive-index sample, a thin metal film and a higher-refractive-index prism. When surface plasmons are excited in the Kretschmann configuration, a hollow cone of directionally scattered light (the surface-plasmon-polariton cone, or SPP cone) is generated on the prism side at a defined angle due to momentum conserving optical and roughness coupling [18]. The collection of the SPP cone from a prism/55-nm silver film/air interface onto photographic film was demonstrated by Simon and Guha in 1976 [19]. We recently reported an optical setup for collecting the full SPP cone image as a function of incident angle as well as the quantification of the SPP cone properties for a thiophenol monolayer and thin (< 100-nm) polymer films [1].

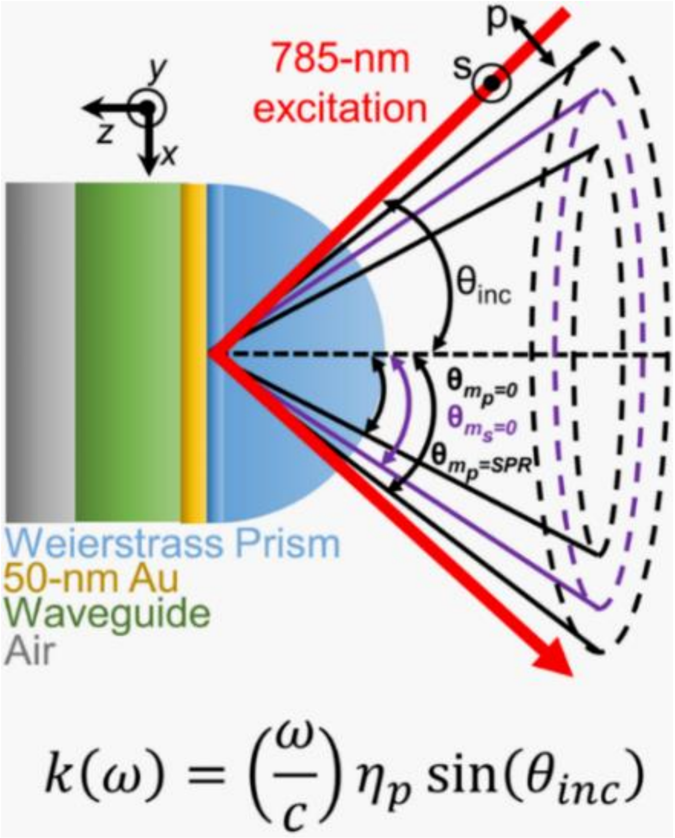

Figure 1. Schematic of the Kretschmann configuration. Multiple concentric SPP cones are measured for the analysis of waveguide samples. A Weierstrass prism is a hyper-hemisphere, which enables the full SPP cone to be measured. Surface plasmons are excited when the electron oscillation frequency of the metal substrate matches the wave vector $k(\omega)$ of incident light that travels through a prism with index of refraction η_p. (frequency of light ω, incident angle of light θ_{inc}, speed of light in a vacuum c)

A SPP cone can also be produced in the reverse-Kretschmann configuration, wherein the incident laser illuminates from the sample side with an orientation that is perpendicular to the interface. The angular intensity of the SPP cone (defined in Figure 3) on the prism side varies with both the polarization of the incident light and the scattered light. Braundmeier and Tomaschke [18] reported on the angular intensity patterns of the SPP cone with p- and s-polarized light incident on the air/Ag/prism interface in the reverse-Kretschmann configuration. A single SPP cone with a nonuniform angular intensity pattern was observed. The maximum cone intensity was recorded in the vertical plane for s-polarized incident light and horizontal plane for p-polarized light. The authors concluded that the maximum intensities around the SPP cone match the orientation of the incoming photons, although the angular intensity pattern of the SPP cone was not modeled.

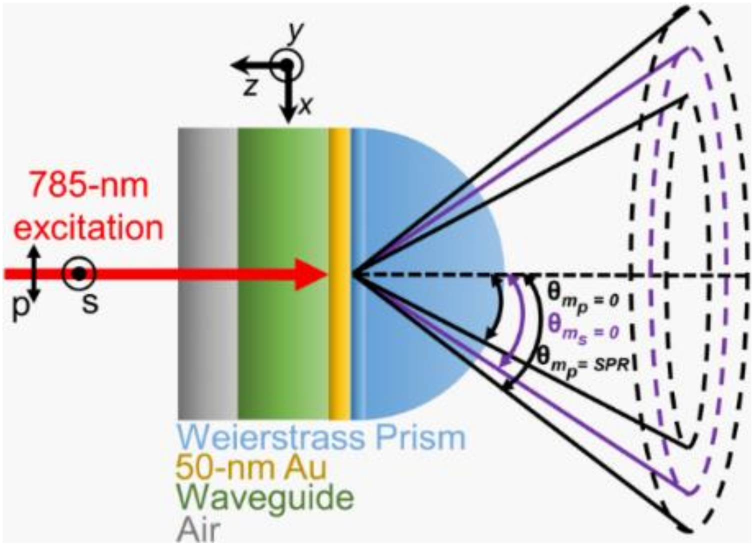

Figure 2. Schematic of the reverse-Kretschmann configuration. Illumination is from the sample side and the incoming rays are at normal incidence to the sample.

Previous reports showing SPP cones did not study waveguide films, rather they focused on bare metal films or thin films that did not meet the waveguide criterion. Plasmon waveguide structures consist of a thin metal film coated with a dielectric layer of thickness ~ $\frac{\lambda}{2\eta}$ or greater, where λ is the excitation wavelength and η is the dielectric material's refractive index [20, 21]. Several waveguide-coupled spectroscopies have been reported that enable sensitive measurements as a result of the enhanced signals produced by the resonant excitation of electromagnetic modes in the waveguide structure [16, 22-24]. To date, these techniques have not relied on measurements of the waveguide-coupled SPP cones, despite the useful information that they encode and the simplicity of not needing to scan the incident angle or wavelength of light. This may be in part due to the lack of experimental data for waveguide-coupled SPP cones.

(Experimentally measured data has, it should be noted, been reported for a related technique called surface-plasmon-coupled emission (SPCE) wherein the signal originates from fluorophores located in close proximately to a metallic surface [25-29]. In these experiments, the SPCE cones were projected onto a flat surface, which was subsequently photographed).

Simulations to model directional scattering phenomena have been reported by Nils Calander [30] and Zhi-Mei Qi [31, 32]. Calander's simulation was based on Fresnel's equations and the Weyl identity theorem for expressing the electromagnetic energy density of the cone emanating from a dipole inside a thin polymer film. The simulation results were comparable to the experimental SPCE results of Gryczynski, Lakowicz, and Malicka [25, 27, 33, 34]. Qi and coworkers' simulations were based on Fresnel's equations and optical reciprocity theorem [31, 32]. They simulated a plasmon waveguide structure in the Kretschmann configuration with a dipole emitter positioned at various locations within the waveguide dielectric layer, which was placed between a gold film and an air layer. The authors concluded that the angular intensity of the waveguide-coupled SPP cones was influenced by the dipole's orientation and distance from the metal surface. No experimental waveguide-coupled SPP cone data were presented.

Herein, we report the experimentally measured properties of waveguide-coupled SPP cones with reverse-Kretschmann and Kretschmann illumination geometries. The experimental properties measured in the reverse-Kretschmann configuration include the angular intensity patterns of the waveguide-coupled SPP cones, their polarization dependence, and cone angles. In the Kretschmann configuration, in addition to images of the waveguide-coupled SPP cones, the directional Raman signal is also recorded. The signals are well modeled using standard optical modeling [30, 35] and three-dimensional finite-difference time-domain simulations. We propose that the waveguide-coupled SPP cone properties reported herein enable a simple and information-rich method for collecting plasmon waveguide resonance data in a single image without the need to scan the incident angle or frequency of light during data collection.

Materials and Methods

Sample Preparation

The waveguide samples were prepared on 25.4 mm diameter sapphire substrates obtained from Meller Optics (Providence, RI). Prior to preparing the waveguide films, a 2-nm titanium (99.999% pure Ti) adhesive layer and 50-nm gold (99.999% pure Au) layer were deposited on clean sapphire disks. The metal deposition was performed by Platypus Technologies LLC., Madison, WI. The surface roughness (RMS) of the gold deposition was 0.2 nm (reported by the film manufacturer). The gold films were immersed in piranha solution (3:1 mixture of sulfuric acid (assay 99.999%, CAS# 7664-93-9, Sigma-Aldrich St. Louis, MO) and hydrogen peroxide (assay 31.7%, CAS# 7722-84-1, Fisher Chemical Pittsburgh, PA) for three minutes to ensure a clean gold surface. **[Piranha solution will cause chemical and thermal burns if not handled with extreme caution]**. Deionized water from an 18.2 MΩ cm^{-1} EasyPure II filtration system (Thermo Scientific, Waltham, MA) was used to rinse the gold films after the piranha cleaning process. A 50:50 (v/v) 200 proof ethanol (assay 99.5%, CAS# 64-17-5, Sigma-Aldrich St. Louis, MO) and deionized water mixture was prepared for sonicating the gold films for five minutes with an ultrasonic cleaner followed by drying in a stream of N_2 gas.

A sputter-up-type sputtering system (ATC 1800-F, AJA International, Scituate, MA) was used for RF sputtering ~400-nm of silica (SiO_2, purity 99.0-99.9999%) onto a 2-nm Ti/50-nm Au coated sapphire disk substrate. The sputtering system was equipped with a quartz crystal thickness monitor (TM-350/400, Maxtek Inc, Cypress, CA). Silica sputtering was achieved using a RF power of 135 W, argon pressure of ~3 mTorr and a substrate rotation rate of 20 rpm. Poly(methyl methacrylate) (PMMA, M_w = ~120,000, CAS# 9011-14-7) and polystyrene (PS, M_w

= 192,000, CAS# 9003-53-6) were purchased from Sigma-Aldrich (St. Louis, MO) and prepared in anhydrous toluene (assay 99.8%, CAS# 108-88-3, Fisher Chemical Pittsburgh, PA) at concentrations of 0.10005 and 0.1030 g ml^{-1} of PMMA and 0.0255, 0.0785, 0.0814, and 0.0926 g ml^{-1} of PS. Poly(4-vinylphenol) (PVPh, M_w = ~11,000, CAS# 24979-70-2) purchased from Sigma-Aldrich (St. Louis, MO) was prepared in 200 proof ethanol at concentrations of 0.08997 and 0.1119 g ml^{-1}. All the waveguide films were then prepared by spin coating 200 µL of the PMMA, PS, and PVPh solutions on separate gold-coated sapphire disks at 3000 rpm for one minute using a KW-4A spin coater (Chemat Technology, Inc. Northbridge, CA). A 0.0255 g ml^{-1} PS solution was spin-coated on top of ~400 nm silica waveguide film after data were collected for the bare silica film. The polymer waveguides were left to dry overnight in ambient conditions to make certain the solvent was completely evaporated.

Ellipsometry Thickness Measurements

The thickness of nine waveguide films was measured using a spectroscopic ellipsometer (J. A. Woollam α-SE, J. A. Woollam Co. Inc., Lincoln, NE, USA) operating in the wavelength range of 380-900 nm at 65°, 70° and 75° angles of incidence with a 10 second data acquisition rate. The measured psi (Ψ) and delta (Δ) parameters were fit to multilayer film models using the CompleteEase^{TM} software package. The refractive index η and absorption coefficient k of the gold substrate were first determined using a two-phase air/gold substrate model. The thicknesses of the silica and polymer films were then determined by fitting ellipsometry data to three- and four-layer air/waveguide/gold substrate models. Measurements were taken at five different locations on the samples and an average thickness and standard deviation of the waveguide films were computed (Table 1). Subsequently, the refractive index of a bulk poly(4-vinylphenol) film was determined at 785 nm (i.e., the excitation wavelength of the near-infrared laser used to collect the experimental data) by ellipsometry.

Table 1. Thicknesses of the indicated waveguide dielectric samples.

concentration (g mL^{-1})	**ellipsometry thickness (nm)^b**
SiO_2	354 ± 1
SiO_2 : 0.0255 PS [a]	354 ± 1 : 100 ± 10
0.0900 PVPh	404 ± 2
0.1001 PMMA	411 ± 5
0.1119 PVPh	496 ± 3
0.1030 PMMA	516 ± 3
0.0785 PS	543 ± 1
0.0814 PS	602 ± 8
0.0926 PS	717 ± 2

[a] The waveguide sample consists of polystyrene on top of a SiO_2 waveguide substrate (SiO_2 : PS).
[b] The uncertainties represent the standard deviations from five different locations on the sample.

Waveguide-coupled SPP Cone Measurements

In the Kretschmann configuration (Figure 1), the gold film was coated on a sapphire substrate and optically coupled to a sapphire Weierstrass-type prism (ISP Optics Irvington, NY) with a $\eta = 1.7400$ (at the sodium D line) index matching fluid solution (Cargille Laboratories Inc., Cedar Grove, NJ). The sample holder designed to secure the prism and the gold substrate was placed on a previously described instrument [1]. In the reverse-Kretschmann configuration (Figure 2), the laser was directed perpendicular to the sample from the front side. A digital image of the entire SPP cone was acquired with a 75 mm (*f*/1.3) Kameratori TV Lens (Tampere, Finland) attached to a 11.340 mm × 7.130 mm, 2.32 mega pixel CMOS sensor (IDS Imaging Development Systems GmbH, Obersulm, Germany) [1]. The SPP cone was acquired with both p- and s-polarized illumination. A near-infrared polarizer was used to further enhance the linearly polarized laser and a half-waveplate was used to switch between p- and s-polarized light. Translational mirrors were controlled by software integrated with a stepper motor used to scan the incident angle from 0.00° to 65.00° with 0.06° angle resolution. The experimental waveguide-coupled SPP cone diameter was determined from a CMOS calibration image of a ruler placed between the Weierstrass prism and the collection lens (Figure S1). Three to five waveguide-coupled SPP cone images were acquired for the same polymer waveguide sample to determine a cone angle average and standard deviation.

Waveguide-coupled Directional Raman Measurements

In the Kretschmann configuration, directional Raman scattering was measured as a function of incident angle with p- and s-polarized 200 mW 785-nm light. The spectra were acquired with either 30 or 60 s acquisitions for three accumulations at the angle that produced the most intense SPP cone intensity. Three replicate measurements were obtained for each sample. All spectra were collected at room temperature.

Simulation of the Electric Field Intensity Distribution Around the Waveguide-coupled Directional-surface-plasmon-polariton Cones

Data were modeled using standard optical calculations [30, 35]. Three-dimensional finite-difference-time-domain (FDTD) simulations (EM Explorer, San Francisco, CA) were used to calculate the angular intensity pattern around the cone by looping over alpha (α) while computing the scattered field in planes orientated in different radial directions (Figure 3). The angle α was scanned between 0° to 360° with 3° resolution at an excitation wavelength of 785 nm. The base interface included a sapphire prism ($\eta = 1.7619$) [36], gold film ($\eta = 0.1431$, $k = 4.799$) [37], waveguide, and air ($\eta = 1.000$) [38]. The thicknesses of the prism and air layers were semi-infinite compared to the waveguide (≥ 300 nm) and the gold (50 nm) layers. The dielectric waveguide materials were: silica ($\eta = 1.454$) [39], poly(methyl methacrylate) ($\eta =$

1.48452) [40], polystyrene (η = 1.57826) [41], or poly(4-vinylphenol) (η = 1.560, determined at 785 nm using ellipsometry and a 1-micron thick film) of varying thicknesses (Table 1).

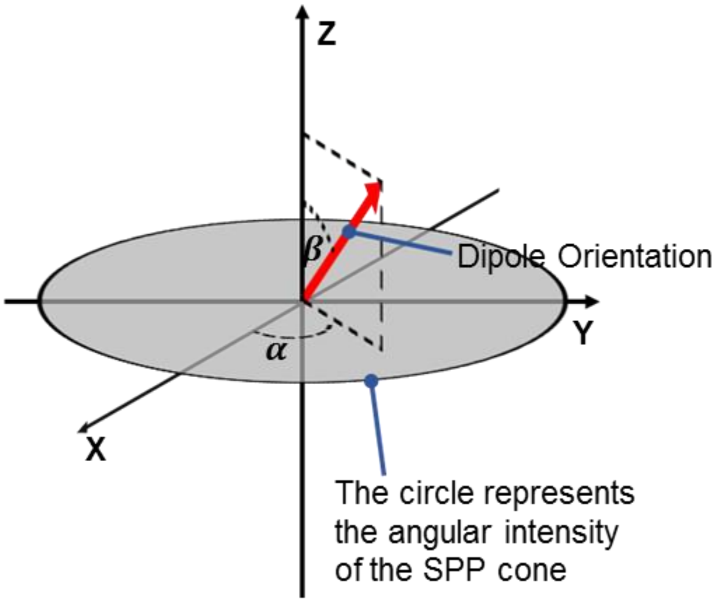

Figure 3. The angular intensity of the SPP cone is the intensity of light as α is rotated from 0° to 360°. The parameter β describes the orientation of the dipole producing the signal.

The simulation tool was designed for periodic boundary conditions in the lateral direction and the calculations assumed all layers were homogenous. A 25-nm Yee cell size was used in the simulation to obtain high resolution calculations at a reasonable simulation time using a 64-bit operating system with an Intel (R) Core ™ i7-4770 processor (CPU @ 3.40 GHz). The total number of cycles for computation was set to 100. A scattering dipole was placed at the center of the waveguide layer between the gold and air layers (Figure S2). The scattering dipole was expressed as plane waves in the EM Explorer finite-difference-time-domain simulation script (included in the Supporting Information) and its radiation wavelength was λ = 785 nm. The orientation of the scattering dipole was given by the beta (β) parameter (Figure 3). For p-polarized excitation, β = 90°, respectively. The *calculated* waveguide-coupled SPP cone diameter was determined using the SPP cone angle obtained from the simulations and the inverse-tangent of the distance between the prism (i.e., sample interface) and detector. A Python (v3.6) script with Matplotlib plotting library was implemented to plot a 2D representation of the log of the angular electric field intensity around the concentric cones as a function of cone angle.

Results and Discussion

Quantification and Modeling of the Waveguide-coupled SPP Cones with Reverse-Kretschmann Raman Illumination

The experimentally measured and calculated waveguide-coupled SPP cones for a 354 ± 1 nm silica over 50-nm Au film are shown in Figure 4A. Three concentric SPP cones are observed. The spacing between the cones when comparing the experimental and calculated data do not always match. This discrepancy is the result of the optics used to image the cones, which can cause image compression, particularly at large cone angles (i.e., the outer cones). The image compression is compensated for as described in Figure S1, and the angle at which each SPP cone is generated is determined. The experimentally measured cone angle is matched with the calculated angles to assign a waveguide mode to each cone (Table 2). The inner cone corresponds to waveguide mode 0 for p-polarized light ($m_p = 0$), the middle cone corresponds to waveguide mode 0 for s-polarized light ($m_s = 0$), and the outer cone corresponds to the SPR mode. As expected, the SPP cone image is rotated by 90° when the incident light is switched from p- to s-polarization (Figure 4A). Figure 4B illustrates the relationship between the polarization of the incident light, the polarization of the waveguide mode, and the resulting angular intensity pattern of the SPP cone. When the polarization of the waveguide mode matches the polarization of the excitation source, the areas of maximum SPP cone intensity are in the horizontal plane using this experimental setup. In contrast, when the polarization of the waveguide modes is orthogonal to the polarization of the excitation source, the maximum cone intensity is measured in the vertical plane.

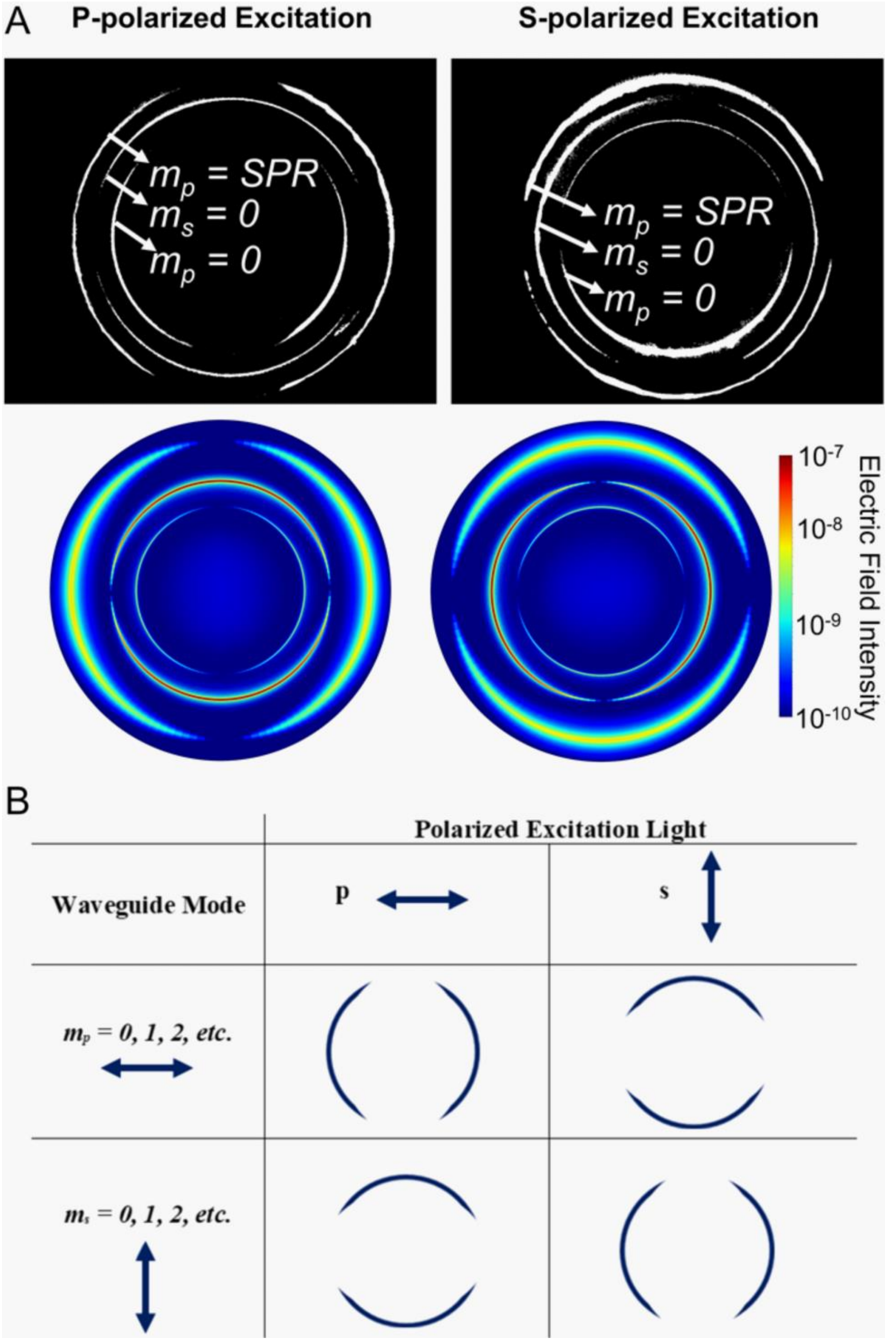

Figure 4. Experimentally measured (black/white scale) and calculated (color scale, shown in a logarithmic base 10 scale) waveguide-coupled SPP cones for a 354 ± 1 nm SiO_2 waveguide sample acquired in the reverse-Kretschmann configuration with (left) p- and (right) s-polarized incident light. The cone angles for the three waveguide modes are listed in Table 2. (B) Schematic showing the relationship between the waveguide mode assignment, the polarization of the excitation source, and the resulting angular intensity pattern in the reverse-Kretschmann configuration.

After coating a 100 ± 10 nm polystyrene film onto the 354 ± 1 nm silica waveguide substrate (SiO_2 : PS), two waveguide modes ($m_p = 0$, $m_s = 0$) and one SPR mode ($m_p = SPR$) are still observed. All the modes, however, appear at larger cone angles compared to the bare silica waveguide (Table 2 and Figure S3). The waveguide-coupled SPP cone properties in the reverse-Kretschmann configuration were further tested using seven polymer waveguides with thicknesses ranging from ~400 to 720 nm. Three different polymers were used to make the waveguides, including: polystyrene (index of refraction at 785 nm, $\eta = 1.57826$), poly(4-vinylphenol) ($\eta = 1.560$), and poly(methyl methacrylate) ($\eta = 1.48452$). Images of the SPP cones using p-polarized incident light are shown in Figure 5 and using s-polarized incident light in Figure S4. In this instrumental configuration, the setup allows cone angles in the range of ~30° to ~50° to be measured. SPP cones outside this range (i.e., the SPR modes for the 411 ± 5 nm and 516 ± 3 nm poly(methyl methacrylate) waveguide samples) cannot be measured with existing instrumentation due to the limiting aperture of the collection lens.

Table 2. Measured and calculated waveguide-coupled SPP cone angles (θ_{cone}) with illumination in the reverse-Kretschmann configuration.

ellipsometry thickness (nm)	$m_{polarization}$[a]	**experimental θ_{cone} (°)** [b]	**calculated θ_{cone} (°)**
354 ± 1 SiO_2	$m_p = 0$	32.15 ± 0.04	32.15
	$m_s = 0$	39.7 ± 0.2	39.90
	$m_p = SPR$	45.7 ± 0.2	45.80
354 ± 1 SiO_2 : 100 ± 10 PS	$m_p = 0$	35.36 ± 0.07	35.39
	$m_s = 0$	41.74 ± 0.02	41.72
	$m_p = SPR$	49.01 ± 0.03	49.04

[a] The waveguide mode assignment is designated $m_{polarization}$, where the polarization is either p- or s-polarized; *SPR* = surface plasmon resonance.

[b] The uncertainties represent the standard deviation of the cone angles from the SPP cone images acquired with p- and s-polarized light.

Both the thickness and the index of refraction of the waveguide affect the waveguide-coupled SPP cone properties. There is an increase in the number of waveguide-coupled SPP cones with increasing polymer thickness [20], with four cones measured for the thickest 717 ± 2 nm polystyrene waveguide. The $m_p = 1$ cone (i.e., the innermost cone denoted by dashed line) for the 602 ± 8 nm polystyrene waveguide film does not show well in the calculated results, but is measured experimentally. This polymer thickness is at the cusp of supporting waveguide mode $m_p = 1$, and as a result a small uncertainty in the waveguide thickness can affect whether the mode appears in the calculated results.

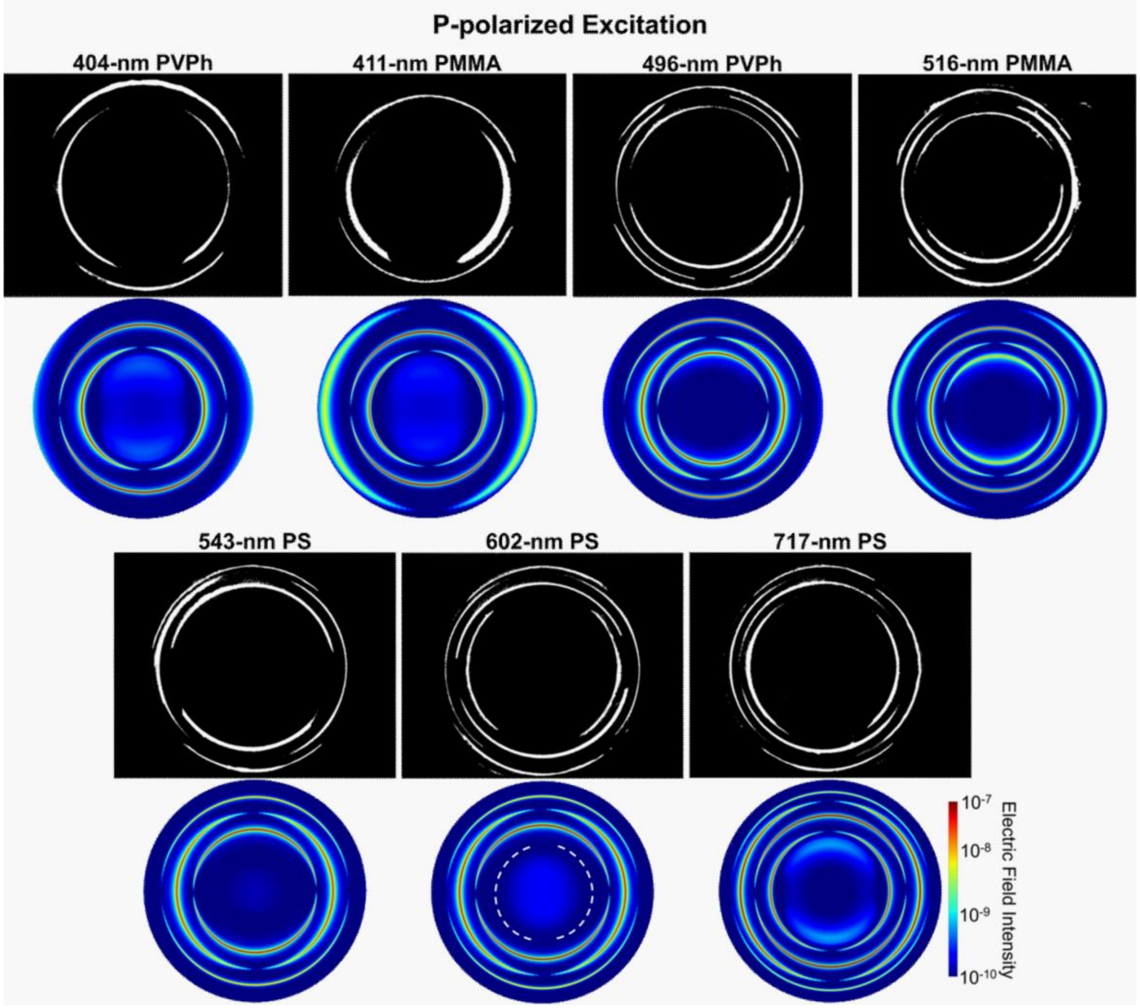

Figure 5. Experimentally measured (black/white scale) and calculated (color scale, shown in a logarithmic base 10 scale) waveguide-coupled SPP cones showing the angular intensity patterns

for 404 ± 2 nm poly(4-vinylphenol) (PVPh), 411 ± 5 nm poly(methyl methacrylate) (PMMA), 496 ± 3 nm PVPh, 516 ± 3 nm PMMA, 543 ± 1 nm polystyrene (PS), 602 ± 8 nm PS and 717 ± 2 nm PS waveguide structures with reverse-Kretschmann p-polarized illumination. The experimental and calculated cone angles are listed in Table S1 and data using s-polarized incident light are shown in Figure S4. The inner cone ($m_p = 1$) for the 602 ± 8 nm polystyrene waveguide is very faint in the calculated results on this color scale and is represented by the added dashed white lines.

Figure 6 shows the cone angles for all seven polymer waveguide films. When considering the same polymer material, the cone angle for a particular waveguide mode increases with increasing thickness (Figure 6 and Table S1). This is due to an increase in the refractive index of the layer adjacent to the metal film that alternates the wave vector of the surface plasmons [42]. The sensitivity is defined as the lowest change in the waveguide-coupled SPP cone angle per change in the polymer waveguide thickness and is reported as a ratio degrees nm^{-1}. The sensitivity is determined from the slope of the fit line for the individual waveguide modes in Figure 6. In the reverse-Kretschmann configuration, the sensitivity is 0.009° nm^{-1} for waveguide mode ($m_s = 0$), 0.02° nm^{-1} ($m_p = 0$), 0.03° nm^{-1} ($m_s = 1$) and 0.02° nm^{-1} ($m_p = 1$), respectively. Abbas et al. report a PWR sensitivity of 0.010° nm^{-1} using a 510-nm silica waveguide and a gold film with a scanning angle (i.e., reflectivity) measurement [43]. While not all experimental parameters are equal, this does show the sensitivity of the waveguide-coupled SPP cone measurement is similar to reported PWR experiments. Abbas et al. also report a higher sensitivity using a silver film, which would also be expected for the measurements of the waveguide-coupled SPP cone.

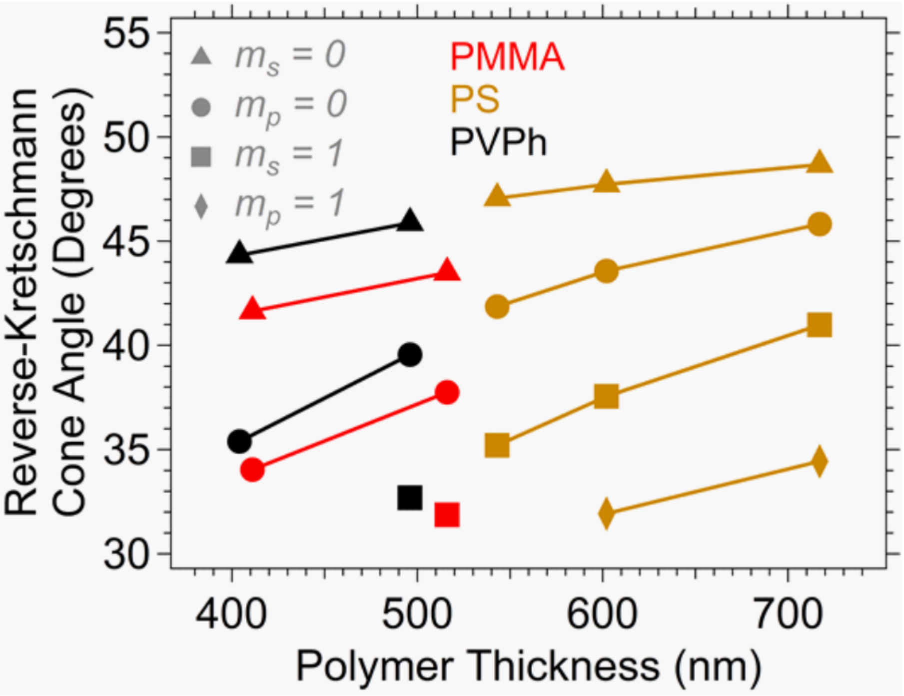

Figure 6. Plot of the reverse-Kretschmann cone angles as a function of polymer thickness for each waveguide mode represented by the symbols (▲) $m_s = 0$, (●) $m_p = 0$, (■) $m_s = 1$, and (♦) $m_p = 1$ generated from (red trace) PMMA, (gold trace) PS, and (black trace) PVPh. The experimental and calculated cone angles are listed in Table S1. The error bars representing the standard deviation of the cone angles are not visible on this scale (the average standard deviation is 0.04°).

Waveguide-coupled SPP Cone Angular Intensity Pattern and Directional Raman Scattering Measurements with Kretschmann Illumination

In the Kretschmann configuration, there are two relevant angles: the angle of incident light that produces the SPP cones (θ_{inc}) and the angle at which the SPP cones are projected (θ_{cone}). The incident angle is always larger than SPP cone angle. The incident angles at which the waveguide modes are generated correlate with the calculated attenuation of the reflected light (Figure 7). Both the incident and SPP cone angles are shifted to higher values when 100 ± 10 nm polystyrene is coated over the 354 ± 1 nm silica film, as expected. There is a wider incident angle range over which the SPP cones are measured compared to the calculated reflectivity, which is a result of a small angle spread in the incident angle. The sensitivity could be further improved by optimizing the instrument’s optics to generate a single incident angle, rather than the small range of incident angles that are currently produced.

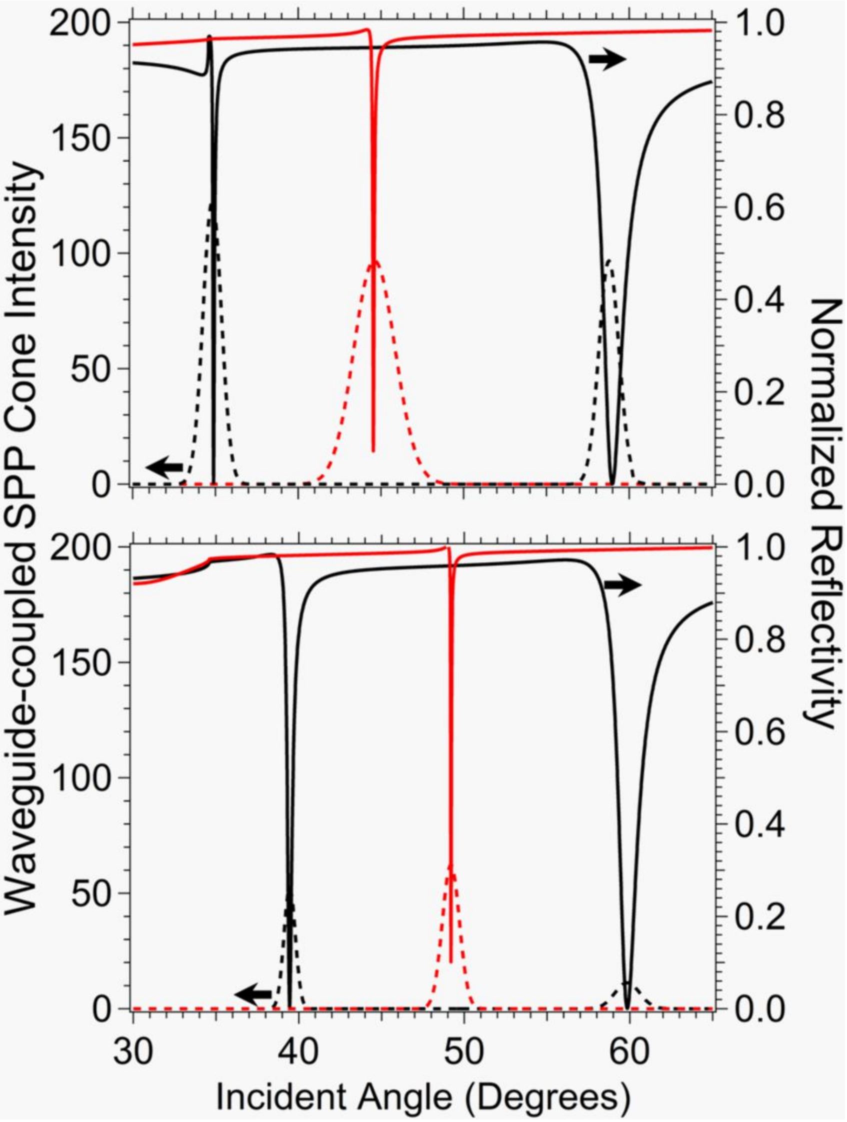

Figure 7. Experimentally measured waveguide-coupled SPP cone intensity acquired in the Kretschmann configuration (dotted line) and calculated Fresnel reflectivity (solid line) for (top) 354 ± 1 nm silica (SiO_2) and (bottom) 354 ± 1 nm SiO_2 : 100 ± 10 nm polystyrene (PS) waveguide films. The red and black curves correspond to s- and p-polarized incident light, respectively. The experimental/calculated incident angles (θ_{inc}) for the bare SiO_2 waveguide modes are: 34.80°/34.88° ($m_p = 0$); 44.58°/44.54° ($m_s = 0$); and 58.77°/58.98° ($m_p = SPR$). The experimental/calculated incident angles for the SiO_2 : PS waveguide modes are: 39.44°/39.42° ($m_p = 0$); 49.19°/49.19° ($m_s = 0$); and 59.79°/59.79° ($m_p = SPR$).

Images of the SPP cones were collected at every incident angle at which the reflected light intensity was maximally attenuated in the Kretschmann configuration (Table S2). The waveguide-coupled SPP cone image acquired at an incident angle of 34.80° (the incident angle associated with $m_p = 0$) for the 354 ± 1 nm silica waveguide is shown in Figure 8. As with reverse-Kretschmann illumination, multiple concentric SPP cones are observed. Since all the waveguide modes can be excited simultaneously with p- or s-polarized incident light at a single incident angle, this represents a simple new strategy for quantifying the properties of a waveguide, or adsorption to a waveguide, in the Kretschmann geometry. The presence of both scattered and reflected light from the through-prism illumination in the Kretschmann configuration (on the right and left of the image in Figure 8) make it difficult to measure the angular intensity pattern around the entire cone, particularly with the polymer waveguide samples. For this reason, the SPP cone intensities were only analyzed in the vertical direction where the background is minimized. The incident angles that produce SPP cones and the SPP cone angles have a linear dependence (Figure 9), which makes it straightforward to determine the optimum incident angle for data collection. Using the cones angles measured from an image acquired in the reverse-Kretschmann configuration, the incident angle of light that generates SPP cones in the Kretschmann configuration can be determined. This reduces the acquisition time for collecting PWR data in the Kretschmann configuration since there is no need to scan a large angle range to collect the SPP cones.

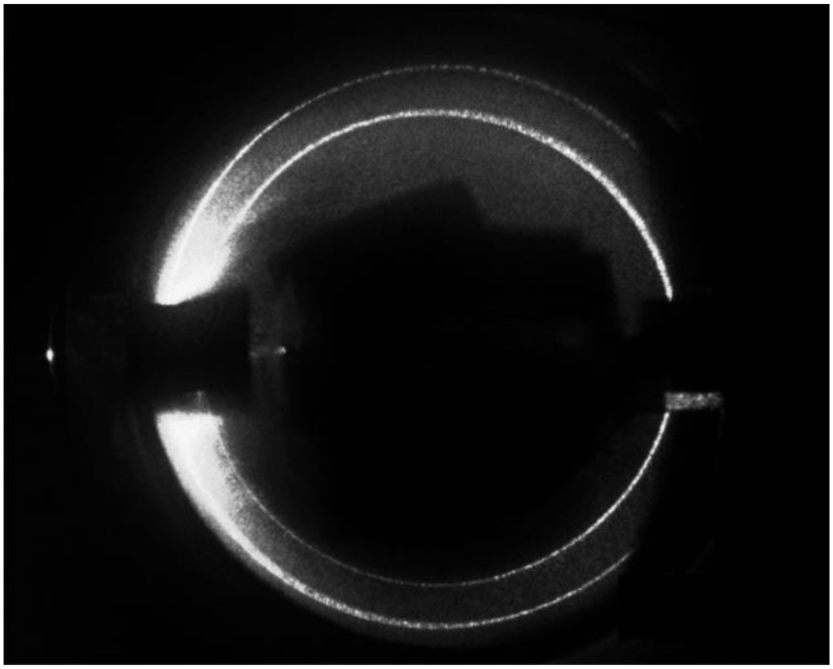

Figure 8. Waveguide-coupled SPP cone image acquired with p-polarized incident light directed at θ_{inc} = 34.80° ($m_p = 0$) in the Kretschmann configuration for the 354 ± 1 nm silica waveguide film. The inner and outer cones represent waveguide modes $m_p = 0$ and $m_s = 0$, respectively. The high background at the left of the image is from reflected and scattered light from the sapphire prism. The optics that direct the incident light (right) and block a majority of the reflected light (left) are observed in the image.

A comparison of the reverse-Kretschmann and Kretschmann cone angles is shown in Figure 10. There is a linear dependency for the cone angles acquired in both the Kretschmann-type configurations across all waveguide thicknesses, with an average deviation of 0.05° for all the data collected. This means the sensitivity (° nm^{-1}) is the same for both illumination geometries. A benefit of utilizing the Kretschmann configuration, which produces total internal reflection, is the ability to measure directional Raman signals from thin films with high signal-to-noise ratio spectra (Figure S5). This provides chemical information about the waveguide structure as well as the identity of the adsorbed species. None of the waveguide films produced detectable Raman signal with the reverse-Kretschmann illumination using the same instrument components. Furthermore, the advantages and disadvantages of the reverse-Kretschmann and Kretschmann illumination geometries are summarized in Table S3.

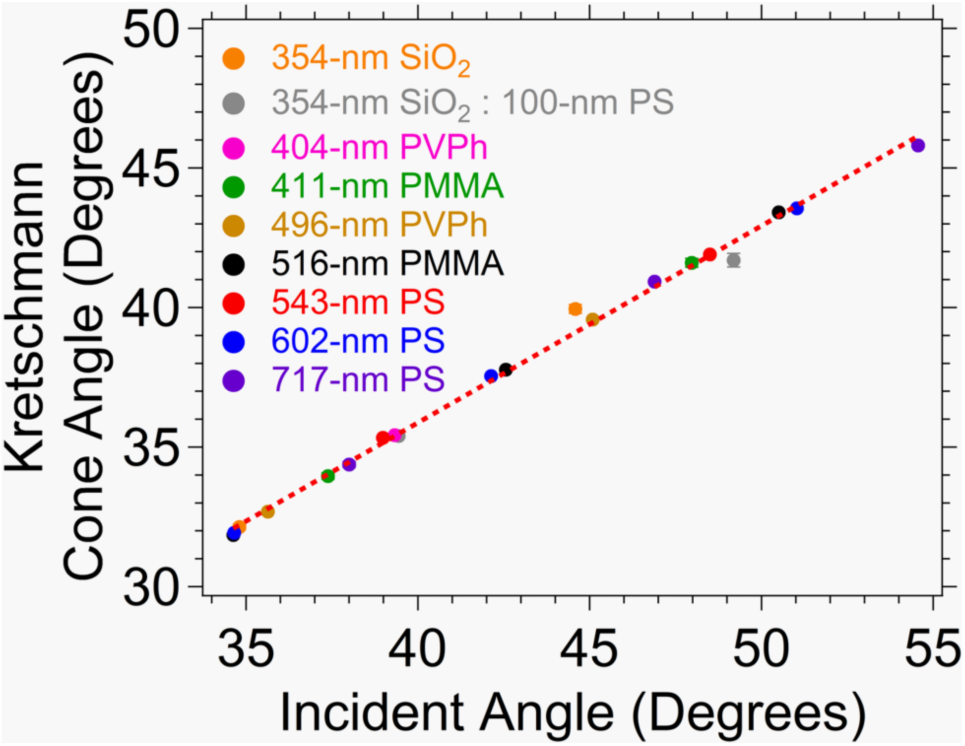

Figure 9. Experimental waveguide-coupled SPP cone angles measured in the Kretschmann configuration versus incident angle for all nine waveguide samples. The linear fit (dotted red trace) of the experimental data is [$y = 0.705x + 7.662$; $R^2 = 0.9958$]. The error bars representing the standard deviation of the SPP cone angles are not visible on this scale (the average standard deviation is 0.06°). Table S2 shows the values of the cone angles and incident angles of all nine waveguide films.

Conclusions

The data demonstrate a method for collecting PWR data using images of SPP cones from dielectric waveguide films on a noble metal surface in both the reverse-Kretschmann and Kretschmann configurations. Waveguide properties (e.g., thickness, index of refraction) can be determined from a single SPP cone image because all the waveguide modes are excited simultaneously and observed with p- or s-polarized light. Similarly, it will be straightforward to extend the presented work to measure adsorption on the waveguide surface. In the reverse

Kretschmann geometry, there is no need for additional optics to vary the incident angle of light, and the angular intensity pattern of the cones encodes information about polarization of the various modes. In addition, the Kretschmann configuration enables sensitive spectral measurements, such as Raman scattering for example, since the illumination conditions produce total internal reflection and enhanced electric fields at the interface. Both illumination configurations have similar sensitivities that parallel those reported in the literature for scanning angle PWR measurements, but require no moving parts to collect. Measurements of waveguide-coupled SPP cones will enable the study of morphology, composition and chemical structure for thin films, such as those found in optoelectronics, sensing devices, and in separations.

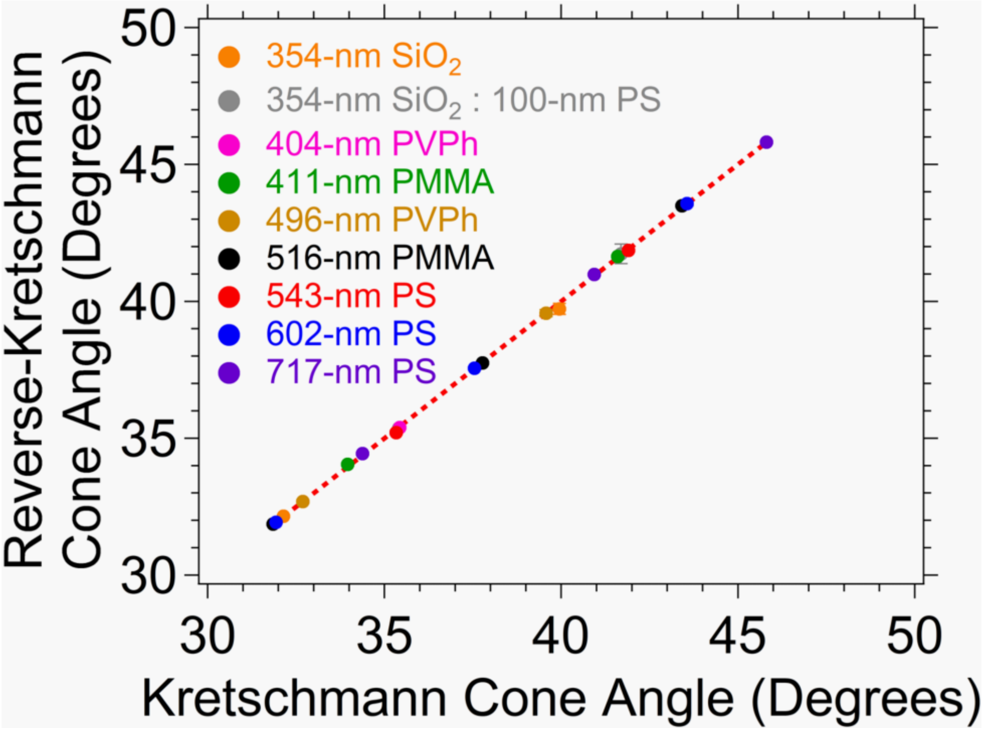

Figure 10. Plot of the experimental SPP cone angles measured in the reverse-Kretschmann configuration versus the Kretschmann SPP cone angles for all the waveguide dielectric structures. The linear fit (dotted red trace) of the experimental data is [$y = 1.001x – 0.027$; $R^2 = 0.9997$]. The error bars represent standard deviations of the SPP cone angles obtained in the two Kretschmann-type configurations and are not visible on this scale.

Acknowledgements

This research was supported by the U.S. Department of Energy, Office of Science, Basic Energy Sciences, Chemical Sciences, Geosciences, and Biosciences Division. The research was performed at the Ames Laboratory, which is operated for the U.S. DOE by Iowa State University under contract # DE-AC02-07CH11358.

References

[1] C.K.A. Nyamekye, S.C. Weibel, J.M. Bobbitt, E.A. Smith, Combined measurement of directional Raman scattering and surface-plasmon-polariton cone from adsorbates on smooth planar gold surfaces, Analyst 143 (2018) 400-408.

[2] M. Futamata, P. Borthen, J. Thomassen, D. Schumacher, A. Otto, Application of an ATR Method in Raman Spectroscopy, Appl. Spectrosc. 48 (1994) 252-260.

[3] M. Futamata, Surface-Plasmon-Polariton-Enhanced Raman Scattering from Self-Assembled Monolayers of p-Nitrothiophenol and p-Aminothiophenol on Silver, J. Phys. Chem. 99 (1995) 11901-11908.

[4] M. Futamata, E. Keim, A. Bruckbauer, D. Schumacher, A. Otto, Enhanced Raman scattering from copper phthalocyanine on Pt by use of a Weierstrass prism, Appl. Surf. Sci, 100 (1996) 60-63.

[5] S.-X. Huo, Q. Liu, S.-H. Cao, W.-P. Cai, L.-Y. Meng, K.-X. Xie, Y.-Y. Zhai, C. Zong, Z.-L. Yang, B. Ren, Y.-Q. Li, Surface Plasmon-Coupled Directional Enhanced Raman Scattering by Means of the Reverse Kretschmann Configuration, J. Phys. Chem. Lett. 6 (2015) 2015-2019.

[6] M. Futamata, Surface Plasmon Polariton Enhanced Raman Scattering from Adsorbates on a "Smooth" Metal Surface: The Effect of Thickness and Dielectric Properties of Constituents, Langmuir 11 (1995) 3894-3901.

[7] S. Byahut, T.E. Furtak, A device for performing surface-plasmon-polariton-assisted Raman scattering from adsorbates on single-crystal silver surfaces, Rev. Sci. Instrum. 61 (1990) 27-32.

[8] H. Li, S. Xu, Y. Liu, Y. Gu, W. Xu, Directional emission of surface-enhanced Raman scattering based on a planar-film plasmonic antenna, Thin Solid Films, 520 (2012) 6001-6006.

[9] X.-m. Wan, R. Gao, D.-f. Lu, Z.-m. Qi, Self-referenced directional enhanced Raman scattering using plasmon waveguide resonance for surface and bulk sensing, Appl. Phys. Lett. 112 (2018) 041906.

[10] S.A. Meyer, E.C. Le Ru, P.G. Etchegoin, Combining Surface Plasmon Resonance (SPR) Spectroscopy with Surface-Enhanced Raman Scattering (SERS), Anal. Chem. 83 (2011) 2337-2344.

[11] H. Wang, H. Li, S. Xu, B. Zhao, W. Xu, Integrated plasmon-enhanced Raman scattering (iPERS) spectroscopy, Sci. Rep., 7 (2017) 14630.

[12] Y.-F.C. Chau, C.-T. Chou Chao, C.M. Lim, H.J. Huang, H.-P. Chiang, Depolying Tunable Metal-Shell/Dielectric Core Nanorod Arrays as the Virtually Perfect Absorber in the Near-Infrared Regime, ACS Omega 3 (2018) 7508-7516.

[13] Y.-F.C. Chau, C.-K. Wang, L. Shen, C.M. Lim, H.-P. Chiang, C.-T.C. Chao, H.J. Huang, C.-T. Lin, N.T.R.N. Kumara, N.Y. Voo, Simultaneous realization of high sensing sensitivity and tunability in plasmonic nanostructures arrays, Sci. Rep., 7 (2017) 16817.

[14] Z. Salamon, G. Tollin, Optical Anisotropy in Lipid Bilayer Membranes: Coupled Plasmon-Waveguide Resonance Measurements of Molecular Orientation, Polarizability, and Shape, Biophys. J. 80 (2001) 1557-1567.

[15] G. Tollin, Z. Salamon, V.J. Hruby, Techniques: Plasmon-waveguide resonance (PWR) spectroscopy as a tool to study ligand–GPCR interactions, Trends Pharmacol. Sci. 24 (2003) 655-659.

[16] Z. Salamon, H.A. Macleod, G. Tollin, Coupled plasmon-waveguide resonators: a new spectroscopic tool for probing proteolipid film structure and properties, Biophys. J., 73 (1997) 2791-2797.

[17] C. Yuan-Fong Chou, L. Chuanyo, H. Hung Ji, L. Chun-Ting, C. Hai Pang, M. Abdul Hanif, V. Nyuk Yoong, L. Chee Ming, Plasmonic effects arising from a grooved surface of a gold nanorod, J. Phys. D: Appl. Phys. 50 (2017) 125302.

[18] A.J. Braundmeier, H.E. Tomaschke, Observation of the simultaneous emission of roughness-coupled and optical-coupled surface plasmon radiation from silver, Opt. Commun. 14 (1975) 99-103.

[19] H.J. Simon, J.K. Guha, Directional surface plasmon scattering from silver films, Opt. Commun. 18 (1976) 391-394.

[20] M.W. Meyer, K.J. McKee, V.H.T. Nguyen, E.A. Smith, Scanning Angle Plasmon Waveguide Resonance Raman Spectroscopy for the Analysis of Thin Polystyrene Films, J. Phys. Chem. C 116 (2012) 24987-24992.

[21] K.J. McKee, M.W. Meyer, E.A. Smith, Plasmon Waveguide Resonance Raman Spectroscopy, Anal. Chem. 84 (2012) 9049-9055.

[22] B.J. M., S.E. A., Extracting interface locations in multilayer polymer waveguide films using scanning angle Raman spectroscopy, J. Raman Spectrosc. 49 (2018) 262-270.

[23] Z. Salamon, M.F. Brown, G. Tollin, Plasmon resonance spectroscopy: probing molecular interactions within membranes, Trends Biochem. Sci. 24 (1999) 213-219.

[24] Z. Salamon, G. Tollin, Plasmon resonance spectroscopy: probing molecular interactions at surfaces and interfaces, Spectrosc. 15 (2001).

[25] I. Gryczynski, J. Malicka, Z. Gryczynski, J.R. Lakowicz, Radiative decay engineering 4. Experimental studies of surface plasmon-coupled directional emission, Anal. Biochem. 324 (2004) 170-182.

[26] I. Gryczynski, J. Malicka, Z. Gryczynski, K. Nowaczyk, J.R. Lakowicz, Surface plasmon-coupled directional fluorescence emission, Proc. SPIE 5327 (2004) 37-44.

[27] J.R. Lakowicz, Radiative decay engineering 3. Surface plasmon-coupled directional emission, Anal. Biochem. 324 (2004) 153-169.

[28] I. Gryczynski, J. Malicka, K. Nowaczyk, Z. Gryczynski, J.R. Lakowicz, Effects of Sample Thickness on the Optical Properties of Surface Plasmon-Coupled Emission, J. Phys. Chem. B 108 (2004) 12073-12083.

[29] I. Gryczynski, J. Malicka, K. Nowaczyk, Z. Gryczynski, J.R. Lakowicz, Waveguide-modulated surface plasmon-coupled emission of Nile blue in poly(vinyl alcohol) thin films, Thin Solid Films 510 (2006) 15-20.

[30] N. Calander, Surface Plasmon-Coupled Emission and Fabry−Perot Resonance in the Sample Layer: A Theoretical Approach, J. Phys. Chem. B 109 (2005) 13957-13963.

[31] C. Chen, J.-Y. Li, L. Wang, D.-F. Lu, Z.-M. Qi, Waveguide-coupled directional Raman radiation for surface analysis, Phys. Chem. Chem. Phys. 17 (2015) 21278-21287.

[32] C. Chen, D.-F. Lu, R. Gao, Z.-M. Qi, Analysis of waveguide-coupled directional emission for efficient collection of Fluorescence/Raman light from surface, Opt. Commun. 367 (2016) 86-94.

[33] J.R. Lakowicz, J. Malicka, I. Gryczynski, Z. Gryczynski, Directional surface plasmon-coupled emission: a new method for high sensitivity detection, Biochem. Biophys. Res. Commun. 307 (2003) 435-439.

[34] J. Malicka, I. Gryczynski, Z. Gryczynski, J.R. Lakowicz, DNA Hybridization Using Surface Plasmon-Coupled Emission, Anal. Chem. 75 (2003) 6629-6633.

[35] N. Calander, Theory and Simulation of Surface Plasmon-Coupled Directional Emission from Fluorophores at Planar Structures, Anal. Chem. 76 (2004) 2168-2173.

[36] B. Michael, PROPERTIES OF CRYSTALS AND GLASSES, Handbook of Optics: Volume IV - Optical Properties of Materials, Nonlinear Optics, Quantum Optics, Third Edition, McGraw Hill Professional, Access Engineering 2010.

[37] P.B. Johnson, R.W. Christy, Optical Constants of the Noble Metals, Phys. Rev. B 6 (1972) 4370-4379.

[38] P.E. Ciddor, Refractive index of air: new equations for the visible and near infrared, Appl. Opt. 35 (1996) 1566-1573.

[39] I.H. Malitson, Interspecimen Comparison of the Refractive Index of Fused Silica*,†, J. Opt. Soc. Am. 55 (1965) 1205-1209.

[40] N. Sultanova, S. Kasarova, I. Nikolov, Dispersion Properties of Optical Polymers, 2009.

[41] S.N. Kasarova, N.G. Sultanova, C.D. Ivanov, I.D. Nikolov, Analysis of the dispersion of optical plastic materials, Opt. Mater. 29 (2007) 1481-1490.

[42] H. Raether, Surface plasmons on smooth and rough surfaces and on gratings, Springer 1988.

[43] A. Abbas, M.J. Linman, Q. Cheng, Sensitivity comparison of surface plasmon resonance and plasmon-waveguide resonance biosensors, Sens. Actuators, B 156 (2011) 169-175.

Supporting Information

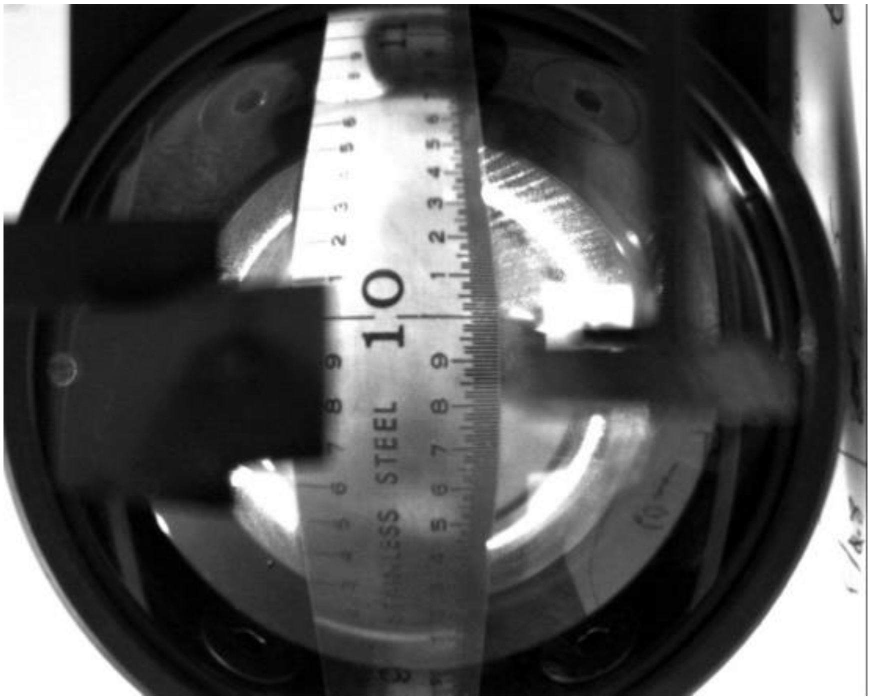

Figure S1. An image of the SPP cone for a gold film measured in the Kretschmann configuration with a metal ruler placed in the collection path. The lens compression of the SPP cone diameter is evident in the image. To correct for the compression, a calibration plot of pixel versus the ruler readings was generated. The plot was fit with a nonlinear cubic polynomial function [$y = (8.75\times10^{-9})x^3 - (6.99\times10^{-6})x^2 + 0.00697x - 0.0162$]. The Radial Profile Plot Java Script in Image-J 1.44p (National Institutes of Health, USA) was used to obtain the measured cone diameter of SPP cones, which was an input in the cubic polynomial equation to obtain the corrected diameter. The experimental SPP cone angle was calculated using the inverse-tangent of the distance between the prism (i.e., sample interface) and detector as well as the corrected radius of the SPP cone. The translation mirrors used to block the incident light and the reflected light from reaching the detector appear on the left and right side of the image. In contrast to data shown in other figures, the room lights were on when this image was collected.

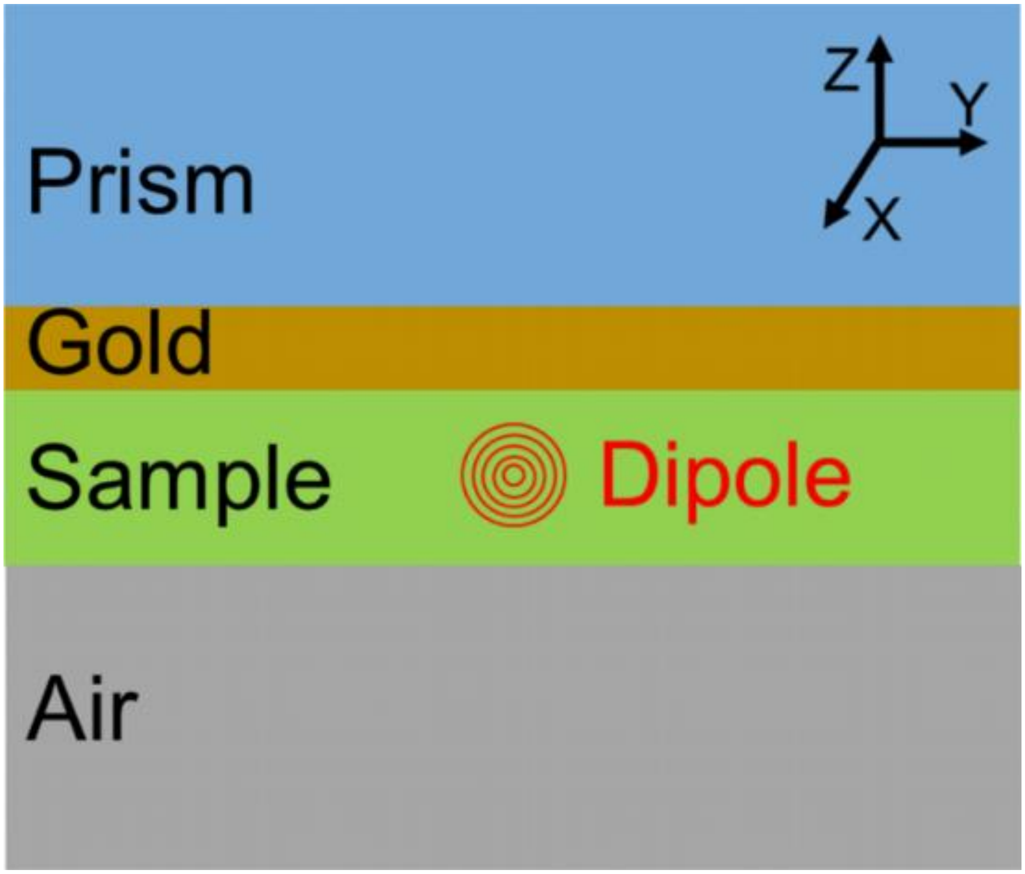

Figure S2. Schematic of the simulation layout with a planar structure and a dipole located in the middle of the sample (i.e., dielectric waveguide) layer. Schematic is not drawn to scale. The EM Explorer finite-difference-time-domain simulation script used to calculate the angular intensity pattern around the cone can be found at the end of Supporting Information.

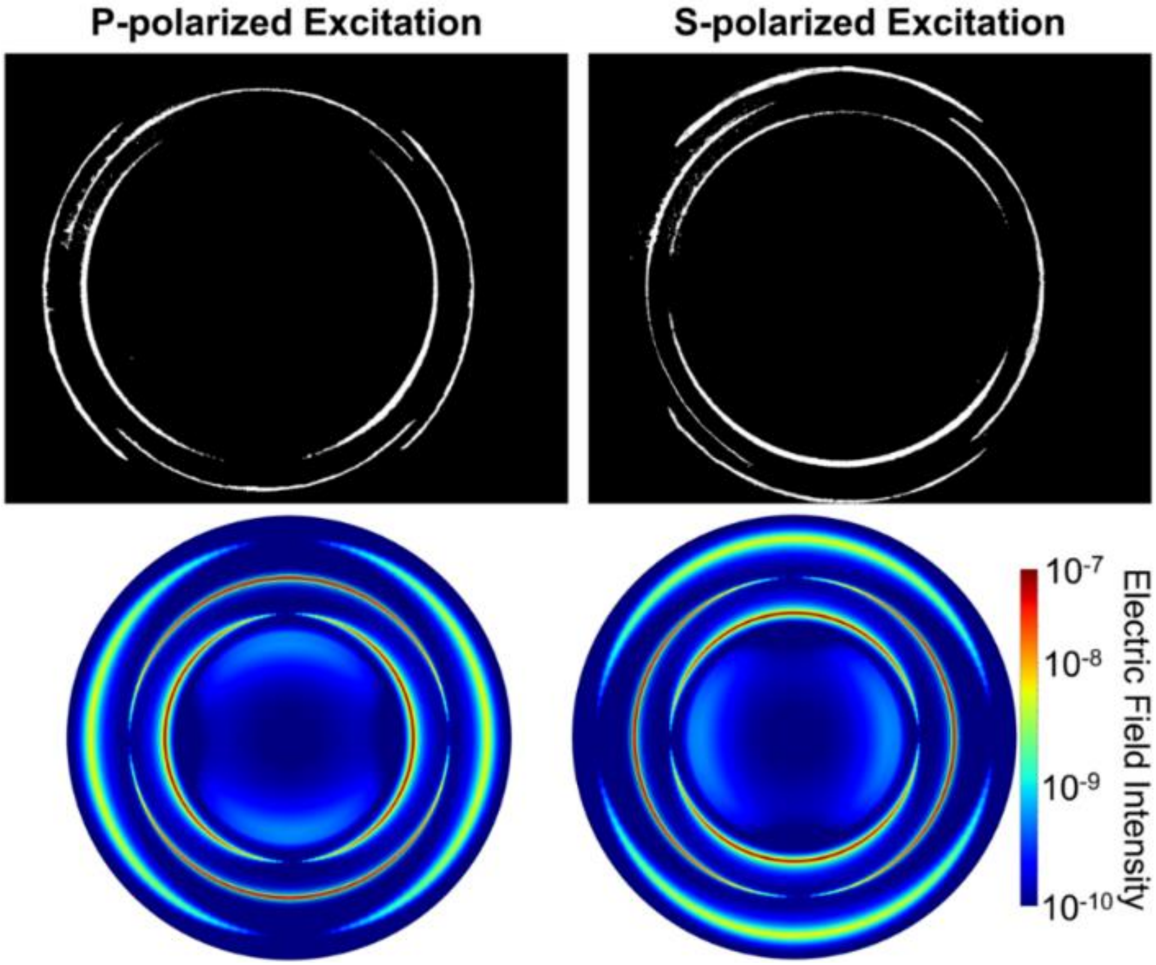

Figure S3. Experimental and calculated waveguide-coupled SPP cones for 354 ± 1 SiO_2 : 100 ± 10 PS waveguide sample acquired in the reverse-Kretschmann configuration with (left) p- and (right) s-polarized incident light. The calculated angular intensity plot is represented as a logarithmic base 10 scale. The inner, middle, and outer cones represent waveguide modes $m_p = 0$, $m_s = 0$, and $m_p = SPR$, respectively.

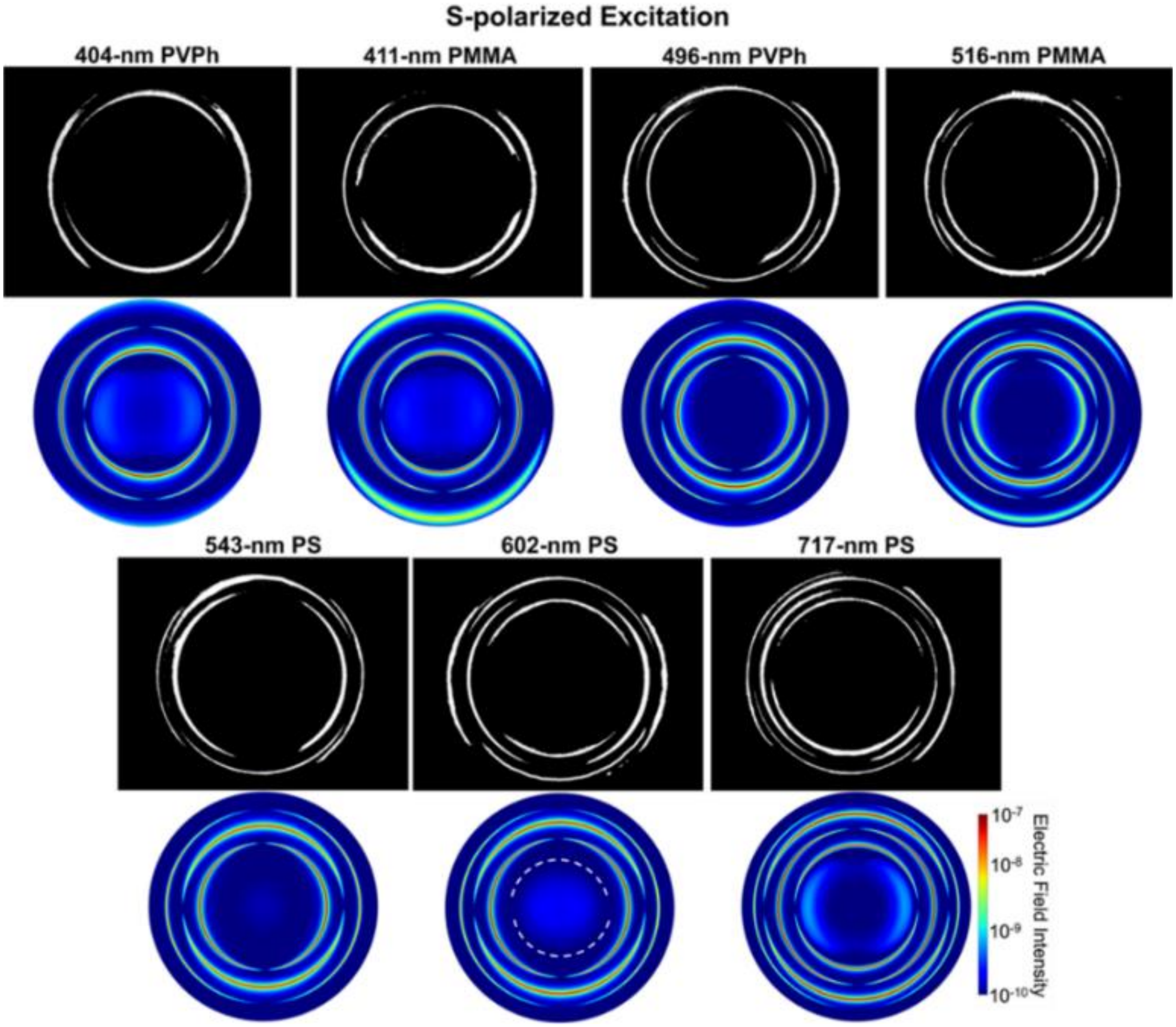

Figure S4. Experimentally measured (black/white scale) and calculated (color scale, shown in a logarithmic base 10 scale) waveguide-coupled SPP cones showing the angular intensity patterns for 404 ± 2 nm poly(4-vinylphenol) (PVPh), 411 ± 5 nm poly(methyl methacrylate) (PMMA), 496 ± 3 nm PVPh, 516 ± 3 nm PMMA, 543 ± 1 nm polystyrene (PS), 602 ± 8 nm PS and 717 ± 2 nm PS waveguide structures with reverse-Kretschmann s-polarized illumination. The missing inner cone is represented by the dashed white lines in the calculated angular intensity pattern for the 602 ± 8 nm PS waveguide (additional details in the legend for Figure 5).

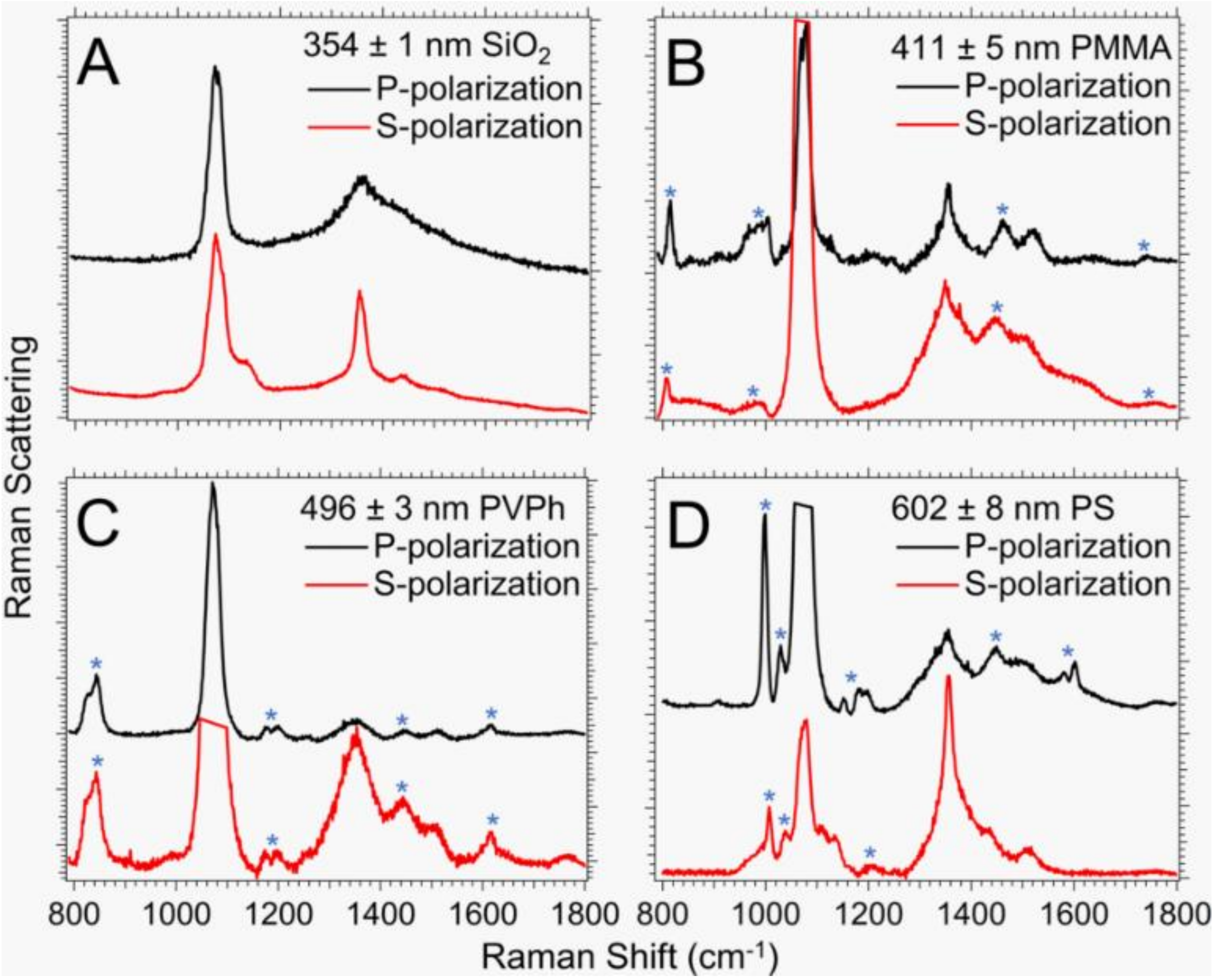

Figure S5. The waveguide-coupled directional Raman spectra of (A) 354 ± 1 nm SiO_2, (B) 411 ± 5 nm PMMA, (C) 496 ± 3 nm PVPh and (D) 602 ± 8 nm PS on a smooth planar gold film using (black) p- and (red) s-polarized 200-mW 785-nm incident light. The spectra were collected at the following incident angles corresponding to the listed waveguide mode: (A) 34.80° ($m_p = 0$) and 44.58° ($m_s = 0$); (B) 37.38° ($m_p = 0$) and 47.97° ($m_s = 0$); (C) 35.63° ($m_s = 1$) and 45.08° ($m_p = 0$) and (D) 34.65° ($m_p = 1$) and 42.14° ($m_s = 1$). The acquisition times were 60 s with 2 accumulations for collecting the Raman signal from the polymer waveguide films, except the s-polarized spectrum of SiO_2 and the p-polarized spectrum of PVPh, which were collected for 30 s with 2 accumulations. The asterisk (*) represents the Raman peaks of the polymer for clarity in distinguishing them from the background.

Table S1. Measured and calculated waveguide-coupled SPP cone angles for all the waveguide samples with illumination in the reverse-Kretschmann configuration.

ellipsometry thickness (nm)	$m_{Polarization}$ [a]	**experimental θ_{cone} (°)** [b]	**calculated θ_{cone} (°)**
404 ± 2 PVPh	$m_p = 0$	35.39 ± 0.05	35.39
	$m_s = 0$	44.327 ± 0.001	44.30
411 ± 5 PMMA	$m_p = 0$	34.04 ± 0.03	34.01
	$m_s = 0$	41.64 ± 0.03	41.68
	$m_p = SPR$	-	50.91
496 ± 3 PVPh	$m_s = 1$	32.689 ± 0.004	32.65
	$m_p = 0$	39.56 ± 0.06	39.56
	$m_s = 0$	45.88 ± 0.03	45.87
516 ± 3 PMMA	$m_s = 1$	31.867 ± 0.005	31.86
	$m_p = 0$	37.75 ± 0.02	37.76
	$m_s = 0$	43.49 ± 0.05	43.43
	$m_p = SPR$	-	49.94
543 ± 1 PS	$m_s = 1$	35.21 ± 0.07	35.20
	$m_p = 0$	41.86 ± 0.06	41.89
	$m_s = 0$	47.06 ± 0.05	47.07
602 ± 8 PS	$m_p = 1$	31.930 ± 0.002	31.93
	$m_s = 1$	37.56 ± 0.02	37.57
	$m_p = 0$	43.57 ± 0.08	43.54
	$m_s = 0$	47.73 ± 0.03	47.74
717 ± 2 PS	$m_p = 1$	34.44 ± 0.03	34.41
	$m_s = 1$	40.98 ± 0.03	40.97
	$m_p = 0$	45.82 ± 0.01	45.87
	$m_s = 0$	48.67 ± 0.07	48.65

[a] The waveguide mode assignment is designated $m_{polarization}$, where the polarization is either p or s polarized; *SPR* = surface plasmon resonance.

[b] The uncertainties represent the standard deviation of the cone angles from the SPP cone images acquired with p- and s-polarized light.

Table S2. Measured waveguide-coupled SPP cone properties and the calculated incident angle that produces surface plasmons with excitation in the Kretschmann configuration.

ellipsometry thickness (nm)	$m_{Polarization}$ [a]	**experimental θ_{inc} (°)**	**calculated θ_{inc} (°)**	**experimental θ_{cone} (°)**
354 ± 1 SiO_2	$m_p = 0$	34.80	34.884	32.11 39.79
	$m_s = 0$	44.58	44.541	32.25 40.11
	$m_p = SPR$	58.77	58.977	32.06 39.95
354 ± 1 SiO_2 : 100 ± 10 PS	$m_p = 0$	39.44	39.423	35.46 41.87
	$m_s = 0$	49.19	49.188	35.38 41.42
	$m_p = SPR$	59.79	59.79	35.36 41.79
404 ± 2 PVPh	$m_p = 0$	39.32	39.324	35.42
	$m_s = 0$	51.54	51.642	35.44
411 ± 5 PMMA	$m_p = 0$	37.38	37.380	33.98 41.77 -
	$m_s = 0$	47.97	47.973	33.84 41.56 -
	$m_p = SPR$	61.72	61.743	34.07 41.47 -
496 ± 3 PVPh	$m_s = 1$	35.63	35.631	32.69 36.51
	$m_p = 0$	45.08	45.099	32.69 39.61
	$m_s = 0$	54.30	54.297	32.69 -

Table S2. continued

ellipsometry thickness (nm)	$m_{Polarization}$ [a]	**experimental θ_{inc} (°)**	**calculated θ_{inc} (°)**	**experimental θ_{cone} (°)**
516 ± 3 PMMA	$m_s = 1$	34.63	34.626	31.87 37.76 43.46
	$m_p = 0$	42.56	42.555	31.87 37.76 43.47
	$m_s = 0$	50.50	50.574	31.82 37.81 43.37
	$m_p = SPR$	62.17	62.166	31.84 37.76 43.36
543 ± 1 PS	$m_s = 1$	38.98	38.988	35.34 41.90
	$m_p = 0$	48.50	48.510	35.31 41.90
	$m_s = 0$	56.39	56.394	35.34 41.90
602 ± 8 PS	$m_p = 1$	34.65	34.587	31.92 37.54 43.51
	$m_s = 1$	42.13	42.138	31.93 37.49 43.63
	$m_p = 0$	51.03	51.048	31.93 37.57 43.52
	$m_s = 0$	57.43	57.429	31.94 37.58 43.56

Table S2. continued

ellipsometry thickness (nm)	$m_{Polarization}$[a]	**experimental θ_{inc} (°)**	**calculated θ_{inc} (°)**	**experimental θ_{cone} (°)**
717 ± 2 PS	$m_p = 1$	38.00	38.007	34.50 40.92 45.87
	$m_s = 1$	46.89	46.89	34.40 40.93 45.82
	$m_p = 0$	54.56	54.576	34.35 40.94 45.81
	$m_s = 0$	58.91	58.905	34.26 40.94 45.73

[a] The waveguide mode assignment is designated $m_{polarization}$, where the polarization is either p or s polarized; *SPR* = surface plasmon resonance.

Table S3. Comparison of the reverse-Kretschmann and Kretschmann configurations.

Geometry Type	**Advantages**	**Disadvantages**
Reverse-Kretschmann	No need for optics to precisely vary the incident angle of light Angular intensity pattern around the cones encodes information about polarization of the various waveguide modes All the waveguide modes can be excited simultaneously with p- or s-polarized light	Raman scattering signal is smaller than measured in the Kretschmann configuration Film deterioration is possible due to laser exposure directly on the sample

Table S3. continued

Geometry Type	**Advantages**	**Disadvantages**
Kretschmann	Enables sensitive spectral measurements, such as Raman scattering, due to total internal reflection Polarized Raman spectra can provide structural information about the adsorbed molecules on the gold surface All the waveguide modes can be excited simultaneously with p- or s-polarized incident light at a single incident angle	Presence of both scattered and reflected light from the through-prism illumination must be blocked and may increase background No angular intensity pattern is observed around the cone, so assigning polarization to each cone is not straightforward

EM Explorer is a commercial software package for 3D Finite Difference Time Domain simulations. The EM Explorer script for the waveguide-coupled SPP cone angular distribution is provided below.

```
# Define wavelength in nm
set wavelength 785.0


# Define film thickness and Yee cell size in nm.
set T_Au 50.0
set dz [expr $T_Au/2.0]
set dx $dz
set dy $dz
set T_Poly 354.0
set T_Prism [expr 10.0*$dz]
set T_Air   [expr 20.0*$dz]
```

EM Explorer script. continued

```
# Define material’s indices of refraction n & k
set nPrism 1.7619
set kPrism 0.0

set nAir 1.0
set kAir 0.0

set nAu 0.1431
set kAu 4.7935

set nPoly 1.454
set kPoly 0.0

# Define simulation domain size
# Note, due to periodic boundary condition, a very large lx is used
# in this case in order to mimic an isolated dipole and to ensure
# a fine resolution in propagation angles of the field in prism
set lx [expr 10000.0*$dx]
set ly $dy
set lz [expr $T_Air+$T_Poly+$T_Au+$T_Prism]
# Define a list of films to be added to the simulation domain
set films [list \
```

EM Explorer script. continued

```
$T_Air $nAir $kAir \
$T_Poly $nPoly $kPoly \
$T_Au  $nAu  $kAu \
$T_Prism $nPrism $kPrism]

# loop over alpha (the angle between dipole polarization and simulation plane, i.e., x-z plane)
set beta 90.0
for {set alpha 0.0} {$alpha < 363.0} {set alpha [expr $alpha+3.0]} {

# Setup the simulation domain
emxp::grid lx=$lx ly=$ly lz=$lz dx=$dx dy=$dy dz=$dz n0=1.0 k0=0.0 check=true

# Add films to the simulation domain
set xc [expr 0.5*$lx]
set yc [expr 0.5*$ly]
set z 0.0
foreach {t n k} $films {
set zc [expr $z+0.5*$t]
set z [expr $z+$t]
emxp::solid shape=box xc=$xc yc=$yc zc=$zc xw=$lx yw=$ly zw=$t n=$n k=$k check=true
```

EM Explorer script. continued

```
}


# Add dipole excitation
set nx [emxp::query object=FDTD property=nx]
set ny [emxp::query object=FDTD property=ny]
set nz [emxp::query object=FDTD property=nz]
set isrc [expr $nx/2]
set zsrc [expr $T_Air-0.5*$dz]
set ksrc [expr int($zsrc/$dz)]
set PI 3.1415927
set ez [expr cos($beta*$PI/180.0)]
set er [expr sin($beta*$PI/180.0)]
set ex [expr $er*cos($alpha*$PI/180.0)]
set ey [expr $er*sin($alpha*$PI/180.0)]
puts "$isrc $ksrc"
for {set jsrc 0} {$jsrc <= $ny} {incr jsrc} {
emxp::excitation wavelength=$wavelength field=ex type=soft i=$isrc j=$jsrc k=$ksrc amplitude=$ex phase=0
emxp::excitation wavelength=$wavelength field=ey type=soft i=$isrc j=$jsrc k=$ksrc amplitude=$ey phase=0
emxp::excitation wavelength=$wavelength field=ez type=soft i=$isrc j=$jsrc k=$ksrc amplitude=$ez phase=0
```

EM Explorer script. continued

```
}
# Setup convergence monitor
emxp::convergence i=0 j=0 k=0 xo=$xc yo=$yc zo=$lz samples_per_cycle=1 sample_size=10 tolerance=0.0
#emxp::snapshot property=ez attribute=amplitude file=ez imin=0 imax=$nx jmin=0 jmax=$ny kmin=0 kmax=$nz

# Run simulation
emxp::run n_cycles=100

# Output near fields transmitted into the prism
emxp::scat_func property=ex attribute=amplitude file=t_ex_amp.vtk k=$nz ft=false
emxp::scat_func property=ey attribute=amplitude file=t_ey_amp.vtk k=$nz ft=false
emxp::scat_func property=ex attribute=phase file=t_ex_phz.vtk k=$nz ft=false
emxp::scat_func property=ey attribute=phase file=t_ey_phz.vtk k=$nz ft=false

set ID $alpha

# Write results to a file
set FILE [open data_dipole_${ID}.txt w]
puts $FILE "angle_in_prism E_sq_in_prism"
```

EM Explorer script. continued

```
emxp::nearfield object=file wavelength=$wavelength kx_inc=0 ky_inc=0 ex_amp=t_ex_amp.vtk ex_phz=t_ex_phz.vtk ey_amp=t_ey_amp.vtk ey_phz=t_ey_phz.vtk n0=$nPrism k0=0
for {set i 0} {$i < [expr $nx/2]} {incr i} {
set ex [emxp::query object=n2f property=ex_ft attribute=amplitude i=$i j=0]
set ey [emxp::query object=n2f property=ey_ft attribute=amplitude i=$i j=0]
set ez [emxp::query object=n2f property=ez_ft attribute=amplitude i=$i j=0]
set e_sq [expr $ex*$ex+$ey*$ey+$ez*$ez]
set a [expr $i*$wavelength/$lx/$nPrism]
if {$a > 1.0} {break}
set angle [expr asin($a)*180.0/$PI]
if {$angle > 90} {break}
puts $FILE "$angle $e_sq"
}
close $FILE

# Clean up
emxp::reset
}; # alpha loop
exit
```

CHAPTER 5. DIRECTIONAL RAMAN SCATTERING SPECTRA OF METAL-SULFUR BONDS AT SMOOTH GOLD AND SILVER SUBSTRATES

Charles K. A. Nyamekye[a,b], Stephen C. Weibel[c], Emily A. Smith[a,b *]

[a] Department of Chemistry, Iowa State University, Ames, Iowa 50011, United States

[b] U.S. Department of Energy, The Ames Laboratory, Ames, Iowa 50011, United States

[c] Surface Photonics Inc., Madison, Wisconsin 53719, United States

[*] Corresponding Author (esmith1@iastate.edu, 2415 Osborn Drive, Ames 50011; 1-515-294-1424)

Modified from a manuscript to be submitted to the Journal of Raman Spectroscopy

Abstract

The gold-sulfur (Au-S) and silver-sulfur (Ag-S) bonds are integral to the surface modification of metal films with alkanethiol monolayers. While the metal-sulfur bond can be characterized with surface-enhanced Raman spectroscopy (SERS) at roughened metal films, some applications require or perform better when using a smooth metal surface, which is not suitable for SERS signal enhancement. Directional-surface-plasmon-coupled Raman scattering (directional Raman scattering) is an approach to measure metal-sulfur bonds on smooth metal films with sub-monolayer sensitivity. The metal-sulfur bonds formed from a benzenethiol monolayer on smooth planar gold or silver films are observed in the directional Raman scattering spectra between 240 and 270 cm^{-1}; the signal-to-noise ratio of the Au-S Raman peak is 60. Importantly, the directional Raman scattering signal measured with smooth metal surfaces can be simply modeled and easily compared across many samples. Directional Raman scattering can also be measured at roughened metal films, which makes it applicable for many analyses.

Introduction

Self-assembled monolayers (SAMs) on noble metal surfaces are utilized in many fundamental and applied technologies. These include microelectronics containing surface patterning,[1-3] sensors made from proteins, lipids, DNA, and antibodies attached to a metal surface,[4] and multilayers of charged polymers adsorbed on a SAM-metal surface.[5,6] SAMs allow the functionality and stability of the metal surface to be tailored for many applications.

When monitoring the formation of SAMs on metal films, detecting the metal-sulfur bond is critical. While other vibrational modes assigned to the alkanethiol or aromatic thiols are often used to indicate the formation of a monolayer,[7,8] these signals are not necessarily indicative of the interaction between sulfur and the metal. Ulman[9] and Whitesides[10-12] showed that organosulfur compounds form SAMs on a gold surface by chemisorption of the sulfur head group to the metal substrate via the reaction:

$$R\!-\!S\!-\!H + Au^0{}_n \Rightarrow R\!-\!S^-Au^+\bullet Au^0{}_n + \frac{1}{2}H_2$$

where the thiol (S-H) bond is cleaved due to oxidation of a gold atom to form a Au-S bond. The hydrogen is released as gas or can combine with oxygen in solution and form water. A similar reaction can be envisioned for a monolayer adsorbed onto a silver film.[8] The properties of the SAM on the metal film are highly dependent on the properties of the metal surface. While detection of the metal-sulfur bond using surface-enhanced Raman spectroscopy (SERS) at roughened metal films is possible, for many applications it is desirable to characterize the SAM and monolayer formation via the metal-sulfur bond at smooth metal surfaces where SERS signal enhancement does not occur.

Vibrational spectroscopy is ideal for studying SAMs. The metal-sulfur bond produces a peak in the spectral region below 500 cm^{-1}; attenuated total reflection infrared (ATR-IR) spectroscopy may lack sensitivity in this region unless a diamond ATR element is used. Furthermore, most IR detectors lack the sensitivity in the spectral region below 500 cm^{-1}, with the exception of a liquid helium cooled bolometer, which is expensive and rarely used for routine ATR-IR measurements. There are many reports of Raman measurements on metal-sulfur interactions in this spectral region, mostly from utilizing SERS substrates, and therefore on a non-planar metal surface. Matulaitienė and coworkers experimentally measured the SERS signal from a synthesized N-(6-mercapto)hexylpyridinium chloride monolayer on roughened Au and Ag surfaces probed with 785-nm excitation.[13] They reported that the Au-S stretching vibrational band at 260 cm^{-1} correlates with the short Au-S bond length, while the low frequency Ag-S mode at 236 cm^{-1} results from a longer Ag-S bond length. The SERS spectra of the Au-S bond was also reported by Burgi et al.[14] from 2-phenylethylthiol and 1R,4S-camphorthiol monolayers on different sizes of gold clusters (producing a roughened metal surface) with a conventional backscattering geometry. It was revealed that the type of monolayer and the number of Au-S binding units on the gold clusters influenced the SERS spectra by shifting the Au-S band to higher frequencies as more gold clusters were introduced into the system.[14]

Computational work by Tlahuice-Flores et al. showed that the Au-S Raman vibrational region can span from 220 to 350 cm^{-1} due to radial and tangential Au-S vibrations.[15] Their density functional theory study showed two types of Au-S stretching vibrations due to movements of the thiolate against the metal surface (radial) and movements of the thiolates parallel to the metal surface (tangential). The tangential Au-S vibrational bond was weakly Raman active due to the longer and weaker Au-S bond compared to the radial Au-S vibrations, which yielded a shorter and stronger bond.[15] Density functional theory calculations using B3LYP functional and 6-31++G(d, p) basis set for C, H, N, and S atoms, and LANL2DZ with

ECP for Au and Ag atoms were performed by Niaura et al.[13] Their work confirmed that the Au-S stretching mode shifts to a higher frequency compared to the Ag-S band due to the shorter bond and stronger affinity between the gold surface and the sulfur headgroup of a N-(6-mercapto)hexylpyridinium chloride monolayer. To our knowledge, no experimental Raman study of the metal-sulfur bond of a SAM on smooth planar metallic substrates have been published. Sensitive methods that could be routinely implemented for measuring and characterizing the metal-sulfur bond at smooth interfaces would lead to a better understanding of the fundamental nature of the bonding interaction.

Directional Raman scattering is analogues to total internal reflection Raman spectroscopy using a smooth metal film (Figure 1). Surface-plasmon-**polaritons (SPPs)** are generated within the metal film when the excitation light is at an appropriate incident angle upon a prism of high refractive index traveling to an interface with a thin noble metal film and an adjacent dielectric material with a lower refractive index. An exponentially decaying evanescent wave is generated in the dielectric material that extends from a hundred nanometers to a couple of micrometers, depending on the excitation wavelength and the indices of refraction of the interfacial media.[16-19] Directional Raman scattering is produced by the excitation of surface plasmons in the plane of the metal film (in-coupling) and the emission of the scattered light through a Weierstrass prism (out-coupling) that results in a hollow cone of directional scattering at a sharply defined angle.[20,21] This is referred to as the SPP cone (Figure 1). The use of a Weierstrass prism (*i.e.,* hyper-hemispherical prism) adjacent to a metal film in the Kretschmann configuration enables one to collect all the scattered light produced within the SPP cone.[21-23] The present work is an experimental study of the metal-sulfur vibrational bond of a benzenethiol monolayer on smooth planar gold and silver surfaces by directional Raman scattering. It is shown that directional

Raman scattering will be a useful alternative to study numerous devices containing smooth metallic films including biosensors, solar cells, and semiconductors.

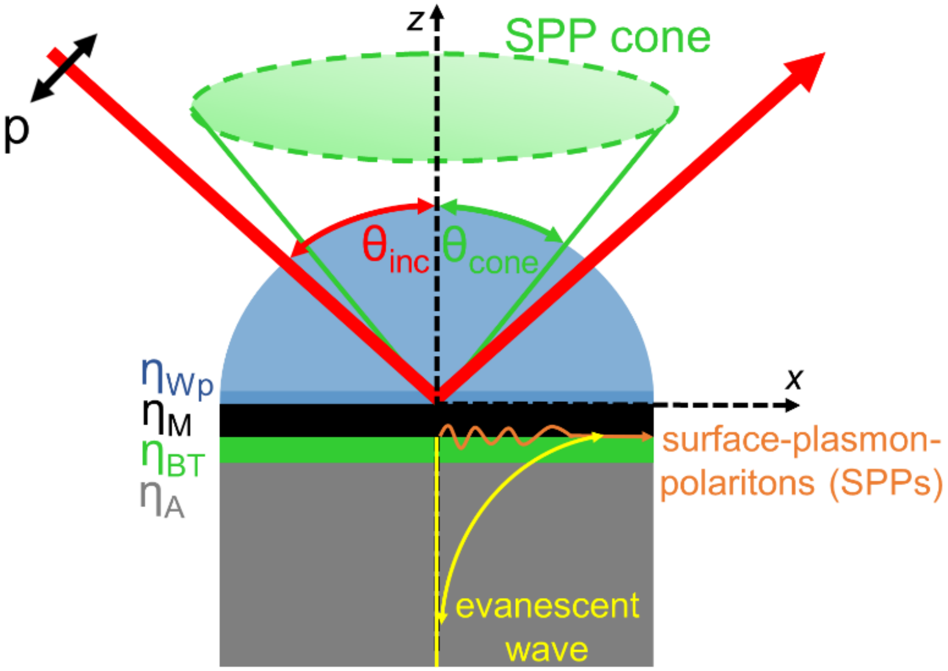

Figure 1. Schematic of the directional Raman scattering geometry for detecting benzenethiol (BT) monolayer on three types of metallic substrates composed of a smooth gold film, a smooth silver film, and colloidal gold nanoparticles coated on top of a smooth gold film. Only p-polarized light can couple to SPPs. (Surface-plasmon-polariton cone: SPP cone, Weierstrass prism: Wp, metal film: M, air layer: A, incident angle of light: θ_{inc}, SPP cone angle: θ_{cone})

Materials and Methods

Materials

1,2-Ethanedithiol (assay ≥98.0%, CAS# 540-63-6), benzenethiol (assay 99%, CAS# 108-98-5), gold(III) chloride hydrate (assay 99.995% trace metals basis, CAS# 27988-77-8), sodium citrate dihydrate (assay ≥99% FG, CAS# 6132-04-3), and 200 proof ethanol (assay 99.5%, CAS# 64-17-5) were obtained from Sigma-Aldrich (St. Louis, MO). Deionized water from an 18.2 MΩ cm^{-1} EasyPure II filtration system (Thermo Scientific, Waltham, MA) was used to prepare colloidal gold nanoparticles and for rinsing. All chemicals were used without further purifications.

Sample Fabrication

Three types of metal films were used in this study: smooth gold film, smooth silver film, and colloidal gold nanoparticle film. A smooth planar thin gold film of 50 nm was applied to a 25.4 mm diameter sapphire substrate (Meller Optics, Providence, RI) with a 2 nm titanium (99.999% pure Ti) adhesive layer (metal deposition by Platypus Technologies LLC., Madison, WI). A smooth planar 48 ± 2 nm silver film was prepared by a sputter-up-type sputtering system (ATC 1800-F, AJA International, Scituate, MA) for RF sputtering high purity silver thin wire (99.99% Ag, Ted Pella, Inc., Redding, CA) onto a sapphire substrate. Silver metal sputtering was achieved using a deposition rate of 0.05 nm/s, while rotating the substrate at 15 rpm under 10^{-5} torr argon pressure and a filament current of 8 Amps. Oxidization of the silver film[24] was reduced by quickly placing the film in a nitrogen enclosed chamber until further use.

Gold nanoparticles were synthesized and characterized with ultraviolet-visible absorption spectroscopy (Figure S1 Supporting Information). The colloidal gold nanoparticle films (*i.e.*, roughened gold films) were fabricated (Figure 2a) by immersing the smooth planar gold film in an ethanolic 10 mM solution of 1,2-ethanedithiol for 24 h to produce a thiol terminal group. Then, the film was placed in 0.25 mM colloidal gold nanoparticles solution for 24 h.

Prior to use, the metal films were cleaned with 200 proof ethanol and rinsed with deionized water. The cleaned metal films were dried with a stream of N_2 gas. Lastly, to form a SAM of benzenethiol, the cleaned films were immersed in an ethanoic 20 mM benzenethiol solution for 24 h (Figure 2). The monolayer samples were rinsed with ethanol to remove unreacted benzenethiol molecules and dried with a stream of N_2 gas. The Weierstrass prism (sapphire hemispherical prism + sapphire window, ISP Optics Irvington, NY) and the metallic films on a sapphire substrate were optically coupled with a refractive index ($\eta_D = 1.7400$)

matching fluid (Cargille laboratories Inc., Cedar Grove, NJ), to ensure optical contact without the presence of air gaps.

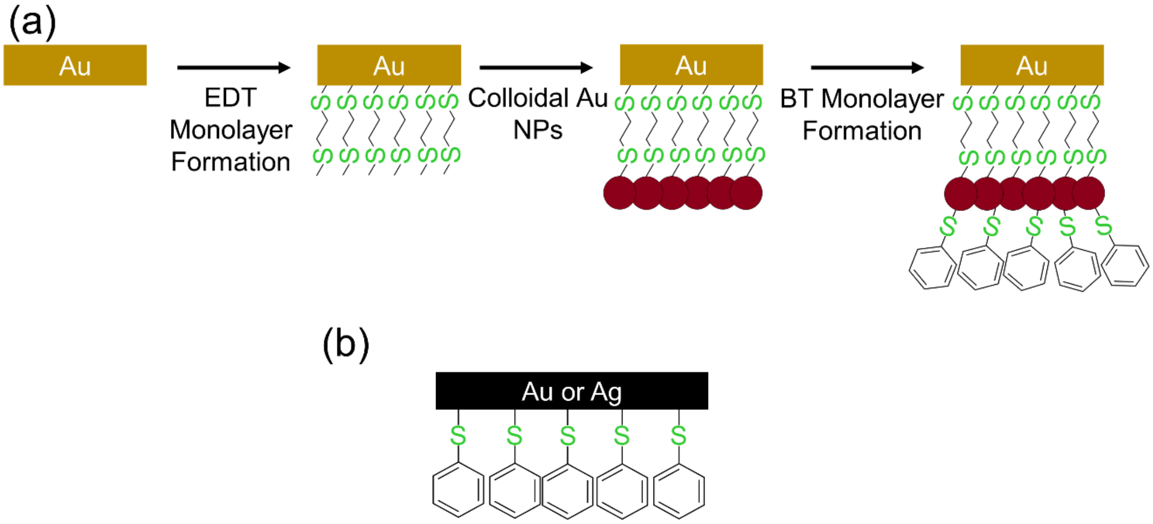

Figure 2. (a) Scheme of the surface chemistry modification procedure for fabricating colloidal gold nanoparticle film on a smooth planar 50 nm gold film for SERS. (b) Diagram of benzenethiol (BT) self-assembled monolayer chemisorbed onto smooth planar 50 nm gold and 48 ± 2 nm silver films. Schematic is simplified and not drawn to scale. (1,2-ethanedithiol: EDT, colloidal gold nanoparticles: colloidal Au NPs).

Directional Raman Spectrometer

A previously described instrument[22,23] was used for all measurements. The directional Raman scattering geometry (Figure 1) consisted of a sapphire Weierstrass prism ($\eta = 1.7619$)[25], 50 nm gold film ($\eta = 0.1431$, $k = 4.799$)[26], 48 ± 2 nm silver film ($\eta = 0.18306$, $k = 4.8842$)[27], colloidal gold nanoparticle film, benzenethiol ($\eta = 1.568$)[22], and air ($\eta = 1.000$).[28] P-polarized excitation was provided by a 785-nm near-infrared diode laser (Toptica Photonics XTRA II, Victor, NY) with approximately 220 mW incident on the surface of a Weierstrass prism/sample/air interface. It is important to note that 785-nm is not an optimal wavelength to achieve the maximum signal enhancement with silver;[29,30] however, data for all three metal films were acquired with identical experimental conditions for comparison. The laser beam was focused to a diameter of 250 µm at the Weierstrass prism interface. The laser profile was cleaned up with a laser line filter. Two separate translational mirrors in synchronized motion were used to control the incident angle of light and to block the specular reflected light from reaching the detectors. Directional Raman data were collected from 15.00 to 55.00° incident angle with 0.25° angle resolution, except within ± 2° of the angle producing the maximum intensity, where an angle resolution of 0.06° was used.

The directional Raman signal emanating from the SPP cone was collected on the Weierstrass prism side with an aspherical lens (50 mm focal length and 75 mm diameter). An N-BK7 plano-convex lens (75 mm diameter, 100 mm focal length, Thor Laboratories, Newton, NJ) focused the collimated light onto a Kaiser HoloSpec Raman spectrometer (Kaiser Optical Systems, Inc. Ann Arbor, MI). The scattered radiation was focused onto a 100 µm slit and passed through a HSG-785-LF volume phase holographic grating. Detection was achieved with a Princeton Instruments (Trenton, NJ) PIXIS 400 1340 × 400 near-infrared-enhanced charged-coupled device (CCD, 20 µm × 20 µm pixels) that was thermoelectrically cooled to -70 °C. The CCD images were processed with the Princeton Instruments WinSpec/32 [v.2.6.14 (2013)] software. For wavelength calibration, a solution of acetonitrile-toluene was used. An acquisition time of 60 s and 3 accumulations was used. All spectra were collected at room temperature and three replicate experiments were conducted.

SPP Cone Images

Images of the SPP cones (*i.e.*, directional Rayleigh signal) from the gold, silver, and colloidal gold nanoparticle films were collected at the maximum cone intensity angle with a 75 mm (f/1.3) Kameratori TV Lens (Tampere, Finland) attached to an 11.340 mm × 7.130 mm, 2.32 mega pixel CMOS sensor (IDS Imaging Development Systems GmbH, Obersulm, Germany). The cone images were acquired at a fixed distance between the sample holder and the camera.

The acquired CMOS cone images were analyzed with Image-J 1.44p (National Institutes of Health, USA).

Data Analysis

Calculations to acquire the SPP cone angle were performed with finite-difference time-domain simulations (OptiFDTD, Optiwave Systems Inc., Ottawa, ON, Canada) of a four-layered system (prism/metal/analyte/air) with a 25 µm × 25 µm simulation dimension window, a mesh size of 0.008 µm, and a continuous transverse magnetic wave of 785-nm for p-polarized excitation. The experimental SPP cone angles were obtained using a nonlinear cubic polynomial function to account for cone compression from the collection lens.[22,23] Briefly, an image of the SPP cone with a metal ruler placed between the prism and the detector was acquired and the ruler scale was used to generate a distance per pixel calibration. The Radial Profile Plot Java Script in Image-J 1.44p (National Institutes of Health, USA) software was used to obtain the SPP cone diameter and the cubic polynomial equation was used to correct the diameter of the SPP cone. The experimental SPP cone angle was calculated using the inverse-tangent of the distance between the prism (*i.e.*, sample interface) and detector as well as the corrected diameter of the SPP cone.

Fresnel reflectivity calculations were performed to model the reflected light intensity as a function of incident angle. These calculations were used to determine the incident angles that produced surface plasmons at the surface plasmon resonance (SPR) angles, where the greatest attenuation of the reflected light intensity was obtained and the most intense SPP cone image and cone intensity were acquired. It was assumed that all layers have a constant refractive index (η) at 785-nm excitation and were homogenous. An IGOR Pro (WaveMetrics, Inc., Lake Oswego, OR) graphical macros program available from Corn et al.[31] was used. The lowest angle resolution of 0.009° with an angle range of 34.000 to 38.000° was utilized. Three-dimensional finite-difference time-domain simulation software (EM Explorer, San Francisco, CA) was used to perform sum square electric field (SSEF) intensity calculations in the interfacial layers to model the experimental Raman peak amplitude of the Au-S bond. The input simulation parameters were: Yee cell size of 5 nm, 2000 cycles, a 35.00 to 55.00° angle range and a 0.05° angle resolution. The thicknesses of the prism and air layers were semi-infinite. The signal-to-noise (S/N) ratios were calculated as the maximum Raman peak intensity of the metal-sulfur bands after background subtraction divided by the standard deviation of the noise measured in a region of the spectra where no analyte peaks were present between 1650 and 1750 cm^{-1}.

Results and Discussion

SPP Cone Images of Benzenethiol Monolayer Adsorbed on Metallic Films

Under total internal reflection using the sample geometry shown in Figure 1, the scattered light produced on the sapphire side of the Weierstrass prism assembly is directional. In other words, the scattered light emanates at a well-defined angle as an SPP cone. The directionality of the Rayleigh scattered photons is easily monitored by collecting an image of the SPP cone for the three metallic surfaces included in this study: a smooth gold film, a smooth silver film, and a smooth gold film on which colloidal gold nanoparticles are immobilized (Figure 3). The latter substrate has nanoscale roughness and serves as a simple SERS substrate. All three metal films produce a strong directional signal, as evidenced by the appearance of an SPP cone. Each cone image was acquired at an incident angle corresponding to the SPR angle, where the highest attenuation of the reflected light from the prism and the maximum SPP cone intensity are measured (Table 1).

Table 1. Measured and (calculated) incident angles used to collect the SPP cone images shown in Figure 3, and the SPP cone angles of the Rayleigh scattered light from three metallic films before and after the adsorption of a benzenethiol monolayer

Type of Metal Film	**Incident Angle (°)**		**SPP Cone Angle (°)**	
	Before	**After**	**Before**	**After**
Smooth Gold	35.53 (35.530)	35.60 (35.572)	34.8 ± 0.1 (34.794)	35.3 ± 0.1 (35.218)
Smooth Silver	35.50 (35.496)	35.64 (35.633)	34.4 ± 0.3 (34.848)	35.0 ± 0.3 (35.253)
Colloidal Gold Nanoparticles on Smooth Gold	36.18	39.83	35.34 ± 0.05	35.3 ± 0.1

Note. SPP: surface-plasmon-polariton. The average and standard deviation are from two SPP cone images of each metal film.

The SPP cones were also measured after immobilizing a benzenethiol monolayer to each of the metallic substrates (Figure 3). The incident angle that produced the most intense SPP cone after immobilizing a benzenethiol monolayer shifted to larger angles compared to the bare metallic substrate (Table 1). This angle shift is analogous to the shifts measured in an SPR experiment, as previously reported.[22,23] The measured and (calculated) incident angle shifts are 0.07° (0.042°) for the gold film, 0.14° (0.133°) for the silver film (Figure S2 Supporting Information), and 3.67° for the colloidal gold nanoparticle substrate, respectively. The calculated incident angles for the gold and silver films before and after the adsorption of benzenethiol are in good agreement with the experimental incident angles. For the SERS substrate, the calculated incident angle is not easily obtained due to the complexity and the uneven distribution of the gold nanoparticles on the metal surface.[20,32] In addition, the SPP cone angle (the angle at which the directional scattering is produced) also increased after immobilizing a benzenethiol monolayer on flat gold and silver surfaces (Table 1, Figure 3a and 3b). The angle changes measured after benzenethiol adsorption are due to changes in the refractive index of the dielectric medium adjacent to the metallic films upon formation of the monolayer. It is noteworthy to mention that the SPP cone angles are statistically the same for the roughened gold surface with colloidal gold nanoparticles before and after the adsorption of benzenethiol (Figure 3c), this may be due to the rough nature of the metal surface and the impact this has on the directionality of the scattered light.[20]

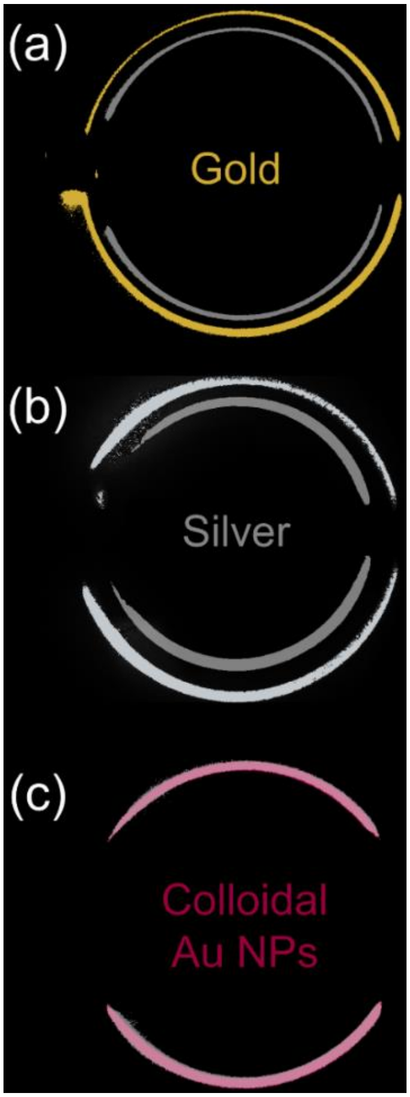

Figure 3. Surface-plasmon-polariton (SPP) cone images of the three metallic films (a) smooth gold film, (b) smooth silver film, and (c) colloidal gold nanoparticles immobilized on a smooth

gold film. The images obtained before and after adsorption of benzenethiol are overlapped to show the change in SPP cone angle. The dark gray inner cones in (a, b) represent before adsorption of a benzenethiol monolayer. The outer cones in (a, gold) and (b, light gray) are the SPP cones after adsorption of a benzenethiol monolayer. In (c), there is no change in the SPP cone angle before and after benzenethiol adsorption, so only a single SPP cone is observable in the overlapped image. The cones are not continuous because two translational mirrors block the incident and reflected light from reaching the detector. The incident angles used to acquire the SPP cones and the SPP cone angles are summarized in Table 1.

Directional Raman Scattering of Benzenethiol Monolayer Adsorbed on Metallic Films

In addition to the Rayleigh scattered light, the Raman scattered light from the adsorbed molecules on the metallic films is also encoded within the SPP cone (as is background, which is discussed below). In order to measure the directional Raman spectrum, the SPP cone is collected, directed through a spectrometer, and measured with a CCD camera. Figure 4 shows the directional Raman spectra of the metallic films before and after immobilizing a benzenethiol monolayer. The spectra are collected at the incident angles where the SPP cone images are acquired in Figure 3. The directional Raman spectra of the bare metallic films prior to forming the benzenethiol monolayer are shown in Figure 4c, 4e, and 4g for the colloidal gold nanoparticle, gold, and silver films, respectively. The Raman bands within the light blue regions at 116, 146, 213, between 350 and 800, 1075, and 1350 cm^{-1} originate from the sapphire[33] Weierstrass prism and substrate[34] as shown in Figure 4h. (There is a low intensity mode of benzenethiol at 614 cm^{-1}, but this peak was not detected for the monolayers). The strong sapphire Raman peaks are due in part to the long path length of the laser through the prism and sapphire substrate. Some variation is measured in the intensity of the sapphire peaks originating from the prism and substrate (Figure S3 Supporting Information).[33]

The Raman spectrum of a neat benzenethiol solution and the directional Raman spectra of a benzenethiol monolayer chemisorbed on the metal films are shown in Figure 4. The predominate benzenethiol Raman peaks are 697, 999, 1023, and 1573 cm^{-1} (Figure 4a). These bands are assigned to the C-S stretching mode, aromatic ring stretching mode, CH in-plane deformation mode, and aromatic ring stretching mode of benzene, respectively.[34-41] Table S1 (Supporting Information) shows a summary of the Raman peak assignments for all of the metallic surfaces studied. The predominate benzenethiol Raman bands are observed for the monolayer adsorbed on gold, silver, and colloidal gold nanoparticle films.

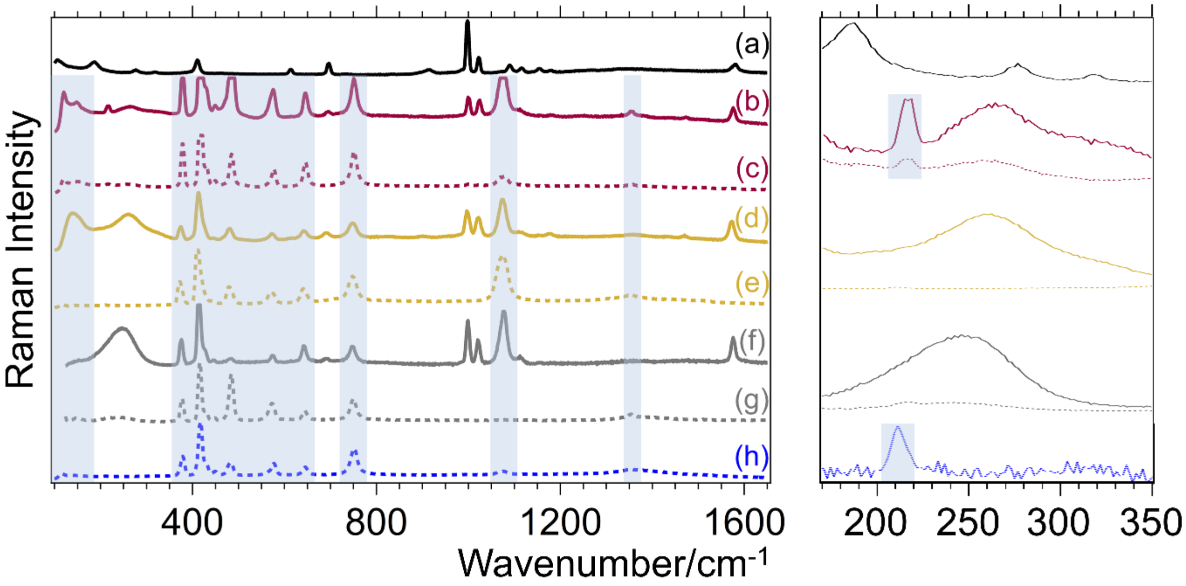

Figure 4. (black line, a) Raman spectrum of neat benzenethiol collected using a conventional backscattering Raman microscopy geometry. Directional Raman spectra of a benzenethiol monolayer on (red line, b) colloidal gold nanoparticle film, (gold line, d) smooth 50 nm gold film, and (gray line, f) smooth 48 nm silver film. The dashed-lines represent control measurements prior to benzenethiol immobilization (c, e, g) using the same color scheme. The blue dashed-line (h) represents a sapphire Weierstrass prism without a metallic substrate. The panel on the right shows an expanded region of the Au-S and Ag-S vibrational bands using the same color scheme. The highlighted blue regions correspond to Raman peaks of sapphire. The incident angles used to collect the directional Raman spectra are listed in Table 1. (Spectrum h was collected at 34.59°).

The Au-S peak at 263 ± 2 cm^{-1} can be seen in Figure 4b, 4c, and 4d. This vibrational mode assignment agrees with previously reported experimental[36,42] and computational[1,14,43] data of the Au-S bond. The Au-S bond is measured on the colloidal gold nanoparticle film before benzenethiol adsorption on the SERS substrate (Figure 4c) since a 1,2-ethanedithiol monolayer was used to immobilize the colloidal gold nanoparticles; the intensity of this peak increased after immobilizing benzenethiol (Figure 4b). The Ag-S peak is measured at 246 cm^{-1} (Figure 4f), and corresponds to the 230 to 250 cm^{-1} range reported in the literature by Carron and Hurley[44] and Matulaitienė et al.[13]

The exponential decay of the evanescent wave from the metal surface (as shown schematically in Figure 1), means that the evanescent wave has its greatest intensity at the location of the metal-sulfur bonds, which generates measurable Raman signals from this relatively weak scattering mode. The signal-to-noise (S/N) ratio of the metal-sulfur band is 30, 60, and 100 on a nanoparticle roughened gold film, smooth gold film, and smooth silver film, respectively. The large S/N ratios are attributed not only to the magnitude of the enhanced electric field at the metallic interface, but also to the directionality of the scattered light at a defined angle that leads to the efficient collection of the directional signal. The relatively low S/N ratio for the SERS substrate is surprising, and may be the result of increased background, which is a known phenomenon of SERS.[45] The colloidal gold SERS substrate used in this work was relatively simple, and better performance may be expected with more sophisticated SERS substrates.[46,47] Importantly, the measurement of the Au-S and Ag-S vibrational modes on smooth planar surfaces can be measured with directional Raman scattering without requiring a SERS substrate to further enhance the signal.

The S/N ratio of the Au-S Raman bands is sufficiently above the detection limit to conclude that the peak shifts to higher wavenumbers when comparing the substrate containing only 1,2-ethanedithiol (240 cm^{-1}) and after adding benzenethiol (264 cm^{-1}) to the gold nanoparticle roughened metallic surface (Figure S4 Supporting Information). This means that the molecular backbone of the SAMs of 1,2-ethanedithiol (an aliphatic compound) or benzenethiol (an aromatic compound) chemisorbed on the gold surface can induce a change in the Raman peak location of the Au-S band, most likely due to differences in the absorption energies of the monolayer.[48-53] Furthermore, the Au-S Raman shifts of the benzenethiol SAM on the colloidal gold nanoparticle roughened surface (264 cm^{-1}) and the smooth gold surface (261 cm^{-1}), respectively, are statistically the same in terms of the maximum Raman peak position given the Raman shift resolution of our spectrometer.

The directional Raman spectra were collected as a function of the incident angle ranging from 15 to 55° for a benzenethiol monolayer on a smooth planar gold film. The Au-S spectral region is shown in Figure 5a and 5b. A cross-section of the 261 cm^{-1} Au-S stretching mode from an incident angle of 34 to 38° is shown as the dotted black symbols in Figure 5c. As stated above, the incident angle where the Raman signal is the most intense correlates with the SPR angle (35.572°) in the calculated reflectivity curve (solid blue line, Figure 5c). These angles are in good agreement to the calculated value of the sum squared electric field (SSEF) at the interface (solid red line, Figure 5c); the maximum SSEF intensity is observed at 35.588° for this sample. The incident angles from the experiment, the reflectivity calculations and the SSEF calculations are within ± 0.01°, showing that the directional Raman signal is accurately modeled. The directional Raman scattering technique can provide sensitive measurements of the Au-S or Ag-S bonds as shown in this study, offering an alternative to the application of a SERS substrate and the associated complex signal modeling that may be required**.**

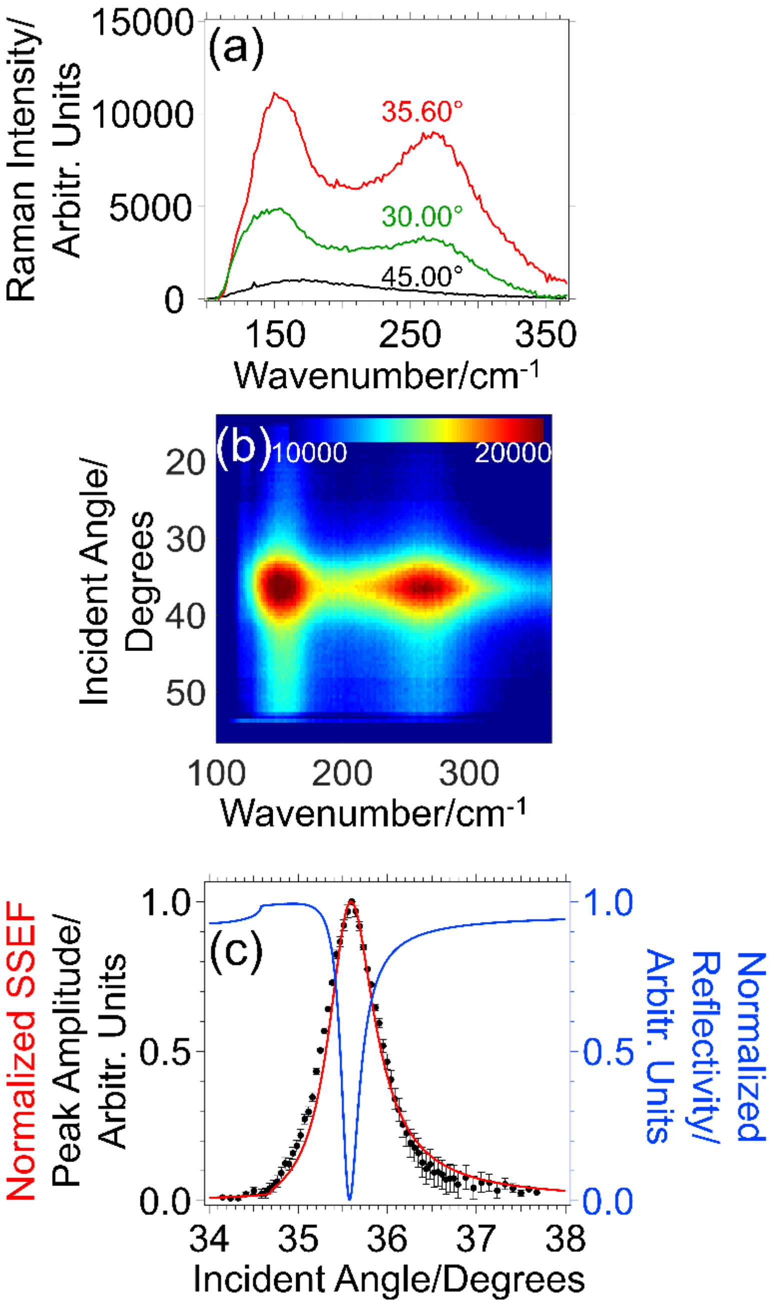

Figure 5. (a) Directional Raman spectra of a benzenethiol monolayer on smooth planar gold film collected at three incident angles. The Raman peaks are assigned to sapphire (146 cm^{-1}) and Au-S stretching mode (261 cm^{-1}). (b) Two-dimensional plot of the Raman scattering intensity as a function of Raman shift and incident angle on a color amplitude scale. The two Raman bands correspond to the Raman spectra shown in (a). The maximum Raman scattering intensity is observed at θ_{inc} = 35.60°. (c) The calculated Fresnel reflectivity curve shown in blue and the plot of the 261 cm^{-1} Au-S Raman peak amplitude *versus* incident angle (shown in black). The red line represents the sum square electric field (SSEF) fit to the experimental data (black symbol). The uncertainties represent standard deviation from three replicate measurements.

Conclusions

Directional Raman scattering provides the capability for monolayer sensitive measurements without the use of SERS. Since directional Raman spectroscopy can provide one to two orders of magnitude enhancement from total internal reflection conditions in addition to the enhancement that results from collecting the Raman signal encoded within the full SPP cone, the Au-S and Ag-S vibrational mode of a benzenethiol monolayer can be probed on smooth planar metallic surfaces. The use of smooth substrates to acquire the directional Raman spectra of adsorbates may eliminate the limitations of SERS techniques such as increased background, poor reproducibility, and potentially prolonged substrate preparation time.[54-56] Directional Raman scattering can be used to characterize surface modification steps as well as a sensor readout, including SPR-based biosensors, in which monolayer-sensitive chemical information is provided along with the ability to gain rapid quantitative responses when biomolecules adhere to a metallic surface. This may propel new and emerging technologies in which functionalization of a surface by SAMs is needed.

Acknowledgements

This material is based upon work supported by the National Science Foundation under Grant Number CHE-1709099. We acknowledge Andrew C. Hillier Research Laboratory from the Department of Chemical and Biological Engineering (Iowa State University, Ames, Iowa) for help with silver film deposition. Any opinions, findings, and conclusions or recommendations expressed in this material are those of the authors and do not necessarily reflect the views of the National Science Foundation. Stephen C. Weibel (Surface Photonics) has commercial interest in the development of a detection system for directional Raman scattering.

References

[1] H. Häkkinen, *Nat. Chem.* **2012**, *4*, 443.

[2] T. Łuczak, *Measurement* **2018**, *126*, 242.

[3] M. Mrksich, G. M. Whitesides, *Trends in Biotechnol.* **1995**, *13*, 228.

[4] J. T. Koepsel, W. L. Murphy, *Chembiochem.* **2012**, *13*, 1717.

[5] J. D. Delgado, R. L. Surmaitis, S. Abou Shaheen, J. B. Schlenoff, *ACS Appl. Mater. Interfaces* **2019**, *11*, 3524.

[6] N. Tillman, A. Ulman, T. L. Penner, *Langmuir* **1989**, *5*, 101.

[7] M. Zharnikov, M. Grunze, *J. Phys.: Condens. Matter* **2001**, *13*, 11333.

[8] M. A. Bryant, J. E. Pemberton, *J. Am. Chem. Soc.* **1991**, *113*, 8284.

[9] A. Ulman, *Chem. Rev.* **1996**, *96*, 1533.

[10] J. P. Folkers, P. E. Laibinis, G. M. Whitesides, *Langmuir* **1992**, *8*, 1330.

[11] G. M. Whitesides, P. E. Laibinis, *Langmuir* **1990**, *6*, 87.

[12] J. C. Love, L. A. Estroff, J. K. Kriebel, R. G. Nuzzo, G. M. Whitesides, *Chem. Rev*. **2005**, *105*, 1103.

[13] I. Matulaitienė, Z. Kuodis, A. Matijoška, O. Eicher-Lorka, G. Niaura, *J. Phys. Chem. C* **2015**, *119*, 26481.

[14] B. Varnholt, P. Oulevey, S. Luber, C. Kumara, A. Dass, T. Bürgi, *J. Phys. Chem. C* **2014**, *118*, 9604.

[15] A. Tlahuice-Flores, R. L. Whetten, M. Jose-Yacaman, *J. Phys. Chem.* C **2013**, *117*, 12191.

[16] T. Ikeshoji, Y. Ono, T. Mizuno, *Appl. Opt.* **1973**, *12*, 2236.

[17] R. Iwamoto, K. Ohta, M. Miya, S. Mima, *Appl. Spectrosc.* **1981**, *35*, 584.

[18] D. A. Beattie, M. L. Larsson, A. R. Holmgren, *Vib. Spectrosc.* **2006**, *41*, 198.

[19] D. A. Woods, C. D. Bain, *Analyst* **2012**, *137*, 35.

[20] A. J. Braundmeier, H. E. Tomaschke, *Opt. Commun.* **1975**, *14*, 99.

[21] H. J. Simon, J. K. Guha, *Opt. Commun.* **1976**, *18*, 391.

[22] C. K. A. Nyamekye, S. C. Weibel, J. M. Bobbitt, E. A. Smith, *Analyst* **2018**, *143*, 400.

[23] C. K. A. Nyamekye, Q. Zhu, R. Mahmood, S. C. Weibel, A. C. Hillier, E. A. Smith, *Anal. Chim. Acta* **2019**, *1048*, 123.

[24] W. M. Moore, P. J. Codella, *J. Phys. Chem.* **1988**, *92*, 4421.

[25] B. Michael In *Handbook of Optics: Volume IV - Optical Properties of Materials, Nonlinear Optics, Quantum Optics, Third Edition*; McGraw Hill Professional, New York, **2010**.

[26] P. B. Johnson, R. W. Christy, *Phys. Rev. B* **1972**, *6*, 4370.

[27] A. D. Rakić, A. B. Djurišić, J. M. Elazar, M. L. Majewski, *Appl. Opt.* **1998**, *37*, 5271.

[28] P. E. Ciddor, *Appl. Opt.* **1996**, *35*, 1566.

[29] B. A. Prabowo, A. Purwidyantri, K.-C. Liu, *Biosensors* **2018**, *8*, 80.

[30] K. A. Willets, R. P. V. Duyne, *Annu. Rev. Phys. Chem.* **2007**, *58*, 267.

[31] R. M. Corn, *Complex Fresnel Calculations For Igor Pro Macros available from http://corninfo.ps.uci.edu/writings/Ref4txt.html* **2014**.

[32] S. A. Meyer, E. C. Le Ru, P. G. Etchegoin, *Anal. Chem.* **2011**, *83,* 2337.

[33] J. Thapa, B. Liu, S. D. Woodruff, B. T. Chorpening, M. P. Buric, *Appl. Opt.* **2017**, *56*, 8598.

[34] M. A. Bryant, S. L. Joa, J. E. Pemberton, *Langmuir* **1992**, *8*, 753.

[35] R. L. Aggarwal, L. W. Farrar, N. G. Greeneltch, R. P. Van Duyne, D. L. Polla, *Appl. Spectrosc.* **2012**, *66*, 740.

[36] R. Holze, *Phys. Chem. Chem. Phys.* **2015**, *17*, 21364.

[37] W. K. Yi, C.-W. Park, M.-S. Kim, K. Kim, *Bull. Korean Chem. Soc.* **1987**, *8*, 291.

[38] D. W. Scott, J. P. McCullough, W. N. Hubbard, J. F. Messerly, I. A. Hossenlopp, F. R. Frow, G. Waddington, *J. Am. Chem. Soc.* **1956**, *78*, 5463.

[39] J. H. S. Green, *Spectrochim. Acta Part A* **1968**, *24*, 1627.

[40] C. E. Taylor, J. E. Pemberton, G. G. Goodman, M. H. Schoenfisch, *Appl. Spectrosc.* **1999**, *53*, 1212.

[41] L.-J. Wan, M. Terashima, H. Noda, M. Osawa, *J. Phys. Chem. B* **2000**, *104*, 3563.

[42] C. S. Levin, B. G. Janesko, R. Bardhan, G. E. Scuseria, J. D. Hartgerink, N. J. Halas, *Nano Lett.* **2006**, *6*, 2617.

[43] T. Burgi, *Nanoscale* **2015**, *7*, 15553.

[44] K. T. Carron, L. G. Hurley, *J. Phys. Chem.* **1991**, *95*, 9979.

[45] S. Mahajan, R. M. Cole, J. D. Speed, S. H. Pelfrey, A. E. Russell, P. N. Bartlett, S. M. Barnett, J. J. Baumberg, *J. Phys. Chem. C* **2010**, *114*, 7242.

[46] P. A. Mosier-Boss, *Nanomaterials* **2017**, *7*, 142.

[47] J. Langer, D. Jimenez de Aberasturi, J. Aizpurua, R. A. Alvarez-Puebla, B. Auguié, J. J. Baumberg, G. C. Bazan, S. E. J. Bell, A. Boisen, A. G. Brolo, J. Choo, D. Cialla-May, V. Deckert, L. Fabris, K. Faulds, F. J. García de Abajo, R. Goodacre, D. Graham, A. J. Haes, C. L. Haynes, C. Huck, T. Itoh, M. Käll, J. Kneipp, N. A. Kotov, H. Kuang, E. C. Le Ru, H. K. Lee, J.-F. Li, X. Y. Ling, S. A. Maier, T. Mayerhöfer, M. Moskovits, K. Murakoshi, J.-M. Nam, S. Nie, Y. Ozaki, I. Pastoriza-Santos, J. Perez-Juste, J. Popp, A. Pucci, S. Reich, B. Ren, G. C. Schatz, T. Shegai, S. Schlücker, L.-L. Tay, K. G. Thomas, Z.-Q. Tian, R. P. Van Duyne, T. Vo-Dinh, Y. Wang, K. A. Willets, C. Xu, H. Xu, Y. Xu, Y. S. Yamamoto, B. Zhao, L. M. Liz-Marzán, *ACS Nano* **2020**, *14*, 28.

[48] Q. Jin, J. A. Rodriguez, C. Z. Li, Y. Darici, N. J. Tao, *Surf. Sci.* **1999**, *425*, 101.

[49] C. Vericat, M. E. Vela, G. Benitez, P. Carro, R. C. Salvarezza, *Chem. Soc. Rev.* **2010**, *39*, 1805.

[50] C. Vericat, M. E. Vela, R. C. Salvarezza, *Phys. Chem. Chem. Phys.* **2005**, *7*, 3258.

[51] J. Zhang, A. Bilič, J. R. Reimers, N. S. Hush, J. Ulstrup, *J. Phys. Chem. B* **2005**, *109*, 15355.

[52] Zhou, T. Baunach, V. Ivanova, D. M. Kolb, *Langmuir* **2004**, *20*, 4590.

[53] E. Pensa, E. Cortés, G. Corthey, P. Carro, C. Vericat, M. H. Fonticelli, G. Benítez, A. A. Rubert, R. C. Salvarezza, *Acc. Chem. Res.* **2012**, *45*, 1183.

[54] D. Graham, K. Faulds, *Expert Rev. Mol. Diagn.* **2009**, *9*, 537.

[55] M. W. Meyer, E. A. Smith, *Analyst* **2011**, *136*, 3542.

[56] P. L. Stiles, J. A. Dieringer, N. C. Shah, R. P. V. Duyne, *Annu. Rev. Anal. Chem.* **2008**, *1*, 601.

Supporting Information

The Supporting Information include: the experimental procedure for synthesizing colloidal gold nanoparticles, the UV-VIS absorbance spectrum of synthesized colloidal gold nanoparticles, a table of the Raman peak locations and assignments for neat benzenethiol, and benzenethiol monolayer on three metallic surfaces, experimentally measured and calculated surface plasmon resonance reflectivity curves for silver film before and after immobilizing a benzenethiol monolayer, and directional Raman spectra of 1,2-ethanedithiol monolayer on smooth gold film, benzenethiol monolayer on colloidal roughened gold nanoparticle film and a comparison of two different 50 nm bare gold films.

The experimental procedure for synthesizing colloidal gold nanoparticles is as follows. The Turkevich method[1] was used to prepare colloidal Au NPs. Briefly, ~170 mg of gold(III) chloride hydrate ($AuCl_4{\bullet}H_2O$) was dissolved in 100 mL deionized water. The beaker was wrapped in aluminum foil with an aluminum foil dome lid and placed on a magnetic stirrer/hotplate. A 0.5% w/v sodium citrate dihydrate solution in 50 mL deionized water was prepared while the $AuCl_3$ solution was heated and stirred at 150 rpm. As soon as the boiling commenced, sodium citrate dihydrate solution was added in small drops into the aluminum wrapped beaker until a deep red color developed. The solution was removed from the heating element, with continued stirring at 150 rpm until the solution cooled to room temperature.

Ultraviolet-visible (UV-VIS) absorption spectroscopy was used to characterize the synthesized colloidal nanoparticles (Figure S1 Supporting Information). The UV-VIS optical absorbance spectrum showed a wavelength peak maximum at 519 ± 1 nm, which was in agreement with reported values at 520 nm for a ~15 nm diameter size colloidal gold nanoparticle using the Turkevich method.[1-4]

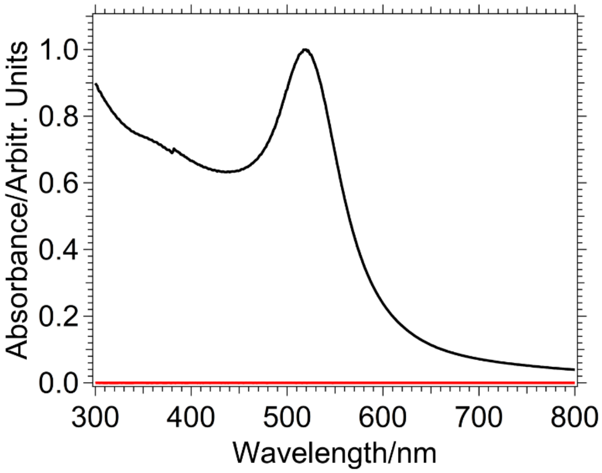

Figure S1. UV-VIS absorbance spectra of (black line) synthesized colloidal gold nanoparticles in aqueous solution and (red line) deionized water. The colloidal gold nanoparticles have a maximum wavelength of 519 ± 1 nm.

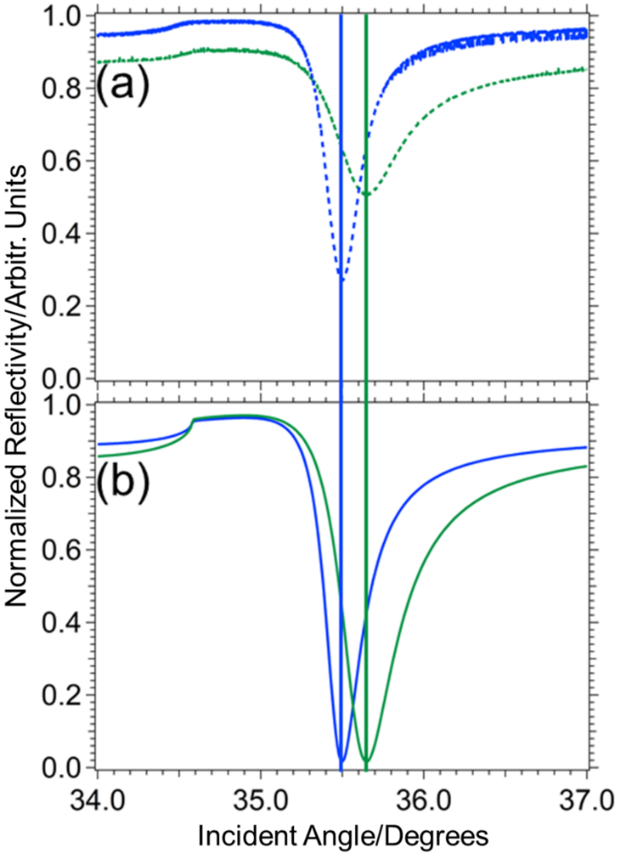

Figure S2. (a) Experimentally measured and (b) calculated surface plasmon resonance (SPR) reflectivity curves for (blue) a bare 48 ± 2 nm silver film and (green) after immobilization of a benzenethiol monolayer adsorbed on the silver film. See Table 1 for the incident angles. The experimental data was collected on a home-built SPR instrument.[19]

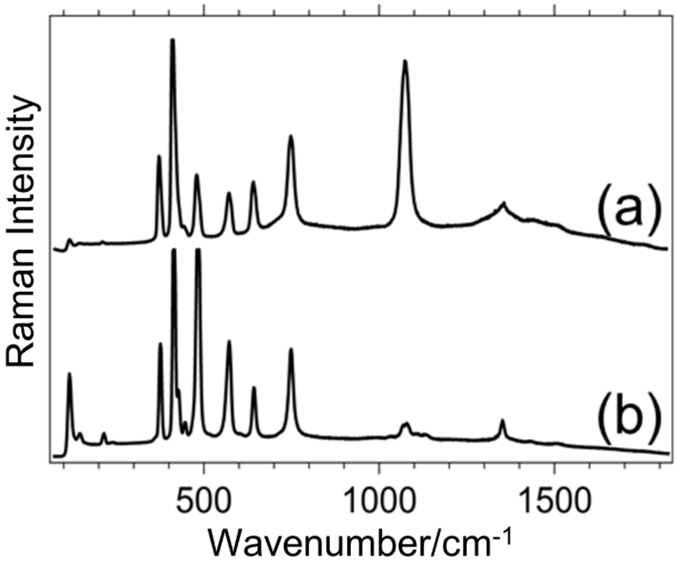

Figure S3. Directional Raman spectra of two different (a and b) 50 nm gold films collected with an incident angle of 35.53°. The peaks are assigned to sapphire, and variations in peak intensity are noted. The reasons for this variation are not known, but may be due to the presence of impurity dopants that can lead to microscopic defects in the sapphire substrate or other differences in the sapphire structure.[20]

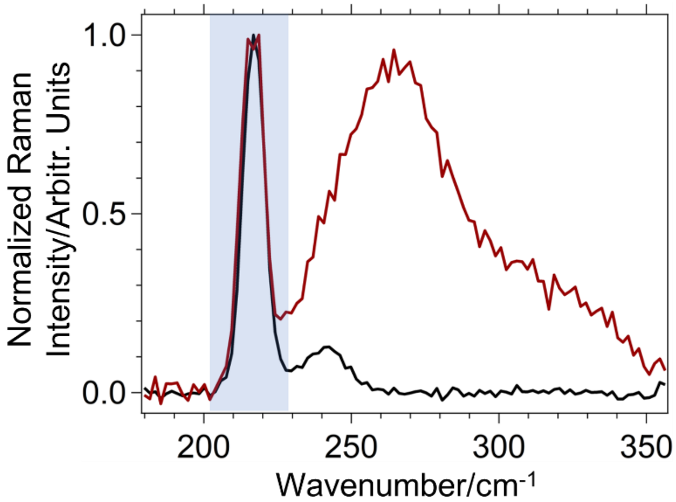

Figure S4. Normalized directional Raman spectra of (black trace) 1,2-ethanedithiol monolayer on a smooth 50 nm gold film and (red trace) benzenethiol monolayer adsorbed on colloidal gold nanoparticle roughened film. The Au-S bands of 1,2-ethanedithiol monolayer on the smooth gold film and benzenethiol monolayer on the roughened gold surface are 240 and 264 cm^{-1}, respectively. The sapphire peak at 217 cm^{-1} is indicated in the blue region and the spectra are normalized to this peak. The spectra were collected with incident angles of (black trace) 35.53° and (red trace) 39.83°.

Table S1. Raman peaks of neat benzenethiol and benzenethiol monolayers adsorbed on smooth planar gold, smooth silver, and colloidal gold roughened nanoparticle films. All assignments are based on literature data.[5-18] The benzenethiol peaks that were not measured in the directional Raman spectrum were low in intensity or overlapped with a sapphire peak

Raman Shift (cm^{-1})				**Peak Assignment**
Neat Benzenethiol	**Gold**	**Silver**	**Colloidal Gold Nanoparticles on Smooth Gold**	
187	-	-	-	Aromatic ring out-of-plane deformation
-	261	246	264	Au-S stretch/ Ag-S stretch
277	-	-	-	C-S in-plane bending
410		-	-	C-H stretch
614	-	-	-	Aromatic ring in-plane deformation
697	691	690	695	C-S stretch
911	-	-	-	C-S-H stretch
999	996	999	999	Aromatic ring stretch
1023	1022	1020	1023	CH in-plane deformation
1090	-	-	-	Aromatic ring stretch
1116	-	1112	1110	In plane C-C-C stretch C-S stretching C-H bend
1155	-	-	-	In-plane deformation of C-H
1181	1177	-	1177	In-plane deformation of C-H
1584	1573	1580	1574	Aromatic ring stretch

References

[1] J. Turkevich, P. C. Stevenson, J. Hillier, *Discuss. Faraday Soc.* **1951**, *11*, 55.

[2] P. Mulvaney, *Langmuir* **1996**, *12*, 788.

[3] K. C. Grabar, R. G. Freeman, M. B. Hommer, M. J. Natan, *Anal. Chem.* **1995**, *67*, 735.

[4] W. Haiss, N. T. K. Thanh, J. Aveyard, D. G. Fernig, *Anal. Chem.* **2007**, *79*, 4215.

[5] M. A. Bryant, S. L. Joa, J. E. Pemberton, *Langmuir* **1992**, *8*, 753.

[6] R. L. Aggarwal, L. W. Farrar, N. G. Greeneltch, R. P. Van Duyne, D. L. Polla, *Appl. Spectrosc.* **2012**, *66*, 740.

[7] R. Holze, *Phys. Chem. Chem. Phys.* **2015**, *17*, 21364.

[8] W. K. Yi, C-W. Park, M-S. Kim, K. Kim, *Bull. Korean Chem. Soc.* **1987**, *8*, 291.

[9] D. W. Scott, J. P. McCullough, W. N. Hubbard, J. F. Messerly, I. A. Hossenlopp, F. R. Frow, G. Waddington, *J. Am. Chem. Soc.* **1956**, *78*, 5463.

[10] J. H. S. Green, *Spectrochim. Acta, Part A* **1968**, *24*, 1627.

[11] C. E. Taylor, J. E. Pemberton, G. G. Goodman, M. H. Schoenfisch, *Appl. Spectrosc.* **1999**, *53*, 1212.

[12] L-J. Wan, M. Terashima, H. Noda, M. Osawa, *J. Phys. Chem. B* **2000**, *104*, 3563.

[13] K. T. Carron, L. G. Hurley, *J. Phys. Chem.* **1991**, *95*, 9979.

[14] A. Tlahuice-Flores, R. L. Whetten, M. Jose-Yacaman, *J. Phys. Chem. C* **2013**, *117*, 12191.

[15] G. Varsányi, *Assignments for Vibrational Spectra of Seven Hundred Benzene Derivatives*. Adam Hilger: London, **1974**.

[16] A. Wokaun, J. P. Gordon, P. F. Liao, *Phys. Rev. Lett.* **1982**, *48*, 957.

[17] F. R. Dollish, W. G. Fateley, F. F. Bentley, *Characteristic Raman Frequencies of Organic Compounds*. Wiley: New York, **1974**.

[18] L. Shujin, D. Wu, X. Xu, R. Gu, *J. Raman Spectrosc.* **2007**, *38*, 1436.

[19] A. Syed, Q. Zhu, E. A. Smith, *Biochim. Biophys. Acta, Biomembr.* **2016**, *1858*, 3141.

[20] J. Thapa, B. Liu, S. D. Woodruff, B. T. Chorpening, M. P. Buric, *Appl. Opt.* **2017**, *56*, 8598.

CHAPTER 6. GENERAL CONCLUSION

The focus of this dissertation is directional Raman scattering, a technique that is equivalent to total internal reflection Raman spectroscopy. Directional Raman scattering non-destructively measures the chemical composition of self-assembled monolayers, thin polymer films, and dielectric waveguides at a metal interface. In addition, this technique simultaneously provides the optical and physical properties of these samples. The enhanced Raman signals are attributed to the collection of the entire surface-plasmon-polariton cone generated from the excitation of surface plasmons from smooth planar metallic films. The surface-plasmon-polariton cone produces a directional scatter of photons through a Weierstrass prism, and this phenomenon results in an increase of the electric field at the metal/sample interface.

The instrument development of the directional Raman spectrometer has the combined benefits of surface plasmon resonance and Raman spectroscopy. The significant advantages of utilizing directional Raman spectroscopy are, 1) the interface selectivity, and 2) the excellent depth profiling resolution combined with 3) an enhancement of the Raman signal. Also, the directional Raman spectrometer is capable of collecting three angle-dependent parameters: the SPP cone intensity, cone diameter, and the Raman scattering signal on a single instrument. The three angle-dependent parameters will be useful for analyzing smooth films such as those used in energy capture and conversion devices, where the film morphology and composition are essential components to their functionalities.

The system utilizes smooth planar metallic films that increase the reproducibility of the measurement and can provide simple modeling of the experimental data. The Kretschmann and reverse-Kretschmann configurations are operated on the directional Raman spectrometer with ease of switching between both configurations. This ensures the fast acquisition of all the waveguide modes in a dielectric waveguide film by operating in the reverse-Kretschmann mode. At the same time, the Raman signal is collected in the Kretschmann configuration.

Directional Raman spectroscopy has similar sensitives that parallel with those reported in the literature for surface plasmon resonance and plasmon waveguide resonance measurements but require minimal data collection or no angle scanning. The enhanced Raman signal from the collection of the full surface-plasmon-polariton cone excites the vibrational modes of metal-sulfur bonds from 1,2-ethanedithiol and benzenethiol monolayers chemisorbed on metallic surfaces. The experimental measurement of these metal-sulfur bonds can address critical information about their formation. Specifically, the physical and chemical properties of the hydrocarbon thiols and the immobilization of biomolecules onto the substrate can serve as a sensor.

Lastly, the total internal reflection Raman spectroscopy techniques discussed in this dissertation will continue to find an increased use in our world. These techniques can be applied to analyze energy storage and harvesting devices, as well as used in multilayered films for the automotive, medical, and meat-packing industries. Directional Raman spectroscopy can be useful in characterizing microelectronics and can be applicable in nanotechnology devices, in which self-assembled monolayers are adsorbed onto smooth planar metallic surfaces. The future of directional Raman spectroscopy will be aimed at measuring thinner films, lower concentrations of immobilized species, and obtaining superb depth profiling measurements and resolution of the directional Raman signal in a variety of systems.